

BRNO UNIVERSITY OF TECHNOLOGY

VYSOKÉ UČENÍ TECHNICKÉ V BRNĚ

FACULTY OF MECHANICAL ENGINEERING

FAKULTA STROJNÍHO INŽENÝRSTVÍ

INSTITUTE OF PHYSICAL ENGINEERING

ÚSTAV FYZIKÁLNÍHO INŽENÝRSTVÍ

PREPARATION AND CHARACTERIZATION OF GRAPHENE BASED HYBRID MATERIALS

PŘÍPRAVA A CHARAKTERIZACE HYBRIDNÍCH MATERIÁLŮ NA GRAFENOVÉ BÁZI

MASTER'S THESIS

DIPLOMOVÁ PRÁCE

AUTHOR

AUTOR PRÁCE

Bc. Jakub Hrubý

SUPERVISOR

VEDOUCÍ PRÁCE

Ing. Petr Neugebauer, Ph.D.

BRNO 2017

Zadání diplomové práce

Ústav: Ústav fyzikálního inženýrství
Student: **Bc. Jakub Hrubý**
Studijní program: Aplikované vědy v inženýrství
Studijní obor: Fyzikální inženýrství a nanotechnologie
Vedoucí práce: **Ing. Petr Neugebauer, Ph.D.**
Akademický rok: 2016/17

Ředitel ústavu Vám v souladu se zákonem č.111/1998 o vysokých školách a se Studijním a zkušebním řádem VUT v Brně určuje následující téma diplomové práce:

Příprava a charakterizace hybridních materiálů na grafenové bázi

Stručná charakteristika problematiky úkolu:

Hlavní myšlenkou tohoto projektu je prozkoumat možnosti smíchání grafenu s komplexy kovů, což by mohlo přinést nové přístupy v materiálech založených na grafenu a molekulárním magnetizmu. Vzorky jsou připraveny sonikací grafitu v kapalně fázi, která vede k exfoliaci grafenu. Komplexy kovů jsou smíchány dohromady s grafenem, který má tendenci ke zpětné agregaci na grafit v průběhu času vlivem van der Waalsových sil. Tento mechanismus by mohl být využit k interkalaci komplexů kovů (molekulárních magnetů) mezi vrstvy grafenu. Magnetické vlastnosti nových hybridních materiálů budou charakterizovány vysokofrekvenční paramagnetickou rezonancí elektronů (angl. HFEPN) a supravodivým kvantovým interferenčním zařízením (angl. SQUID), elektronické vlastnosti pak měřeními transportu. Získané vlastnosti budou porovnány s výchozími nesmíšenými materiály.

Cíle diplomové práce:

Připravit grafen z grafitu exfoliací v kapalně fázi
Smíchat různé komplexy kovů s exfoliovaným grafenem
Charakterizovat připravené vzorky vhodnými metodami (HFEPN, SQUID, SEM, XPS, atd.)

Seznam doporučené literatury:

Weil, J. and Bolton, J., Electron Paramagnetic Resonance: Elementary Theory and Practical Applications, Second Edi. New Jersey: John Wiley & Sons, 2007.
Rieger, P. H., Electron Spin Resonance, First Edi. Cambridge: The Royal Society of Chemistry, 2007.
Lotya, M., King, P. J., Khan, U., De, S. and Coleman, J. N., High-Concentration, Surfactant-Stabilized Graphene Dispersions, ACS Nano, vol. 4, no. 6, pp. 3155–3162, Jun. 2010.

Paton, K. R. et al. Scalable production of large quantities of defect-free few-layer graphene by shear exfoliation in liquids, Nat. Mater., vol. 13, no. 6, pp. 624–630, 2014.

Termín odevzdání diplomové práce je stanoven časovým plánem akademického roku 2016/17

V Brně, dne

L. S.

prof. RNDr. Tomáš Šíkola, CSc.
ředitel ústavu

doc. Ing. Jaroslav Katolický, Ph.D.
děkan fakulty

Abstract

Graphene with metal complexes could provide novel approaches in graphene-based hybrid materials and molecular magnetism. Both topics are highly innovative as such, however, there is a little research into possibilities of mixing them. Samples were prepared by a liquid-phase sonication of graphite which resulted in the exfoliation of graphene. Subsequently, various metal complexes were deposited onto a graphene-covered substrate by modified Langmuir–Schaefer method. An essential step was to determine the material's properties. Consequently, properties of new hybrid materials were characterised by high frequency electron paramagnetic resonance (HFEP), scanning electron microscopy (SEM), Raman spectroscopy and four-point probe resistance measurements. Herein, the results confirmed our presumption that it is possible to mix exfoliated graphene with potential molecular magnets in order to gain novel magnetic and electronic properties which could be possibly utilised in the next generation of detectors and electronics.

Abstrakt

Grafen v kombinaci s komplexy kovů by mohl poskytnout nové přístupy v hybridních materiálech založených na grafenové bázi a v oblasti molekulárního magnetismu. Obě témata jsou velmi diskutovaná jako taková, nicméně, výzkumu vedoucího k možnosti jejich míchání není mnoho. Vzorky byly připraveny sonikací grafitu v kapalně fázi, což vedlo k exfoliaci grafenu. Následně byly nadeponovány pomocí modifikované Lagmuirovy–Schaeferovy depoziční metody různé komplexy kovů na substrát pokrytý grafenem. Klíčovým krokem bylo určení vlastností takto připraveného materiálu. Proto byly následně vlastnosti takového hybridního materiálu charakterizovány pomocí vysokofrekvenční elektronové paramagnetické rezonance (angl. HFEP), rastrovacího elektronového mikroskopu, (angl. SEM), Ramanovou spektroskopií a čtyř bodovou metodou měření odporu. V této práci jsme potvrdili naši presumpci, že je možné vytvořit hybridní materiál smícháním exfoliovaného grafenu s molekulárními magnety pro získání nových magnetických a elektronických vlastností, které by mohly být využity v další generaci detektorů a elektroniky.

Keywords

graphene, liquid-phase exfoliation, molecular magnetism, spectroscopy, magnetochemistry, metal complexes

Klíčová slova

grafen, exfoliace v kapalně fázi, molekulární magnetismus, spektroskopie, magnetochemie, komplexy kovů

HRUBÝ, Jakub. *Preparation and Characterization of Graphene Based Hybrid Materials*. Brno, 2017. 91 p. Master's thesis. Brno University of Technology. Faculty of Mechanical Engineering. Supervised by Ing. Petr NEUGEBAUER, Ph.D.

I hereby confirm that my Master Thesis: *Preparation and Characterization of Graphene Based Hybrid Materials* was written by myself and myself only under supervision of Ing. Petr Neugebauer, Ph.D. with the use of sources quoted in References.

Bc. Jakub Hrubý

I would like to thank everyone who directly or indirectly contributed to this project. Especially, I would like to thank my supervisor Dr. Petr Neugebauer as well as prof. Tomáš Šikola, the director of Institute of Physical Engineering in Brno, and the group leader, prof. Joris van Slageren, at the University of Stuttgart, for giving me the the opportunity to work on this project. Big thanks also goes to: Dr. Ivan Nemeč, Dr. Dmytro Kostyuk, Dr. Mauro Perfetti, Dr. Tomáš Šamořil, Bc. Martin Schneider, Ing. Michal Kern, Dipl.-Chem. Dominik Bloos, M.Sc. Philipp Hallmen, M.Sc. Samuel Lenz, M.Sc. Heiko Bamberger, and all faculty personnel at both University of Stuttgart and Brno University of Technology.

This research was carried out under the project CEITEC 2020 (LQ1601) with financial support from the Ministry of Education, Youth and Sports of the Czech Republic under the National Sustainability Programme II.

Special thanks goes to my family for material and spiritual support. The last and the biggest thanks belongs to my beloved soul mate who stood beside me, I love you.

Bc. Jakub Hrubý

Contents

Preface	1
1. Introduction	3
2. Theory	5
2.1. Graphene Fundamentals	5
2.1.1. Electronic Structure	5
2.1.2. Real and Reciprocal Space	6
2.1.3. Band Structure	8
2.1.4. Mobility and Density of Carriers	10
2.2. Single-Molecule Magnets (SMMs)	12
2.2.1. Molecular Magnetism	12
2.2.2. Magnetic Interactions in SMMs	15
2.3. Langmuir–Blodgett Films	18
2.3.1. Thermodynamic Equilibrium	18
2.3.2. Gas–Liquid Interface	19
2.3.3. Monolayer Formation	20
2.3.4. Surface Pressure Measurement	22
2.4. Electron Paramagnetic Resonance (EPR)	23
2.4.1. Basic Principles and Historical Background	23
2.4.2. Scope of EPR	25
2.4.3. Angular Momentum and Relation to Magnetic Moment	27
2.4.4. EPR Spectrometer	29
2.5. Raman Spectroscopy	30
2.6. Scanning Electron Microscopy (SEM)	32
3. Experiment	35
3.1. Preparation of Graphene-Based Hybrid Materials	36
3.1.1. Few-Layer Graphene (FLG) – Deposition	36
3.1.2. Molecular Deposition	38
3.2. Characterisation of Graphene-Based Hybrid Materials	42
3.3. Resistance Measurements	42
3.3.1. High Frequency EPR Spectrometer	43
3.4. Few-Layer Graphene (FLG)	45
3.4.1. Raman Spectroscopy	45
3.4.2. High Frequency EPR	46
3.4.3. Scanning Electron Microscopy	47
3.5. Cu(dbm) ₂	48
3.5.1. Synthesis and Structure	48

3.5.2.	Isotherms	49
3.5.3.	Raman Spectroscopy	51
3.5.4.	High Frequency EPR	52
3.5.5.	Scanning Electron Microscopy	54
3.6.	Ni(salen)	55
3.6.1.	Synthesis and Structure	55
3.6.2.	Isotherms	55
3.6.3.	Raman Spectroscopy	57
3.6.4.	High Frequency EPR	58
3.6.5.	Scanning Electron Microscopy	59
3.7.	DM15N	60
3.7.1.	Synthesis and Structure	60
3.7.2.	Isotherms	60
3.7.3.	Raman Spectroscopy	62
3.7.4.	High Frequency EPR	63
3.7.5.	Scanning Electron Microscopy	66
3.8.	DM18N	67
3.8.1.	Synthesis and Structure	67
3.8.2.	Isotherms	67
3.8.3.	Raman Spectroscopy	69
3.8.4.	High Frequency EPR	70
3.8.5.	Scanning Electron Microscopy	72
3.9.	ErPc ₂	73
3.9.1.	Synthesis and Structure	73
3.9.2.	Isotherms	73
3.9.3.	Raman Spectroscopy	75
3.9.4.	High Frequency EPR	76
3.9.5.	Scanning Electron Microscopy	78
4.	Conclusions	81
	References	85
	List of Abbreviations	91

Preface

This master thesis aims to bring together graphene and molecular magnets; two topics that have recently risen a significant interest in both scientific and industrial community. This can be ascribed to extraordinary potential how these fields of interest could change and improve everyday life, not only of human kind. Several steps are crucial in order to successfully connect these topics and to bring such an idea to life. Firstly, it is essential to investigate both materials as such. The best scenario would be to gain a full understanding of behaviour at atomic dimensions by the means of mathematics, physics, and chemistry. This, however, is often limited by the experimental equipment or human inability to gain, process, and use knowledge. The best what can we do is to try and never give up in pursuit of understanding the laws of nature.

The idea was formed in summer 2016 during my Erasmus+ experience in AG van Slageren at University of Stuttgart, Germany. Along with my supervisor Dr. Neugebauer, we decided to depart on a journey towards the mixing of graphene with metal complexes. Former experiments took place at the University of Stuttgart in summer 2016. After my return to Brno, several experiments were conducted in sonochemistry laboratories of CEITEC - MUNI in Brno in the group of Prof. Pinkas and with the help of Mgr. Kuchařová, whom I would like to thank for contributions on the journey towards graphene-based hybrid materials. Our next 'stop' was at Slovak Academy of Sciences in Bratislava, where the deposition of thin films with the help of Dr. Kostyuk and Dr. Šiffalovič took place. Several detours led also to Palacký University Olomouc and Dr. Ivan Nemeč, who made a major contribution to the work concerning the metal complexes involved. The second to last 'stop' was in the place of the origin in Stuttgart, where the experiments related to high frequency electron paramagnetic resonance (HFEPN), Raman spectroscopy (with the help of M.Sc. Knecht), and scanning electron microscopy (with the help of M.Sc. Qawasmi), took place. The final destination on our journey was Brno, where the second scanning electronic microscopy (with the help of Dr. Šamořil), and Raman spectroscopy (with the help of Dr. Hemzal), was carried out. One journey represented by this thesis, out of an ocean of never-ending journeys, towards the investigation of graphene-based materials, is over.

The content of this thesis is following: the first chapter (1. Introduction) is supposed to provide a brief outlook on the topic and current state-of-the-art. The second chapter (2. Theory) deals with the main focus of this work, which is to connect graphene with metal complexes. The emphasis is also given on the theoretical description of characterisation methods used in the third section (3. Experiment). The last section (4. Conclusions) summarises the results obtained during an experiment with outlining the implications that arose from this work and possibilities for further improvement and treatment of this topic.

PREFACE

1. Introduction

This chapter gives reader a brief idea about the topic and overview of current state-of-the-art at the research area related novel materials. Detailed theoretical background is provided throughout the (2. Theory) section of this thesis.

Graphene, a single layer of bonded carbon atoms, has recently generated a significant interest due to its unique physical properties [1]. Figure (1.1) illustrates graphene as one of many carbon allotropes in the form of two-dimensional hexagonal lattice. It exhibits the highest electrical conductivity from all known materials up to date [2], mechanical strength is 200 times greater than steel at a one sixth of a weight [3], and a thermal conductivity is even superior to that of diamond [4]. Graphene was originally isolated through micro-mechanical cleavage of graphite, which is also known as the 'Scotch tape' method. This discovery was honoured with the Nobel Prize in Physics in 2010 [5]. Nowadays, there are several methods how to prepare graphene, namely epitaxial growth from silicon carbide, chemical vapour deposition (CVD), and liquid-phase exfoliation. The last method is possibly the best option for scalable production of graphene based hybrid materials, thin conductive films, and thermal pastes [6], [7]. Graphene-based composites can also be utilised in body motion sensors as shown by Boland et al. [8]. He presented a very sensitive strain gauge based on graphene-rubber composite which was used for monitoring joint and muscle motion as well as breathing and pulse.

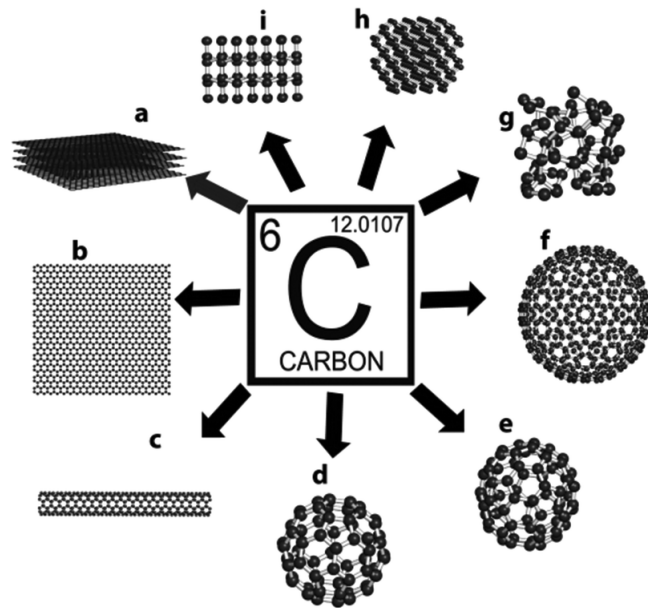


Figure 1.1: Illustration of carbon allotropes: (a) graphite, (b) graphene, (c) carbon nanotube, (d) fullerene C₆₀, (e) fullerene C₇₀, (f) fullerene C₅₄₀, (g) amorphous carbon, (h) lonsdaleite, and (i) diamond. Adapted from [9].

1. INTRODUCTION

Since 2004, the first description of atomically thin carbon films (graphene) by Novoselov et al. [5], numerous works have been published on 'graphene' (exactly: 112 919 according to Web of Science - entry on 22. 05. 2017). They have ranged from preparation methods mentioned by Rao et al. [10], intrinsic properties stated by Geim [11] to novel applications shown by Boland et al. [8]. Exfoliation of graphene is the reverse process of stacking; owing to the weak bonding and large lattice spacing in the perpendicular direction compared to the small lattice spacing and stronger bonding in the hexagonal lattice plane. The liquid-phase exfoliation appears to be feasible as graphene can be imagined as a stack of graphite sheets resulting from an overlap of partially occupied p_z or π orbital perpendicular to the plane of the sheet (involving van der Waals forces). In order to obtain exfoliated graphene, there is a need of external stimuli such as ultrasonic power discussed by Vadukumpully et al. [12], micromechanical cleavage mentioned by Geim and Novoselov [5], or by shear exfoliation in liquids demonstrated by Paton et al. [7].

In addition to graphene, quantum bits (qubits), core computational units based on molecular magnets, present one way in pursuing a quantum computer, a device which could substantially change all fields of human activity. Figure (1.2a) illustrates quantum mechanics principle of superposition in contrast to classical zeroes and ones, that are used in current computational technology. A quantum computer could outperform any classical one in factoring numbers and searching a database [13]. Molecular magnets, as candidates for a quantum bit, were investigated by Bader et al. [14].

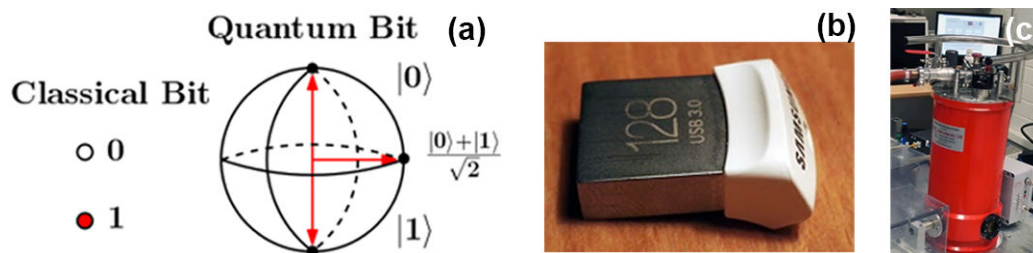


Figure 1.2: Potential applications of graphene-based hybrid materials: (a) quantum computing, (b) data storage, and (c) detection devices.

Metal complexes, however, are not only restrained to be used for quantum bits. Figure (1.2b) demonstrates their potential application in data storage. Some of them also exhibit interesting properties such as spin crossover behaviour, where transition from high to low or low to high spin state occurs [15],[16]. Another field of interest is improvement of broadband detectors as demonstrated by bolometer in Figure (1.2c), which is a very sensitive detection device of electromagnetic radiation. Utilisation of graphene for high-performance terahertz bolometers was proposed by El. Fatimy et al. [17].

Nowadays, graphene as such can be reasonably well prepared and characterised. However, utilising graphene properties with other materials is still in its infancy. Recently, there has been a growing interest in graphene-based materials; Hong et al. [18] chemically engineered graphene-based 2D organic molecular magnet by a nitrophenyl functionalisation of graphene. The ability to control magnetic properties of graphene-based hybrid materials is crucial for further development of carbon-based devices as shown by Le Ferrand et al. [19]. There are also several review articles that thoroughly describe possibilities of so-called supra-molecular approaches to graphene, such as this one written by Ciesielski et al. [20]. This work aims to bring together graphene with metal complexes, potential single-molecule magnets or quantum bits, and present preparation of graphene-based samples with subsequent characterisation of their properties.

2. Theory

This chapter aims to provide necessary theoretical background for the experimental part of this thesis, and follows the thesis structure by covering main topics involved. Considering the diversity of covered scientific interest in the thesis, I have decided to pinpoint fundamentals of graphene, single-molecule magnets (SMMs), and experimental methods used: Langmuir–Blodgett films, electron paramagnetic resonance (EPR), Raman spectroscopy, and scanning electron microscopy (SEM).

2.1. Graphene Fundamentals

In order to create and control graphene-based hybrid materials, it is crucial to understand theoretical fundamentals of graphene. Brief history and information related to current use of this carbon allotrope were already mentioned in previous (1. Introduction) chapter. This section aims to provide deeper insight into physical and chemical properties of graphene. The structure follows book: Graphene: Fundamentals and Emergent Applications [21].

2.1.1. Electronic Structure

Carbon is an interesting element due to diversity of structural existing forms in which it occurs. For instance, graphite and diamond are the best-known allotropes of carbon. This structural variety arises from different electron configuration of carbon, which enables forming of different types of valence bonds to various elements, as well as to other carbon atoms, through atomic orbital hybridisation. Carbon ${}^6\text{C}$ has the atomic number 6 and therefore, electrons occupy the $1s^2$, $2s^2$, $2p_x^1$, and $2p_y^1$ atomic orbitals in ground state. Figure (2.1) shows sp^3 and sp^2 hybridisation of carbon atom from his ground state. Carbon is tetravalent element, i.e., only the four exterior electrons participate in the formation of covalent chemical bond. When forming bonds with other atoms, carbon promotes one of the 2s electrons into the unoccupied $2p_z$ orbital, this results in the formation of hybrid orbitals.

In diamond, the first possible hybridisation, sp^3 , occurs. The 2s-energy level hybridises with the three 2p levels in order to form four energetically equivalent sp^3 -orbitals, each occupied with one electron. The sp^3 -orbitals are oriented with largest possible distance from each other in this orientation, thus forming an imaginary tetrahedron. The sp^3 -orbitals of one carbon atom overlap with the sp^3 -orbitals of other carbon atoms, which results in formation of the 3D diamond structure¹.

In graphite, the second possible hybridisation, sp^2 , occurs. Only two out of three 2p-orbitals take part in the hybridisation resulting in three sp^2 -orbitals that are oriented

¹The high hardness of diamond results from the strong binding energy of the C–C bonds.

2. THEORY

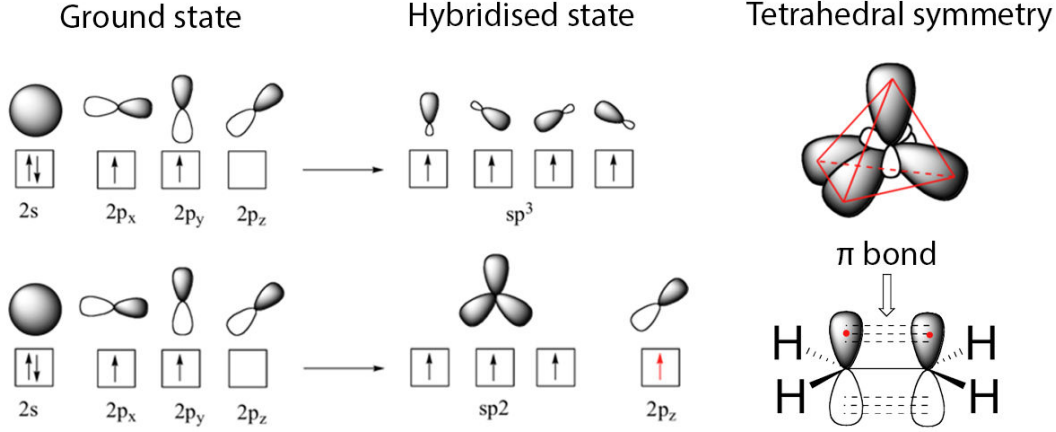


Figure 2.1: Illustration of two possible hybridisations of carbon atom electron orbitals. Upper row demonstrates sp^3 hybridisation resulting in tetrahedron (e.g. methane or diamond). Lower row represents sp^2 hybridisation, which leads to formation of π bond (e.g. ethylene, graphite or graphene). Adapted from [22].

perpendicular to the remaining 2p-orbital and lying symmetrically in the xy plane at 120° angles. Therefore, sp^2 -carbon atoms form covalent in-plane bonds causing the planar hexagonal "honeycomb" structure of graphite. The in-plane σ -bonds within the graphene layers (615 kJ/mol) are even stronger than those of the C–C bonds in sp^3 -hybridised diamond (345 kJ/mol). The interplane π -bonds formed by the remaining 2p-orbitals have, however, significantly lower binding energy, which leads to an easy shearing of graphite along the layer plane.

2.1.2. Real and Reciprocal Space

A graphene layer can be imagined as a single-layer of graphite with the lattice constant $a = \sqrt{3}a_0$ where $a_0 = 1.42 \text{ \AA}$ is the nearest neighbour interatomic distance. The interplane distance between two adjacent graphene layers in AB stacked graphite is 3.35 \AA . Strictly taken, 'graphene' refers to a quasi-two-dimensional isolated monolayer of carbon atoms that are arranged in a hexagonal lattice. It is important to investigate into the structure of graphene thoroughly, as its electronic properties are significantly dependant on the number of graphene layers. Only single-layer graphene (SLG) and bilayer graphene (BLG) are considered to be zero-gap semiconductors with only a single type of electrons and holes, respectively. In the case of the few-layer graphene (FLG), usually 3 to 10 layers, the conduction and valence band start to overlap and several charge carriers appear. Thicker structures can be considered as thin films of graphite.

The hexagonal graphene lattice is illustrated in Figure (2.2) on the left side. The unit cell of graphene is a rhombus (grey) with a basis of two non-equivalent carbon atoms (A and B). The black and white circles are sites of the corresponding A and B triangular construction. In Cartesian coordinates, the real space basis vectors of unit cell \vec{a}_1 and \vec{a}_2 can be written as

$$\vec{a}_1 = \begin{pmatrix} \sqrt{3}a/2 \\ a/2 \end{pmatrix} \quad \text{and} \quad \vec{a}_2 = \begin{pmatrix} \sqrt{3}a/2 \\ -a/2 \end{pmatrix} \quad (2.1)$$

with the lattice constant $a = \sqrt{3}a_0$.

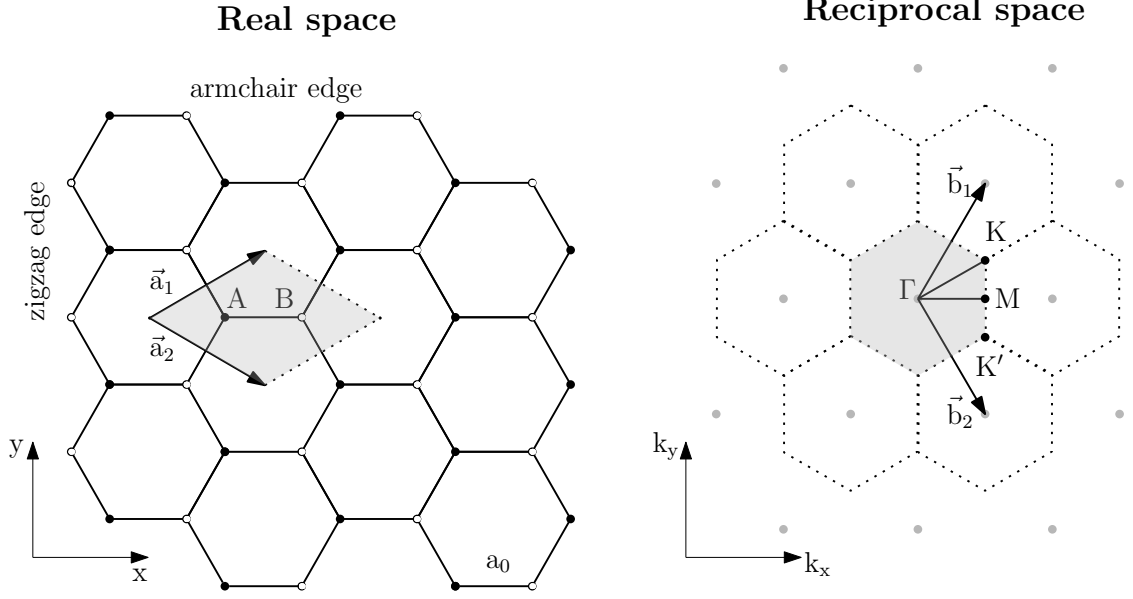


Figure 2.2: Crystal structure of graphene: Left side shows 2D hexagonal lattice of graphene in real space with basis vectors \vec{a}_1 and \vec{a}_2 . The unit cell is highlighted by grey colour. It contains two non-equivalent carbon atoms A and B, each of which span a triangular construction as indicated with black and white atoms, respectively. Right side shows reciprocal lattice (dashed) with reciprocal lattice vectors \vec{b}_1 and \vec{b}_2 . The first Brillouin zone is highlighted by grey colour and the high symmetry points Γ , M, K, and K' are indicated.

Corresponding reciprocal lattice is shown in Figure (2.2) on the right side together with the first Brillouin zone (grey hexagon). The reciprocal basis vectors \vec{b}_1 and \vec{b}_2 can be expressed as follows

$$\vec{b}_1 = \begin{pmatrix} 2\pi/\sqrt{3}a \\ 2\pi/a \end{pmatrix} \quad \text{and} \quad \vec{b}_2 = \begin{pmatrix} 2\pi/\sqrt{3}a \\ -2\pi/a \end{pmatrix} \quad (2.2)$$

with reciprocal lattice constant $4\pi/\sqrt{3}a$ and indicated points of high symmetry (Γ , M, K, K'). The reciprocal lattice is useful geometrical construction in describing diffraction data. It is an array of points where each point corresponds to a specific set of lattice planes of the crystal in real space. Furthermore, it is generally used to depict a material's electronic band structure by plotting the bands along specific reciprocal directions within the Brillouin zone (e.g. from Γ to M or K in graphene). Especially the two points K and K' (also known as Dirac points) play a crucial role. Their coordinates in reciprocal space can be expressed as

$$K = \begin{pmatrix} 2\pi/\sqrt{3}a \\ 2\pi/3a \end{pmatrix} \quad \text{and} \quad K' = \begin{pmatrix} 2\pi/\sqrt{3}a \\ -2\pi/3a \end{pmatrix} \quad (2.3)$$

Graphene is a zero-gap semiconductor since the conduction and valence bands are in contact at the Dirac points and exhibit a linear dispersion. The electronic density of states is zero at the Dirac points. This topology of the bands gives rise to unique and rather exotic electronic transport properties. Finally, this makes graphene a promising candidate for broad range of applications in new generation of molecular electronics, graphene-based devices [21].

2. THEORY

2.1.3. Band Structure

Graphene has risen large scientific interest mainly due to its unique electronic properties. The band structure of mono-layer graphene exhibits three main features; the vanishing carrier density at the Dirac points, the existence of pseudo-spin and the relativistic nature of carriers.

The band structure of graphene emerges from its atomic structure. Every carbon atom in the graphene lattice is connected to three neighbouring atoms by strong in-plane covalent bonds. These σ bonds are from electrons in the 2s, 2p_x, and 2p_y valence orbitals. The remaining fourth valence electron occupies 2p_z orbital, which is perpendicular to the graphene sheet plate, and thus does not interact with the in-plane σ electrons. The 2p_z orbitals from neighbouring atoms overlap resulting in delocalised π (i.e. occupied or valence) and π^* (i.e. unoccupied or conduction) bands. Majority of electronic properties of graphene can be understood by these π bands.

The unit cell of the hexagonal graphene lattice consists of two atoms separated by $a_{C-C} = 1.42 \text{ \AA}$. Figure (2.3) illustrates the division of unit cell of the hexagonal graphene lattice into two interspersed triangles, usually denoted A and B. The original description of this triangular concept along with first calculation of the band structure of mono-layer graphene was done by Wallace in 1947 [23]. The band structure can be sufficiently described using nearest neighbour tight-binding approach considering a single π electron per atom. Final dispersion relation can be written

$$E^{\pm}(k_x, k_y) = \pm\gamma_0 \sqrt{1 + 4 \cos \frac{\sqrt{3}k_x a}{2} \cos \frac{k_y a}{2} + 4 \cos^2 \frac{k_y a}{2}} \quad (2.4)$$

with $a = \sqrt{3}a_{C-C}$, and γ_0 the nearest neighbour overlap integral which takes a value between 2.5 and 3 eV.

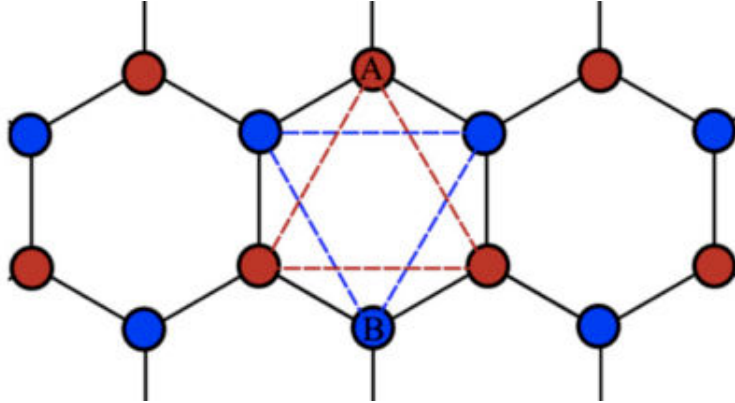


Figure 2.3: Triangular division of hexagonal graphene structure. Each atom of the A triangle is surrounded by three B triangle atoms and vice-versa. Adapted from [21]

The band structure of graphene calculated by Equation (2.4) is shown in Figure (2.4). The valence and conduction bands meet at points of high symmetry K and K'. In intrinsic (un-doped) graphene each carbon atom provides one electron completely filling the valence band and leaving the conduction band empty. Fermi level E_F , as such, is situated at the energy where the conduction and valence bands meet. These points are known as the Dirac or charge neutrality points. The dispersion relation can be limited to just two of the Dirac points ($K = [2\sqrt{3}\pi/3a, 2\pi/3a]$ and $K' = [2\sqrt{3}\pi/3a, -2\pi/3a]$). Other are

equivalent through translation by a reciprocal lattice vector. These two Dirac points in reciprocal space can be directly related to the two real space graphene triangles, where K is caused by electrons on triangle A and K' by electrons on triangle B.

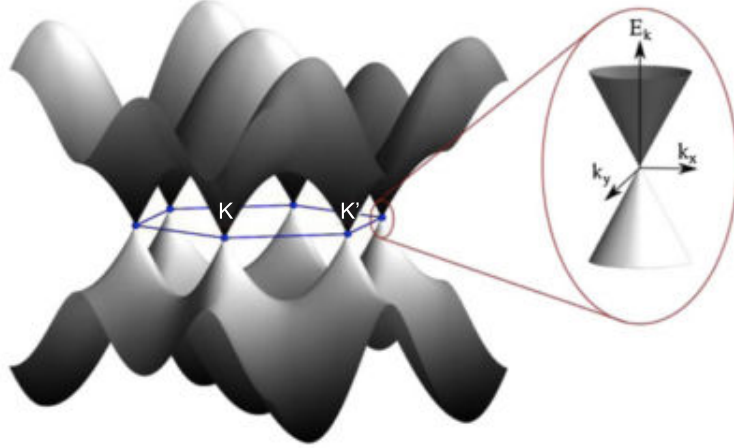


Figure 2.4: Band structure of graphene illustrating the conduction and valence bands meeting at the Dirac points (marked with blue dots). Inset is a zoom of one of the Dirac points showing the linear dispersion relation at small values of \vec{k} . Adapted from [21]

Equation (2.4) can be expanded close to the Dirac point (K or K') resulting in dispersion relation showing the linear relation between energy, $E(\vec{k})$ and momentum, \vec{k} :

$$E^\pm(\vec{k}) = \hbar v_F |\vec{k} - K| \quad (2.5)$$

where $\vec{k} = (k_x, k_y)$ and $v_F = (\sqrt{3}\gamma_0 a / 2\hbar) \approx 1 \times 10^6 \text{ ms}^{-1}$. The region of the dispersion relation close to K(K') is plotted in the inset to Figure (2.4), showing the linear nature of the Dirac cones. To sum up, by considering the nearest neighbour tight-binding description, the band structure of graphene can be calculated. This implies three important features which in general define the nature of electron transport through this material:

1. The occupied valence and empty conduction bands meet at Dirac point at which the density of states (DOS) is zero. Therefore, graphene is best described as a zero-gap semiconductor with vanishing DOS at the Dirac point but no energy gap between the valence and conduction bands.
2. Close to the Fermi energy the band structure can be described by two inequivalent Dirac cones situated at K and K'. A large momentum change is required for an electron to scatter from K to K'. Therefore, electron transport in graphene can be imagined as occurring in parallel through the K and K' Dirac cones (corresponding to the two graphene triangles A and B). Charge carriers in graphene have, in addition to orbital and spin quantum number, a valley or pseudo-spin quantum number with a degeneracy of 2. The term pseudo-spin is used due to analogy with real spin, they are however, completely independent of one and other.
3. Close to the Dirac point the graphene dispersion relation is linear in nature. This linear-dispersion relation is well described by the relativistic Dirac equation. In this description the charge carriers (electrons or holes) act as massless Dirac fermions travelling with a group velocity of $v_F \approx 1 \times 10^6 \text{ ms}^{-1}$.

2. THEORY

2.1.4. Mobility and Density of Carriers

Electronic properties of graphene can also be described by means of solid state physics, namely the Drude model of electrical conduction to elucidate the transport properties of electrons, mainly in metals, proposed in 1900 [24]. This model presumes that electrons can be approximated as free particles, bouncing off heavier, immobile positive ions. One important result of this model is a linear relationship between current density \vec{j} and electric field \vec{E}

$$\vec{j} = \sigma \vec{E} \quad (2.6)$$

where σ is the electrical conductivity (the inverse of resistivity ϱ). The electrical conductivity σ can be then, for the case of Fermi gas (approximation for metals), defined as

$$\sigma = \frac{ne^2\tau}{m} \quad (2.7)$$

where charge transported is proportional to the charge density ne , the factor e/m is present, because the acceleration in a given electric field is proportional to e and inversely proportional to the mass m . The τ describes the free time during which the field acts on the carrier [25].

It is convenient to introduce terms that are representing material properties. This is expressed by the charge carrier mobility μ , which is the ratio of the carrier drift velocity v_d to the applied electrical field \vec{E} . The current density defined by Equation (2.6) can be subsequently written as

$$\vec{j} = ne\vec{v}_d = ne\mu\vec{E}. \quad (2.8)$$

Combination of Equation (2.7) and Equation (2.8) shows that electrical conductivity σ is related to the charge carrier mobility μ as follows

$$\sigma = ne\mu. \quad (2.9)$$

In the case of graphene, n and μ were determined either from field effect or Hall effect measurements.

Using field effect measurements, the density of carriers n in a graphene sample can be estimated from the surface charge density induced by application of a gate voltage

$$n = \varepsilon_0\varepsilon_r V_g / te \quad (2.10)$$

where ε_0 is permittivity of vacuum, ε_r the relative permittivity of the dielectric (e.g. SiO₂), t the dielectric thickness and e is elementary charge. As $n = 0$ at Dirac point, any doping of the sample is compensated for by replacing V_g in Equation (2.10) by $(V_g - V_{gD})$ with V_{gD} the gate voltage at the Dirac point.

The field effect mobility μ_{FE} can be extracted from the gate voltage dependence of conductivity

$$\mu_{FE} = \frac{d\sigma}{dV_g} \frac{1}{C_g} \quad (2.11)$$

where σ is the conductivity of the sample and C_g the gate capacitance which can be calculated as $C_g = ne / (V_g - V_{gD})$.

Alternatively, the carrier density and mobility can be determined by performing a Hall effect measurement which is shown in Figure (2.5) below.

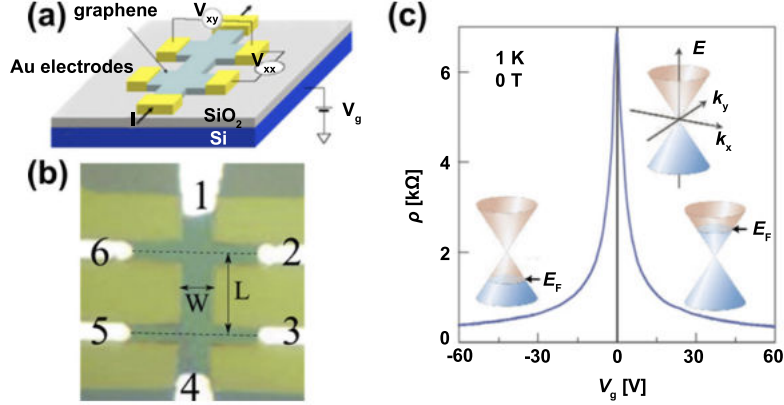


Figure 2.5: (a) Schematic of a standard device geometry for such measurements on graphene samples is the Hall bar. Graphene is transferred to a heavily doped Si substrate capped with an insulating SiO₂ layer of several hundreds of nanometres, (b) optical microscope image illustrates an etched graphene sample into a Hall bar geometry by lithographic means (i.e. patterned resist mask followed by plasma etching). A four-point probe measurement can be then performed by driving a current between electrodes 1 and 4, I_{14} , and measuring the voltage drop between electrodes 2 and 3, V_{23} (or 5 and 6, V_{56}), (c) modulation of a graphene sample by the application of a gate voltage. By electrically contacting the heavily doped Si, an electric field is applied across the sample by application of gate voltage V_g . This can be used to tune the Fermi level E_F (thus also carrier density) of the graphene. As E_F approaches Dirac point ($V_g = 0$), resistivity reaches its maximum. This measurement allows for the study of electron transport when E_F is above Dirac point (conduction band) and hole transport for E_F below the Dirac point (valence band). Adapted from [21]

The resistivity of graphene sample in this case is defined as

$$\rho_{xx} = \left(\frac{W}{L}\right) \left(\frac{V_{23}}{I_{14}}\right) \quad (2.12)$$

and units are Ohms. W is the width and L the length of the graphene channel between the voltage probes. The transverse resistivity $\rho_{xy} = (W/L)(V_{26}/I_{14})$ of a sample is measured in presence of an out of plane magnetic field. The carrier density is then expressed as

$$n = B/e\rho_{xy} \quad (2.13)$$

with the Hall coefficient defined as

$$R_H = \frac{1}{ne}. \quad (2.14)$$

When the charge carrier density is known the Hall mobility can be written as

$$\mu_H = \frac{1}{ne\rho_{xx}} = \left(\frac{1}{ne}\right) \sigma_{xx}. \quad (2.15)$$

Hall mobilities even higher than $200\,000\text{ cm}^2\text{ V}^{-1}\text{ s}^{-1}$ have been reported for graphene devices with charge carrier densities for two-dimensional graphene as low as $5 \times 10^9\text{ cm}^{-2}$ [21]. To sum up, determination of material properties such as charge carrier density n and charge carrier mobility μ is crucial for development of novel graphene-based devices.

2.2. Single-Molecule Magnets (SMMs)

This chapter is written to provide an introduction to the approach of molecular magnetism by describing characteristic properties of SMMs and by outlining the magnetic interactions in molecular systems. The notation was taken from the book: *Molecular Nanomagnets* [26] and review: *Introduction to Molecular Magnetism* [27].

2.2.1. Molecular Magnetism

Molecular magnetism is rather new approach, fully developing from 1990s, describing magnetic behaviour at the scale of individual molecules and molecular clusters. It can be described as an interdisciplinary field, where chemists design and synthesise new materials with increasing complexity based on a feedback from physicists, that perform and develop experimental measurements in order to model the novel material properties associated with molecular materials. The rise of this approach is also closely related to the rising interest in nano-science and nanotechnology, that spans throughout natural sciences and industrial needs of miniaturisation processes connected to rapid development of computers. Along with the need for smaller components in devices, also the need for principles of quantum mechanics when describing these systems becomes relevant. Both theoretical and experimental parts are necessary for understanding and controlling matter at the nano-scale. Investigation of such systems was enabled by progress in the field of scanning probe microscopy such as atomic force microscopy, scanning tunnelling microscopy, scanning electron microscopy, etc.

Figure (2.6) illustrates the transition from the region of permanent magnets with magnetic domains containing huge number of spins to molecular clusters with hundreds of spins.

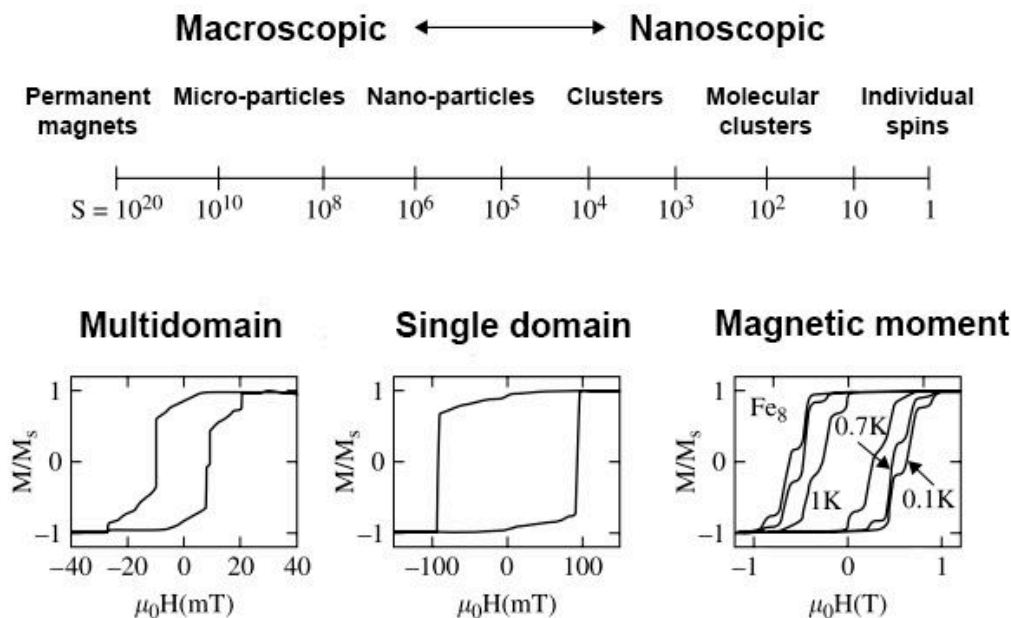


Figure 2.6: The transition from macroscopic to nanoscopic magnets. Different appearance of hysteresis loops for multidomain (left), single domain (middle), and individual magnetic moment (right). Adapted from [26].

2.2. SINGLE-MOLECULE MAGNETS (SMMS)

At the macro-scale, the particles constituting bulk magnet contain billions of individual spins, that are coupled and respond collectively to an external stimuli. The magnetic energy is minimised by forming domains, regions within all the individual magnetic moments are parallel (anti-parallel) to each other. The orientation of magnetic moment in magnetic domains is random in the absence of an external magnetic field, and thus the magnetisation of the sample is zero. When the sample is magnetised, all the individual moments will be parallel to each other and the magnetisation reaches its saturation value. If the field is decreased, the magnetisation will not be zero, like in the non-magnetised case, but it will exhibit so-called remanent magnetisation. Demagnetisation of the sample is possible by going to negative field, which is called coercive field. This is used in order to classify the bulk magnets. A small coercive field is typical for soft magnets (i.e. they do not tend to stay magnetised), and large in the case of hard magnets (i.e. permanent). The M/H plot, shown in Figure (2.6) on the left shows a hysteresis loop, which gives us information that the value of magnetisation of the sample is dependant on its history. This is the basis for the use of magnets for storing information.

When reducing the size of magnetic particles, magnetic anisotropy A of the sample comes into play

$$A = KV \tag{2.16}$$

where V is the volume of the particle and K is the anisotropy constant of the material.

Figure (2.7) shows the energy of the system as a function of the orientation of the magnetic moment. The anisotropy of the magnetisation is of an Ising type (i.e. the stable orientation of the magnetic moment of the particle is parallel to a given z direction).

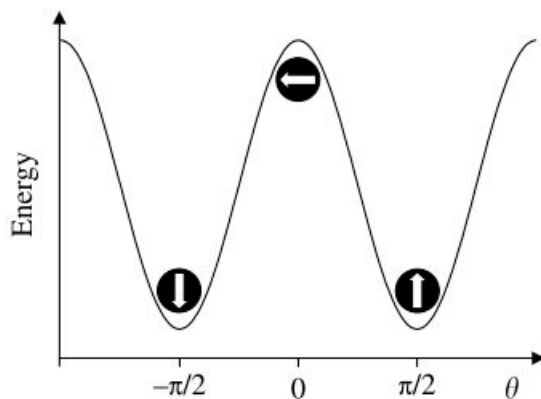


Figure 2.7: Energy of an Ising (easy axis) as a function of the angle of the magnetisation from the easy axis. Adapted from [26].

The bottom-left well represents energy minimum for magnetisation down, the bottom-right well energy minimum for magnetisation up, and the top between well represent energy maximum for the magnetisation at 90° from the easy axis. When reducing the size of the sample, the barrier for the reorientation of the magnetisation becomes comparable to the thermal energy. If the sample is prepared with up magnetisation (right well), some of the particles with enough energy can jump over the barrier and reverse their magnetisation. After a while, the equilibrium between up and down is established (i.e. half of them will be in the left and half in the right well), because the two minima have the same energy. The system will no longer be magnetised in zero magnetic field as a paramagnet. If, however, an external magnetic field is applied, one of the two wells will lower its energy and the

2. THEORY

other will increase it. The two wells will have different populations and the system behaves like a paramagnet, but since the response to the external perturbation of the system comes from all the individual magnetic centres, it will be large. These particles are called superparamagnets with interesting applications in magnetic drug delivery, magnetic separation of cells, and as a contrast agent for magnetic resonance imaging. The size of particles needed to observe this superparamagnetic behaviour ranges from 2 to 30 nm.

An important feature of the superparamagnet is whether the observation of either static or dynamic magnetic behaviour depends on the time-scale of the experiment used for such an investigation. For example, during AC magnetic susceptibility measurement with oscillating field at $\nu = 100$ Hz, static behaviour with a blocked magnetisation is observed if the characteristic time required for the particle to overcome the barrier is longer than $\tau_m = (2\pi\nu)^{-1}$. On the contrary, dynamic behaviour is observed for shorter τ_m . The characteristic time for the reorientation of the magnetisation can be calculated, assuming thermally activated process, as an exponential dependence on the energy barrier with so-called Arrhenius behaviour, as observed in many other thermally activated and chemical processes

$$\tau_N = \tau_0 \exp \frac{KV}{k_B T} \quad (2.17)$$

where KV is magnetic anisotropy, k_B Boltzmann constant and T absolute temperature.

Therefore, so-called blocking temperature can be defined, which corresponds to the temperature at which the relaxation time of the magnetisation $\tau_N = \tau_m$, the characteristic time of the experiment. The blocking temperature can be obtained from Equation (2.17) by expressing for temperature

$$T_B = \frac{KV}{k_B \ln(\frac{\tau_m}{\tau_0})}. \quad (2.18)$$

The single-molecule magnet (SMM) also exhibits a superparamagnetic behaviour below a certain blocking temperature. They can be imagined as zero-dimensional magnets. In other words, every molecule in SMMs can act as a nanomagnet. The preparation route is by means of synthetic chemistry. The structure of such SMM is following: the metallic centre, usually transition metal, lanthanide, or actinide, is surrounded by various organic ligands.

At this point, it is convenient to summarise optimal conditions to be met by a system in order to be considered as a single-molecule magnet, which is generally a class of metal-organic compounds with following features:

1. It is a molecule that exhibits slow relaxation of the magnetisation of purely molecular origin.
2. It can be magnetised in a magnetic field, and that will remain magnetised even after switching off the magnetic field.
3. It is inherent molecular property, and no interaction between molecules is necessary for this phenomenon to occur.
4. It can be dissolved in a solvent or put in a matrix (polymer), and it will still exhibit properties listed above.

2.2.2. Magnetic Interactions in SMMs

Magnetic interactions in a molecular system are principally the same as can be observed in continuous lattices. There are generally two interactions involved between two magnetic centres in a molecular system. One is purely magnetic and the other is electrostatic. The electrostatic interaction is responsible for the formation of the chemical bonds and the magnetic interaction for the formation of a weak chemical bond between two magnetic centres.

Herein, so-called spin Hamiltonian approach (SH) will be mentioned, as it proved to be a suitable interpretation and classification for experimentally measured spectra without the need for fundamental theories.

This SH approach expresses the Hamiltonian in powers of abstract spin-operators, absorbing the different (spatially dependent) interactions in effective parameters, and thus reducing the complexity of the problem. In the following section, focus will be given on systems with orbitally non-degenerate ground states with weak spin-orbit coupling (e.g. transition metal complexes) that are treated well by this approach.

A magnetic centre with n unpaired electrons has a ground state characterised by $S = n/2$. The $2S + 1$ spin levels associated to this multiplet are split by low-symmetry components of the corresponding Hamiltonian (crystal field hamiltonian), and by an applied magnetic field (Zeeman Hamiltonian). The term "crystal field" refers to a simplified treatment of the spin levels of transition metal compounds, where the effects of the atoms around the transition metal ions (the ligands or the donor atoms) are considered as the only source of ionic interactions.

The Zeeman Hamiltonian can be written as

$$\mathcal{H}_Z = -\mathbf{H} \cdot \mathbf{m} = \mu_B \mathbf{B} \cdot \mathbf{g} \cdot \mathbf{S} \quad (2.19)$$

where μ_B is Bohr magneton², \mathbf{B} is applied magnetic field, \mathbf{g} is a tensor linking the magnetic field and the spin vectors, and \mathbf{S} is a spin operator. The magnetic moment \mathbf{m} is given by

$$\mathbf{m} = -\mu_B \cdot \mathbf{g} \cdot \mathbf{S}. \quad (2.20)$$

As a time-even-operator, it is convenient to assume the crystal field splitting Hamiltonian to be a quadratic form of the spin operators defined now in the coordinate system corresponding to the diagonal form of the D-tensor.

$$\mathcal{H}_{CF} = \mathbf{S} \cdot \mathbf{D} \cdot \mathbf{S} \quad (2.21)$$

where \mathbf{D} is a real, symmetric tensor with three orthogonal eigenvectors. If the coordinate axes x , y , z are chosen to be parallel to these eigenvectors, \mathbf{D} is diagonal and Equation (2.21) can be expressed as

$$\mathcal{H}_{CF} = D_{xx}S_x^2 + D_{yy}S_y^2 + D_{zz}S_z^2 \quad (2.22)$$

where S_x , S_y , and S_z are spin operators.

The physical meaning is not changed by subtracting a constant from a Hamiltonian. Subtracting $(1/2)(D_{xx} + D_{yy})(S_x^2 + S_y^2 + S_z^2) = (1/2)(D_{xx} + D_{yy})S(S + 1)$, leads to

$$\mathcal{H}_{CF} = DS_z^2 + E(S_x^2 - S_y^2) \quad (2.23)$$

²Bohr magneton in SI units: $\mu_B = \frac{e\hbar}{2m_e} \doteq 9.274 \times 10^{-24} \text{ J} \cdot \text{T}^{-1}$.

2. THEORY

where

$$D = D_{zz} - \frac{1}{2}D_{xx} - \frac{1}{2}D_{yy} \quad \text{and} \quad E = \frac{1}{2}(D_{xx} - D_{yy}). \quad (2.24)$$

By subtracting the constant $DS(S+1)/3$ from Equation (2.23), the crystal field Hamiltonian is

$$\mathcal{H}_{\text{CF}} = D \left[S_z^2 - \frac{1}{3}S(S+1) \right] + E(S_x^2 - S_y^2). \quad (2.25)$$

The advantage of Equation (2.25) is that $\text{Tr } \mathcal{H}_{\text{CF}} = 0$, where Tr stands for the trace of the tensor. In addition, both Equations (2.23) and (2.25) are, when introducing eigenvectors $|m\rangle$ of S_z , defined by $S_z|m\rangle = m|m\rangle$, where $m = -s, -(s-1), \dots, (s-1), s$. If the vectors $|m\rangle$ are used as a basis, the second term of Equations (2.23) or (2.25) has no diagonal elements, i.e. $\langle m|S_x^2 - S_y^2|m'\rangle = 0$ if $m = m'$. On the contrary, the first term of these Equations (2.23) or (2.25) has no off-diagonal elements.

It is apparent from Equation (2.24) that $D = 0$ when $D_{zz} = D_{xx} = D_{yy}$ (i.e. cubic symmetry). In axial symmetry, $D_{xx} = D_{yy}$, and thus $E = 0$. Equation (2.23) is then

$$\mathcal{H}_{\text{CF}} = DS_z^2. \quad (2.26)$$

Therefore, in axial symmetry, only the D parameter is needed to express the energies of the $(2S+1)$ spin levels of the S multiplet at this approximation. The effect of the Hamiltonian in Equations (2.23) and (2.25) is that of splitting the $(2S+1)$ levels even in the absence of an applied magnetic field. This effect is called zero-field splitting (ZFS).

If $|E|$ is sufficiently smaller than $|D|$, it is common to limit its variation as

$$-1/3 \leq E/D \leq +1/3. \quad (2.27)$$

From Equations (2.23) and (2.24), it is possible to obtain following expressions

$$D_{xx} = -D/3 + E; \quad D_{yy} = -D/3 - E; \quad D_{zz} = 2D/3. \quad (2.28)$$

For $E/D = 1/3$, $D_{xx} = 0$; $D_{yy} = -2D/3$; $D_{zz} = 2D/3$, and the splitting among these three components reaches its maximum (maximum rhombic splitting). At $E/D = 1$, $D_{xx} = D_{zz} = 2D/3$; $D_{yy} = -4D/3$. The x and z components are exactly the same, this means that the system is axial with y as the unique axis.

The eigenvectors of the Hamiltonian (2.26) in axial symmetry (if $E = 0$), are the eigenvectors $|m\rangle$ of S_z , and the eigenvalues are

$$W(m) = Dm^2 - S(S+1)/3. \quad (2.29)$$

At this approximation, $W(m) = W(-m)$. Including a non-zero E (i.e. reducing the symmetry below the axial one) the $|m\rangle$ and $| - m\rangle$ states remove their degeneracy if S is integer. On the contrary, they remain degenerate in pairs if S is half-integer. This is caused by time-reversal symmetry, and the pairs of degenerate levels are called Kramers doublets.

D can be either positive (levels with lowest $|m\rangle$ are the most stable) or negative (levels with the highest $|m\rangle$ lie lowest). Positive D corresponds to easy-plane magnetic anisotropy, negative D to easy-axis type magnetic anisotropy.

The Hamiltonian in Equation (2.21), which is quadratic in the S coordinates (spin components), represents the simplest possible crystal field Hamiltonian. Principally, it is necessary to include also fourth, sixth, etc. order terms in the Hamiltonian in order

2.2. SINGLE-MOLECULE MAGNETS (SMMS)

to sufficiently reproduce energy levels. The expansion is applicable only for even-order terms in zero field when calculating the effects on states of the same configuration. In fact, in this case the product of bra and ket is even, and thus only an even operator can give non-zero matrix elements. Therefore, it is unnecessary to include all the terms, it is sufficient to include only terms of order

$$N = 2, 4, 6, \dots, 2S. \quad (2.30)$$

Generally, a good approximation is obtained by considering that higher order terms are relatively smaller than the lower order terms. Formally, exact expansion can be done by including higher-order operators such as S_z^4 , S_x^4 , etc. The best way to exploit point group symmetry is to use so-called Stevens operator equivalents

$$\mathcal{H}_{\text{HO}} = \sum_{N,k} B_N^k \mathbf{O}_N^k \quad (2.31)$$

where the sum is over all N values defined in Equation (2.30) and the integer k satisfies

$$-N \leq k \leq +N. \quad (2.32)$$

B_N^k are parameters, and \mathbf{O}_N^k are so-called Stevens operators. The N numbers are limited according to Equation (2.30), while the k values depend on the point group symmetry.

By combining Equations (2.19), (2.25), and (2.31), the final spin-Hamiltonian can be obtained

$$\mathcal{H} = \mathcal{H}_Z + \mathcal{H}_{\text{CF}} + \mathcal{H}_{\text{HO}} = \mu_B \mathbf{B} \cdot \mathbf{g} \cdot \mathbf{S} + D \left[S_z^2 - \frac{1}{3} S(S+1) \right] + E(S_x^2 - S_y^2) + \sum_{N,k} B_N^k \mathbf{O}_N^k. \quad (2.33)$$

The spin anisotropy is expressed as the energy barrier that spins must overcome when they switch from parallel to anti-parallel alignment and can be written as $U_{\text{eff}} = |D|S^2$ for integer spin number, and $U_{\text{eff}} = |D|(S^2 - \frac{1}{4})$ for half-integer spin number [28]. Common units of U_{eff} are reciprocal centimetres [cm^{-1}]. In a simple approximation, the larger the value of U_{eff} , the longer the relaxation time will be, and thus this barrier determines the observation of single-molecule magnetism. Therefore, there are two parameters that can be changed in general, total spin number S and zero-field splitting parameter D , in order to increase the barrier. It was demonstrated, that it is convenient to focus on increasing D rather than S as there is a fundamental connection between D and S approximately given by $D \propto 1/S^2$ [29].

In conclusion, the SH approach provides only very approximative insight into description of magnetic interactions within molecular magnets. Important zero-field splitting parameters D and E are crucial for characterisation of single-molecule magnets by spectroscopic methods such as paramagnetic electron resonance.

2.3. Langmuir–Blodgett Films

The structure of this section follows book: Langmuir–Blodgett Films: An Introduction [30], and PhD thesis: A Modified Langmuir–Schaefer Method For the Creation of Functional Thin Films [31]. The history of a monolayer-thick film started hundreds of years ago. Already ancient Babylonians created patterns by spreading oil on water surface. The first technical application of floating organic films dates back to 12th century when coloured dyes composed of sub-micrometer particles (ink) mixed with proteins were spread on a water surface to create patterns. Subsequent horizontal dipping of a paper onto an air-water interface created unique drawings³. Detailed report on molecular layers was given by Benjamin Franklin in the first scientific report on surface chemistry in 1774. During his observations of wave attenuation on a water surface (thought to be caused by leaking oil around ships) he noticed a calming effect of oil on water. After depositing a small amount of oil onto a water surface he observed that area covered by oil layer was left unaffected by wind and had attenuating effect on the water surface. If Franklin had calculated the thickness of the oil layer created from volume of roughly 2 mL spreading over 2000 m², he would have found that the layer was approximately 1 nm thick.

The next contributor was Lord Rayleigh, who attempted to measure accurately the quantity of olive oil, which was needed to cover a water surface. He found that 0.81 mg of olive oil was needed to cover an area of 555 cm² resulting in a 16 Å thick layer. This length appeared to be a monomolecular layer of the triolein molecule (C₅₇H₁₀₄O₆) which constitutes olive oil. Significant progress was also made by German scientist Agnes Pockels who created the prototype of today well-known so-called Langmuir–Blodgett through (shallow container with movable barriers which are used to sweep the surface clean and to compress or relax any thin film).

Finally, the crucial step was made by Irving Langmuir who introduced a novel concept about molecular conformation at the air/water interface⁴. He also mentioned possibility to transform such a layer at the air/water interface onto a substrate. This was, however, done afterwards by Katherine Blodgett and published in the Journal of the American Chemical Society (JACS) in 1934 and 1935, respectively. This milestone denoted birth of Langmuir–Blodgett (LB) deposition method and Langmuir film being the expression ascribed to the monomolecular layer at the air/water interface. LB deposition refers to an approach where the sample plate is lowered into the through vertically. If the sample is inserted horizontally, the technique is called Langmuir–Schaefer (LS). The rebirth of LB and LS deposition starts in 1980s and with numerous modifications still provides reasonable deposition technique.

2.3.1. Thermodynamic Equilibrium

When an arbitrary thermodynamic system is left to itself, properties such as (p – pressure, V – volume, T – temperature) generally change in time. This system, however, after sufficiently long time will reach a state of thermodynamic equilibrium. The equilibrium is achieved when the free energy is minimised. For systems at constant volume, this is expressed by the Helmholtz function F

$$F = U - TS \tag{2.34}$$

³Known as Sumi Nagashi - paper marbling method of Japanese origin.

⁴The Nobel Prize in Chemistry 1932 – "for his discoveries and investigations in surface chemistry".

and for constant pressure changes, the free energy is given by the Gibbs' function G

$$G = H - TS = U + pV - TS \quad (2.35)$$

where enthalpy H is basically the sum of all the potential and kinetic energies in a system

$$H = U + pV \quad (2.36)$$

and U is the internal energy of a system. In both Equations (2.34) and (2.35) mentioned above, S is the entropy. Normally, this represents the heat into or out of a system divided by temperature

$$\Delta S = \frac{\Delta H}{T} \quad (2.37)$$

and is also a measure of the disorder of a thermodynamic system. Equations (2.34) and (2.35) suggest that free energy can be minimised either by reducing the internal energy or by increasing the entropy. At low temperature, the internal energy of the molecules contributes more to the free energy. On the contrary, at high temperature, the entropy of the system becomes the predominant influence. Consequently, fluid phases are stable at elevated temperatures even though they constitute higher internal energy configurations than the solid state.

2.3.2. Gas–Liquid Interface

Certain molecules can orient themselves at the gas/liquid interface in order to minimise their free energy. The resulting surface film with thickness of one molecule is often referred to as a monomolecular layer or monolayer. The boundary between a liquid and a gas phase (e.g. air/water interface) marks a transition between the composition and properties of two different bulk phases. The thickness of this region is of the utmost importance, because this is the region, where all the processes take place. A molecule at the surface is surrounded by fewer molecules than one in the bulk liquid (see Figure 2.8). Molecules will therefore diffuse initially from the surface. The activation energy for a surface molecule escaping into the bulk will increase until it is equal to the energy of molecules diffusing from the bulk to the surface, and finally reaching a state of equilibrium. The line force acting on the surface molecules is the surface tension γ .

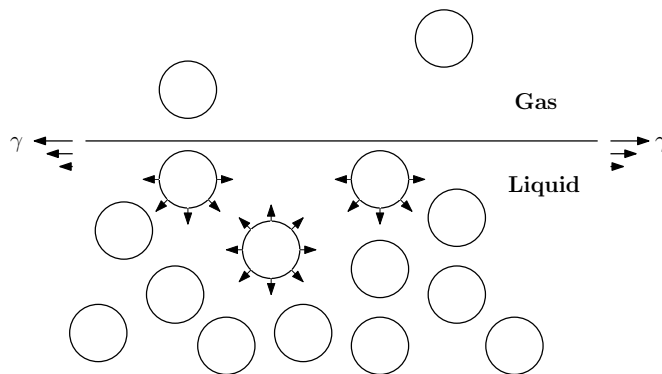


Figure 2.8: Forces in the bulk liquid and at the liquid/gas interface.

At thermodynamic equilibrium, the surface tension of a planar interface can be expressed as partial derivatives of the free energy functions with respect to the area A of the surface

$$\gamma = \left(\frac{\partial F}{\partial A} \right)_{T, V, n_i} = \left(\frac{\partial G}{\partial A} \right)_{T, p, n_i} \quad (2.38)$$

2. THEORY

where p , V , T are intensive properties and n_i is an extensive property (e.g. number of moles, entropy, internal energy).

Surface tension γ is similar to vapour pressure, it remains constant for two phases in equilibrium at the constant temperature, but changes with changing temperature. Unlike the vapour pressure, which increases with increasing temperature, γ decreases with increasing temperature and becomes zero at the critical point. The presence of a monolayer on a liquid surface affects the surface tension. Therefore, it is convenient to introduce surface pressure Π

$$\Pi = \gamma_0 - \gamma \quad (2.39)$$

where γ_0 is the surface tension of the pure liquid and γ is the surface tension of the film-covered surface.

2.3.3. Monolayer Formation

All compounds can be roughly divided into those that are soluble in water and those that do not dissolve in water. The former compounds are generally polar, their charge is unevenly distributed. Such molecules possess an electric dipole moment⁵ μ . Figure (2.9) shows the case for a water molecule. Each of the two hydrogen atoms share an electron pair with the oxygen atom. The geometry of the shared electron pairs in the outer shell of the oxygen causes the V-shape of a water molecule. The strong electron-withdrawing ability of oxygen causes a local negative charge in the vicinity. Even though the water molecule as a whole is electrically neutral, its positive and negative charges are widely separated.

The solvent properties of water are closely related to the attraction between its electric dipoles and the charges associated with the solute. The molecules of most monolayer-forming materials are composed of two main parts: one part is a water soluble (hydrophilic = water-loving) and the opposite one is (hydrophobic = water-hating). These molecules are called amphiphiles, the most important representatives are soaps and phospholipids.

Water is one of the most wide-spread and common solvents, and thus it is important to thoroughly describe its properties. In addition, water is also usually used in LB through as a sub-phase (i.e. majority liquid which takes part in a deposition process). Unfortunately, coordination metal complexes, as well as graphite, are not soluble in water. Therefore, it is necessary to use specific organic solvents (e.g. chloroform, dichloromethane, dimethylformamide) in order to dissolve these compounds. When such a material is first applied onto the water surface, spreading will continue until the surface pressure reaches an equilibrium value. This happens spontaneously and generally the material is being added as long as it tends to spread observably on the water surface.

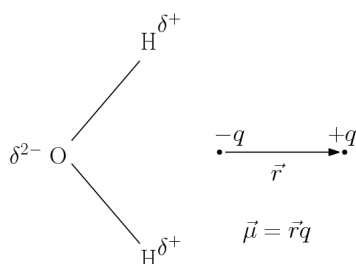


Figure 2.9: Origin of electric dipole moment μ in a water molecule.

⁵The SI unit of electric dipole moment is [C·m], it is, however, common to use Debye unit ($1\text{ D} \doteq 3.336 \times 10^{-30}\text{ C} \cdot \text{m}$), electric dipole moment of water is 1.85 D.

When the monolayer is compressed on the water surface, it will undergo phase transformations. These changes can be observed by monitoring the surface pressure Π as a function of the area occupied by the film. This diagram is shown in Figure (2.10) and is unique for every substance and gives information about formation of the monolayer. Therefore, it is the very first step in the investigation of a new material created at the air/water interface. It is common, in such a plot, to divide the film area A by the total number of molecules N on the water surface to obtain the area per molecule

$$a = \frac{A}{N} = \frac{A}{nN_A} = \frac{AM}{m} \cdot N_A = \frac{AM}{cVM} \cdot N_A = \frac{AN_A}{cV} \quad (2.40)$$

where n is the amount of a solute in moles, N_A is the Avogadro constant⁶, m is mass of a solute, M is the molecular weight of a solute, c is the specific molar concentration of a solution, and V is its volume. It is convenient to obtain the last expression on the right side of above mentioned equation (2.40) for further calculations in the experimental section of this thesis (3.5.2. Isotherms).

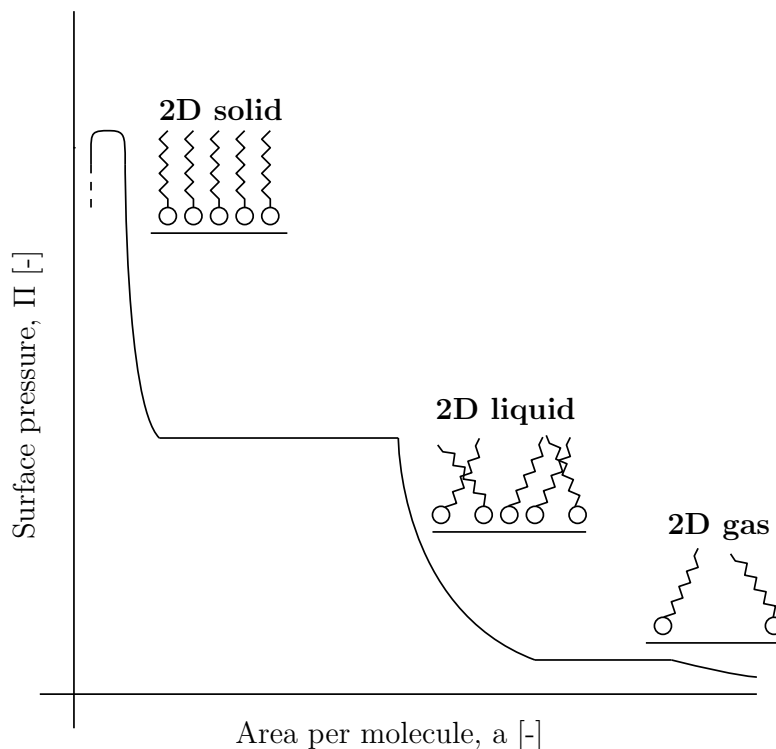


Figure 2.10: Illustration of surface pressure versus area per molecule diagram.

Equation (2.40) is derived from a model by using two-dimensional variation of conventional kinetic theory. The molecules in the film can move with an average translational kinetic energy of $k_B T/2$ for each degree of freedom. This leads to the following equation for an ideal 2D gas

$$\Pi a = N k_B T \quad (2.41)$$

where Π is the surface pressure, a is the area per molecule, N is number of molecules, and k_B is the Boltzmann constant⁷, and T is the absolute temperature.

⁶Avogadro constant in SI units: $N_A \doteq 6.022 \times 10^{23} \text{mol}^{-1}$.

⁷Boltzmann constant in SI units: $k_B \doteq 1.381 \times 10^{-23} \text{J} \cdot \text{K}^{-1}$.

2. THEORY

2.3.4. Surface Pressure Measurement

The surface pressure Π is usually measured by so-called Wilhelmy plate. Figure (2.11) shows the principle which is as follows: a plate, very often made out of paper, is partially immersed in water. The force acting on this plate is sum of three force contributions; the gravity F_G and the surface tension F_{ST} , both are acting downwards, whereas the buoyancy F_B of the plate is acting upward. This can be expressed by following equations

$$F = F_G + F_{ST} - F_B \quad (2.42)$$

$$F = m_p g + \gamma \cos \alpha P - m_l g \quad (2.43)$$

for a rectangular plate of dimensions l_p , w_p , t_p , material density ρ_p , and perimeter P immersed to a depth h in a liquid of density ρ_l the net force is given by

$$F = \rho_p g l_p w_p t_p + 2\gamma(t_p + w_p) \cos \alpha - \rho_l g t_l w_l h \quad (2.44)$$

where γ is the surface tension of the liquid, α is the contact angle on the solid plate and g is the gravitational constant. By this approach it is possible to measure surface pressure by measuring the change of force F acting on a plate with and without a molecular film at the surface. During a deposition, Wilhelmy plate is completely wetted after a while, that means $\alpha = 0$ and $\cos 0 = 1$. The surface pressure can be subsequently obtained from following equations

$$F_0 = F_G + 2\gamma_0(t_p + w_p) - F_B \quad (2.45)$$

$$F = F_G + 2\gamma(t_p + w_p) - F_B \quad (2.46)$$

giving the final relation for surface pressure connecting the change in force and the change in surface tension

$$\Pi = \gamma_0 - \gamma = \frac{F_0 - F}{2(t_p + w_p)}. \quad (2.47)$$

The sensitivity can be increased by using a very thin plate, so that $t_p \ll w_p$, and giving the following equation

$$\Delta\gamma = \frac{\Delta F}{2w_p}. \quad (2.48)$$

The force is then determined by measuring the changes in the mass of the plate, which is directly coupled to a sensitive microbalance.

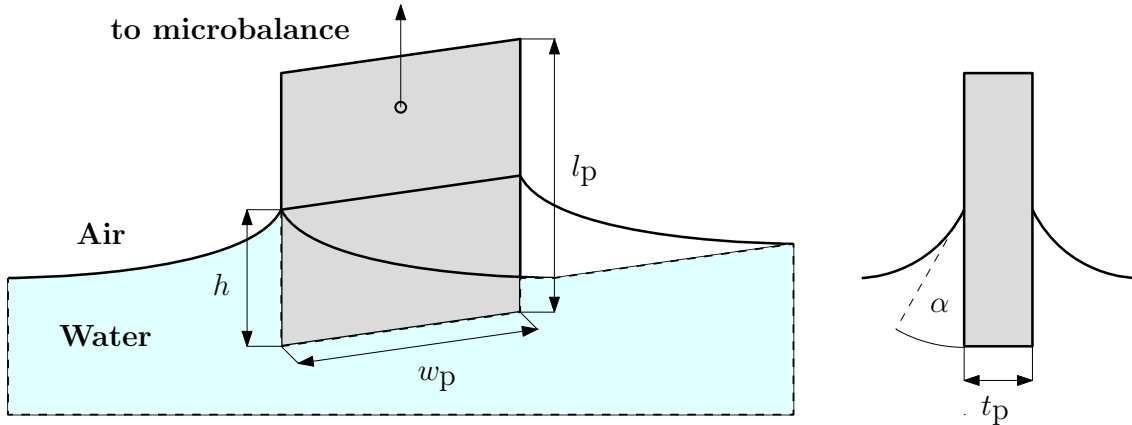


Figure 2.11: A Wilhelmy plate: the perspective view and the side view.

2.4. Electron Paramagnetic Resonance (EPR)

The chapter about electron paramagnetic resonance (EPR), also sometimes called electron spin resonance (ESR), aims to provide basic principles behind this spectroscopic method with an illustrative example of experimental set-up. The notation is taken from the books: *Electron Paramagnetic Resonance: Theory and Fundamental Applications* [32] and *Electron Spin Resonance* [33].

2.4.1. Basic Principles and Historical Background

The concept of EPR is similar to more widespread nuclear magnetic resonance (NMR). Both methods are based on interaction between electromagnetic radiation and magnetic moments. However, in the case of EPR, the magnetic moments arise from electrons rather than nuclei. The structure of a matter is revealed by analysing absorption spectra. They are obtained by measuring of attenuation versus frequency (wavelength) of an electromagnetic radiation passing through a sample. Lines and bands in spectra represent transitions between energy levels of the absorbing sample.

Figure (2.12) shows propagation of electromagnetic radiation as coupled electric \vec{E} and magnetic \vec{B} field perpendicular to the direction of propagation \vec{k} . Both fields oscillate at a frequency ν . In EPR, commonly frequencies of $10^9 - 10^{12} \text{ s}^{-1}$ (1 – 1000 GHz) are used.

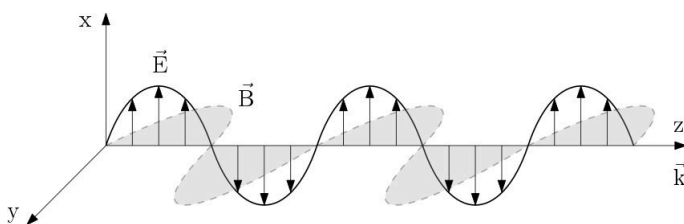


Figure 2.12: Illustration of propagating plane-polarised and monochromatic electromagnetic wave with propagation vector \vec{k} along z .

The electromagnetic radiation can be imagined as a stream of photons. The energy of a photon is given by $h\nu$, where h is Planck constant⁸. When a photon is absorbed or emitted by an electron, atom, or molecule, the energy and angular momentum of the system must be conserved.

In usual spectroscopic studies it is the electric field component of the radiation which interacts with molecules. There are two conditions, that must be fulfilled for absorption to occur:

1. The energy $E = h\nu$ of a radiation quantum must correspond to the energy separation between certain energy levels in the molecule.
2. The oscillating electric-field component of \vec{E} of electromagnetic radiation must be able to interact with an oscillating electric-dipole (or higher order) moment.

Likewise, a molecule with a magnetic dipole is expected to interact with the oscillating magnetic component of \vec{B} of electromagnetic radiation. This is a basic concept for magnetic-resonance spectroscopy. Commonly, in the case of EPR, there is also an external magnetic field \vec{B}_{ex} applied.

⁸Planck constant in SI units: $h \doteq 6.626 \times 10^{-34} \text{ J} \cdot \text{s}$.

2. THEORY

Every electron possesses own intrinsic magnetic-dipole moment arising from its spin. In most systems, electrons are paired in such a way that the net moment is zero. Therefore, only systems with one or more unpaired electrons possess non-zero net spin moment, which is necessary for desired interaction with an electromagnetic field. A magnetic-dipole moment in an atom or molecule (both neutral and charged) can arise from unpaired electrons or from magnetic nuclei. The magnetic-dipole moments of these particles originate from electronic or nuclear angular momenta. Thus, it is important to understand the nature and quantisation of angular momenta when dealing with EPR spectroscopy.

The origin of EPR technique can be treated as an extension of the famous Stern–Gerlach experiment. They demonstrated in 1920s, that an electron magnetic moment in an atom can acquire only discrete orientations in a magnetic field, in spite of the sphericity of the atom. Subsequently, Uhlenbeck and Goudsmit connected the electron magnetic moment to the electron spin angular momentum. The next contributors were Breit and Rabi that described the energy levels of a hydrogen atom in a magnetic field. In fact, Rabi et al. studied transitions between levels induced by an oscillating magnetic field. This was the first observation of magnetic resonance.

Finally, the first observation of an electron paramagnetic resonance peak was made in 1945 by Zavoisky who detected a radiofrequency absorption line from a $\text{CuCl}_2 \cdot 2\text{H}_2\text{O}$ sample. He discovered a resonance at the magnetic field $B = 4.76 \text{ mT}$ for a frequency $\nu = 133 \text{ MHz}$. For this case, the Zeeman factor g is approximately 2. Lately, Frenkel interpreted Zavoisky’s results as showing paramagnetic resonance absorption. Subsequent experiments with higher magnetic fields of $100 - 300 \text{ mT}$ demonstrated the advantage of using high fields and frequencies.

The rapid development of paramagnetic resonance started after World War II (ended 1945) due to widespread availability of microwave technology used for military purposes. For instance, technology for 9-GHz (X band: $8 - 12 \text{ GHz}$) region was widely used for radar, and thus components were easy to obtain at reasonable cost. Nowadays, state-of-the-art instruments for EPR detection benefit from development of related field such as computers, microwave sources, precise machining, and detection devices. All of this pushes every upcoming EPR instrument to a higher level and allows a deeper, quicker, and more sophisticated investigation into a matter.

Figure (2.13) shows the simplest energy-level diagram in case of EPR studies for a particle with spin $\frac{1}{2}$ (e.g. electron) in a magnetic field.

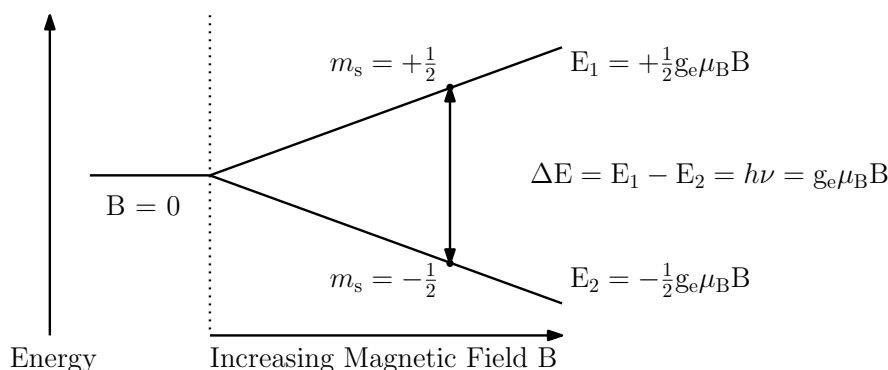


Figure 2.13: Scheme of energy-level diagram for a free electron as a function of applied magnetic field B illustrating EPR absorption. E_1 and E_2 are energies corresponding to $m = \pm\frac{1}{2}$ states. s is the characteristics of a particle, an electron in this case. $g_e \doteq 2.00232$ is the g factor for an electron, μ_B is the Bohr magneton, and h is the Planck constant.

2.4. ELECTRON PARAMAGNETIC RESONANCE (EPR)

By varying the magnetic field, it is possible to change the energy-level separation. Resonant absorption is observed for the frequency satisfying $E = h\nu$, where ν is the frequency of incident electromagnetic radiation (usually microwave region). The magnitude of the transition equals to the energy that must be absorbed from the radiation in order to excite the lower state to the upper state. Usually, many simple unpaired-electron systems require field of approximately 0.3 T and $\nu = 9$ GHz for the resonance to occur.

2.4.2. Scope of EPR

In majority of EPR spectroscopy, the electron magnetic dipole arises mainly from spin angular momentum with only a small contribution from orbital motion. Resonant absorption of electromagnetic radiation by a system is called 'electron paramagnetic resonance' or 'electron spin resonance'. The term resonance describes exactly what happens since the well-defined separation of energy levels matches to the energy of a quantum of incident radiation. The term electron paramagnetic resonance (EPR) takes into account contributions from electron orbital as well as spin angular momentum.

In any system consisting of atoms or molecules, there is a tremendous amount of electronic states for standard optical spectroscopy. In the case of EPR, however, the energy of photons is very low (e.g. 9 GHz = 0.0372 meV). Therefore, it is possible to ignore the plethora of electronic states except for the ground state and nearby excited states. This uniqueness allows this technique to be widely applicable to any system in a paramagnetic state (or system that can be placed in such a state), meaning the state having net electron angular momentum (typically spin angular momentum). Many systems already exist in a paramagnetic ground state, the rest can be excited into a paramagnetic state, for instance, by irradiation. Principally, all atoms and molecules are amendable to be studied by EPR spectroscopy. List of typically examined systems is as follows:

1. Free radicals in the solid, liquid or gaseous phases. A free radical can be an atom, molecule or ion containing one unpaired electron.
2. Transition ions including actinide ions. Can contain up to five or seven unpaired electrons.
3. Point defects (localised imperfections, trapped electrons, electron vacancies - positive holes).
4. Systems with multiple unpaired electrons: (a) Triplet states - systems with strong interaction between two unpaired electrons. (b) Biradicals - systems with weak interaction between two unpaired electrons. (c) Multiradicals - systems with more than two unpaired electrons interacting.
5. Conducting electrons in semiconductors and metals.

EPR method is very sensitive spectroscopic method with wide applicability. Consequently, it is of great importance to thoroughly investigate EPR spectra that provide significant chemical information. In most set-ups, the first derivative of absorption signal is measured. This is caused by the use of so-called 'lock-in' amplifier, which enables to separate very weak signal from a sample from a noise. In an experiment, alternating current (AC) modulation with known noise frequency, surrounding the sample, is applied.

2. THEORY

To interpret EPR spectra properly, it is necessary to consider basics of quantum mechanics, especially the part associated with angular momentum. There are a few points that are helpful to bear in mind when treating EPR spectra, it is necessary to:

1. Analyse the energy levels of the system and the influence of the surrounding environment affecting these levels: (a) Theoretical treatments and approximations are often necessary to obtain plausible interpretation of the data of organic free radicals and π -electron free radicals, (b) the knowledge of the splitting of orbital and spin energy levels by local electric fields of various symmetries is important for investigation of transition-ion spectra.
2. Realise that some systems behave isotropically (their properties are independent of magnetic field orientation). Nevertheless, most systems behave anisotropically (their energy-level separations and properties depend on orientation in an applied magnetic field).
3. Consider time-dependent phenomena, such as decay of paramagnetic species, molecular motions, changes in population polarisation of spin states, chemical, and electron exchange leading to inner sample kinetics.

Figure (2.14) shows the net energy flow in a sample during an EPR experiment beginning by the excitation source and ending by the thermal motions of the atoms at the surroundings of the sample. The appearance of EPR spectral lines and the ability to detect them is dependent on the energy flow throughout the system.

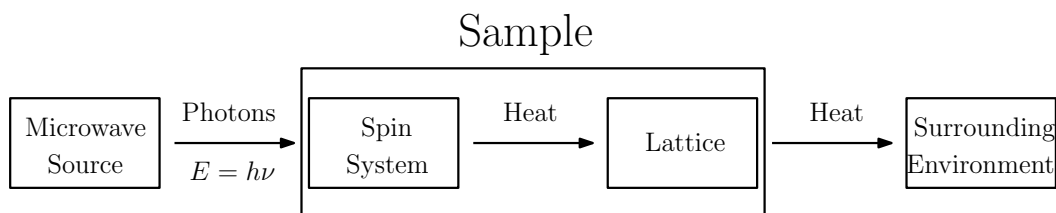


Figure 2.14: Energy flow in an EPR experiment. The spin system is irradiated by incident photons at frequency ν . The absorbed radiation is at exponential rate dissipated by diffusion to the lattice, which allows continuous absorption of photons by a sample. Finally, energy is transferred from the sample to the surrounding environment.

The coupling between the spins of a system and the lattice is measured by a characteristic spin-lattice relaxation time τ_1 . The magnitude of observed EPR signal is proportional to the polarisation of all spin orientations within a sample. The system is considered as saturated when the rate of upward and of downward transitions is equalised. In this case no energy is transferred between incoming radiation and the spin system. If the electron spin-lattice relaxation time τ_1 is very long, it is necessary to make observations at very low microwave power to avoid saturation of a system. On the contrary, very short τ_1 , lifetime broadening may get very large so that the line is broadened too much, and thus undetectable. This issue of optimal spin-lattice relaxation time is usually solved by measuring at very low temperatures (units of K), since the τ_1 tends to increase rapidly with decreasing temperature.

2.4.3. Angular Momentum and Relation to Magnetic Moment

As mentioned in the previous section, understanding of quantisation of angular momentum is essential for EPR studies. This section aims to provide brief introduction into the origin of such a quantisation starting with a classical angular momentum.

Classically, angular momentum is defined as

$$\vec{L} = \vec{r} \times \vec{p} \quad (2.49)$$

where $\vec{p} = m\vec{v}$ is the momentum of a particle with mass m and velocity \vec{v} .

In quantum mechanics, however, the total (or generalised) angular momentum operator $\hat{\mathbf{J}}$ can be written as

$$\hat{\mathbf{J}} = \hat{\mathbf{L}} + \hat{\mathbf{S}} \quad (2.50)$$

where $\hat{\mathbf{L}}$ is orbital angular-momentum operator and $\hat{\mathbf{S}}$ is the spin angular-momentum operator.

At this place, it is important to note that all of operators mentioned in Equation (2.50) are quantised

$$\hat{\mathbf{L}} = \hbar[L(L+1)]^{1/2} \quad L = 0, 1, 2, \dots \quad (2.51)$$

$$\hat{\mathbf{S}} = \hbar[S(S+1)]^{1/2} \quad S = 0, \frac{1}{2}, 1, \frac{3}{2}, \dots \quad (2.52)$$

$$\hat{\mathbf{J}} = \hbar[J(J+1)]^{1/2} \quad J = 0, \frac{1}{2}, 1, \frac{3}{2}, \dots \quad (2.53)$$

where $\hbar = \frac{h}{2\pi}$ is the reduced Planck constant, J is the angular-momentum quantum number, and S the spin quantum number. The allowed values of the component of $\hat{\mathbf{J}}$ are restricted by the quantum number m_J , with increments of $-J$ to $+J$. This gives in total $2J + 1$ possible components.

The quantisation phenomena arise from Heisenberg uncertainty principle, as it can be shown, that it is possible to measure one projection and the square of the operator at the same time (e.g. \hat{L}_z, \hat{L}^2). This is best understood by the operation of commutation. Two operators commute if

$$[\hat{A}, \hat{B}] = \hat{A}\hat{B} - \hat{B}\hat{A} = 0. \quad (2.54)$$

Commuting quantities can be measured at the same time. This is, however, not the case of individual components of angular momentum.

$$[\hat{L}_x, \hat{L}_y] = i\hbar\hat{L}_z. \quad (2.55)$$

The same applies for other variations of components. They do not commute, and thus they cannot be measured at the same time.

On the contrary, an arbitrary projection and square

$$[\hat{L}_z, \hat{L}^2] = 0 \quad (2.56)$$

commute, and thus they can be measured at the same time. Therefore, it is relevant to consider arbitrary projection or square of quantised angular-momentum components [32], [34].

2. THEORY

Figure (2.15) shows a projection of two different spin angular momenta for (a) $S = \frac{1}{2}$ and (b) $S = 1$. States with $S = \frac{1}{2}$ are called doublet states, because their multiplicity $2S + 1$ is equal to 2. This first example represents also a case for a free radical. States with $S = 1$ are called triplet states. In the case of EPR, states with $S > \frac{1}{2}$ are common. Moreover, EPR transitions do not change the value of S .

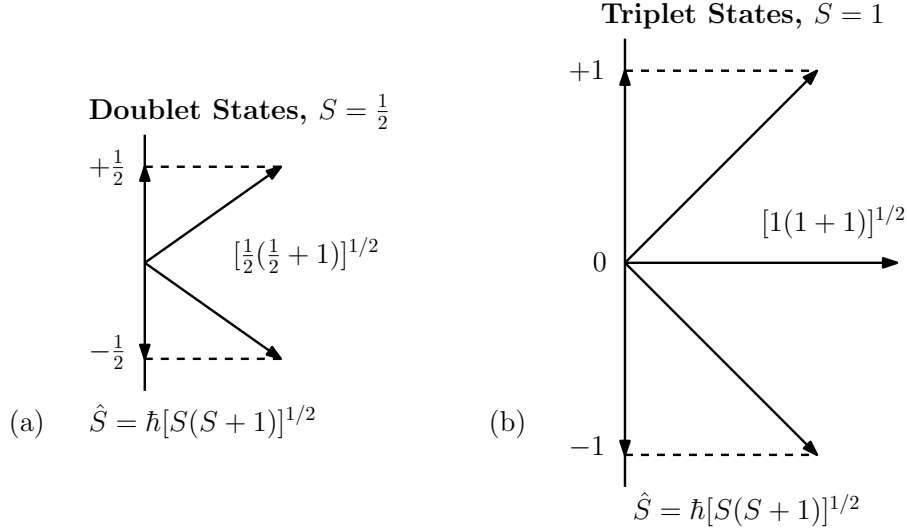


Figure 2.15: Quantisation of the total spin angular momentum $\hat{\mathbf{S}} = \hbar[S(S+1)]^{1/2}$ in units of \hbar and its component m_S for (a) $S = \frac{1}{2}$, and (b) $S = 1$.

The magnetic moment and angular momentum are proportional to each other, in both classical and quantum mechanics. In analogy of an orbital magnetic dipole, classical particle with mass m and charge q rotating with speed v in a circle of radius r , is taken to lie in the xy plane. The circulating electric current i is a magnetic field equivalent to the field produced by a point magnetic dipole. This dipole has a moment iA and is normal to the plane with $A = \pi r^2$ being the area of the circle. The charge flow per unit time (effective current) is $i = qv/2\pi r$. The magnetic moment pointing along z can be then expressed as

$$\mu_z = iA = \pm \frac{qv\pi r^2}{2\pi r} = \pm \frac{q}{2m} mvr = \frac{q}{2m} l_z \quad (2.57)$$

where l_z is the orbital angular momentum along the axis z and the sign choice depends on the direction at which the particle rotates. The proportionality constant is $\gamma = q/2m$ which is called the gyromagnetic ratio (units in SI: $\text{C} \cdot \text{kg}^{-1} = \text{s}^{-1}\text{T}^{-1}$). This factor γ converts angular momentum to magnetic moment. Therefore, every integral multiple \hbar of orbital angular momentum has an associated orbital magnetic moment with magnitude $\beta = |q|\hbar/2m$. This is the origin of the Bohr magneton for an electron which is given by

$$\beta_e = \mu_B = \frac{e\hbar}{2m_e} \doteq 9.274 \times 10^{-24} \text{J} \cdot \text{T}^{-1}. \quad (2.58)$$

To sum up, in order to treat EPR data, it is necessary to take into account quantum mechanics, governing the nano-scale, with its peculiar and often strange behaviour in comparison to our everyday experience. Especially, the g factor plays a vital role in the EPR spectroscopy, it can be imagined as a dimensionless magnetic moment. It is a unique characteristic of examined material. For an electron $|g_e| = 2.00231930436182$, it is one of the most precisely determined physical constant up to date [35].

2.4.4. EPR Spectrometer

This section is devoted to illustration of how such an EPR spectrometer can look like. It is important to realise, that there is a large variety of set-ups and instruments worldwide in comparison with NMR spectrometers. This is related to relatively slower development of EPR method unlike NMR, that gained a solid place in medical facilities and became a standard instrument.

Figure (2.16) shows an EPR spectrometer. This represents an example of continuous-wave (cw) arrangement. There are four main parts of such set-up, microwave source, resonator, magnetic field, and detector.

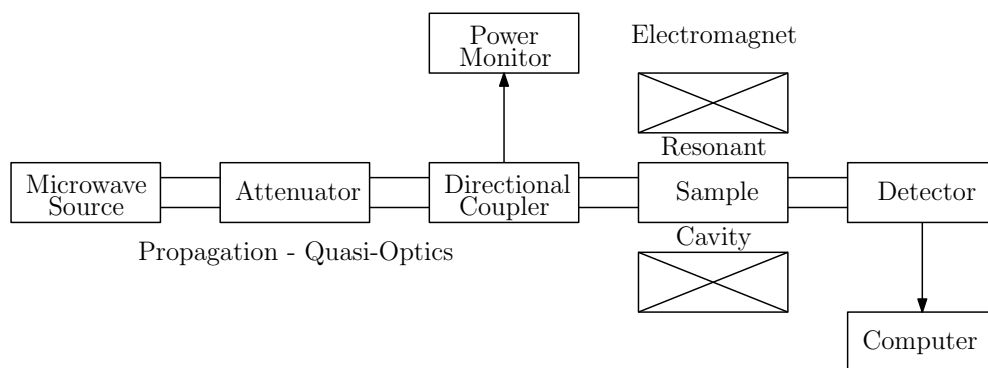


Figure 2.16: Block diagram of possible EPR spectrometer appearance.

Microwave source: The high-power microwave is usually generated inside specialised vacuum tube. The energy transmission is typically realised by special coaxial cables or by waveguides. The most common operating frequencies of EPR spectrometers for different wavebands are: X – band (9.5 GHz), Q – band (35 GHz), W – band (95 GHz), and also high frequency EPR (HFEPR) with $\nu > 100$ GHz are possible nowadays. Frequencies $\nu > 100$ GHz can be realised by microwave synthesiser with subsequent amplification and multiplication.

Resonator: This part is usually constructed as a resonant cavity in which a sample is located during an experiment. The resonant frequency is defined by the dimensions of cavity and the microwave source is tuned to satisfy its resonance conditions.

Magnetic Field: Standard EPR spectrometers usually use static magnetic field provided by resistive magnets cooled by water or by superconducting magnets cooled by liquid nitrogen and helium. It is essential to secure stability and avoid interference with other devices in order not to influence a measurement, as well as prevent interference with devices (e.g. cardiostimulators and other electronic and magnetic devices). This can be partially solved by letting the magnet into a ground floor.

Detector: There is a wide variety of solid-state detectors sensitive to microwave energy working as p–n junction. Absorption lines in the EPR spectrum are observed when the separation of two energy levels is equal to (or very close to) the quantum of an incident microwave photon, $E = h\nu$. The absorption of such photons by a sample is then indicated as a change in the detector current. It is also possible to use a bolometer, which is a device for measuring electromagnetic radiation via small heating of a material with a temperature-dependant electrical resistance, from which current can be obtained.

2.5. Raman Spectroscopy

The following section about Raman spectroscopy provides theoretical minimum in order to explain experimental results, what is measured, and how. This spectroscopy was, as the title suggest, comprehensively investigated and described by the Indian scientist C. V. Raman in 1928⁹.

Figure (2.17) shows schematically the basics of Raman scattering. A sample is irradiated by incident monochromatic source (laser). This light is absorbed by the sample and leads to energy transitions (excitation) in the sample with subsequent de-excitation, light emission. The origin of Raman scattering is inelastic scattering of an incident photon. It is a two-photon process during which an annihilation and creation of photon occurs. Molecular modes observed by this method are especially molecular vibrations that are characterised by frequency Ω . Every molecule has its own spectra originating from different vibrational modes, and thus Raman scattering can be imagined as a chemical fingerprint of a molecule [36].

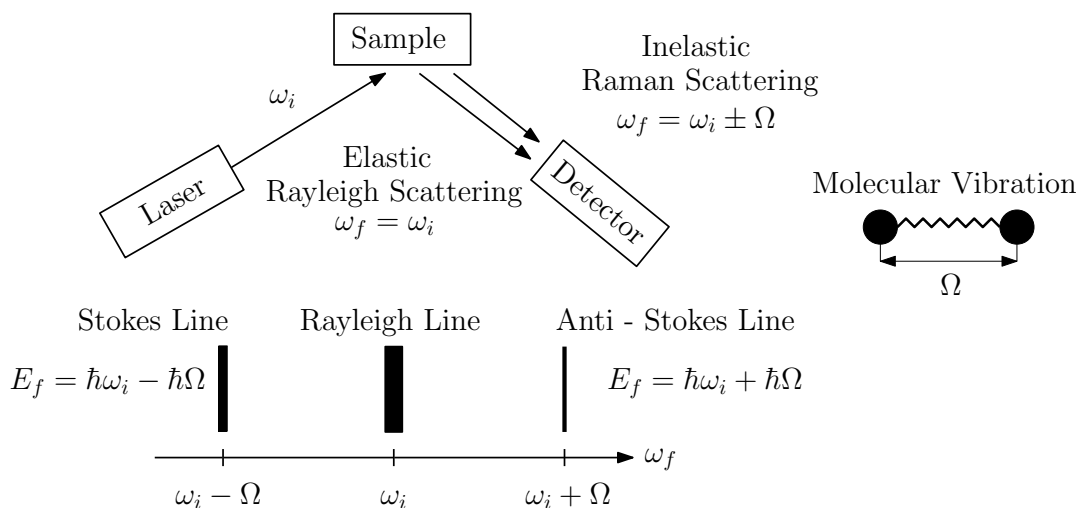


Figure 2.17: Scheme of Raman scattering in a sample. For the case of elastic scattering, Rayleigh line is observed. Inelastic scattering gives origin to Raman signal, there are two observable lines. The first are Anti-Stokes lines that have higher energy and the second are Stokes lines with lower energy.

In a typical Raman spectroscopy measurement, spectra show vibrational frequency in wavenumbers [cm^{-1}]. Peaks indicate specific chemical "groups" (i.e. types of bonds). Usable energy range for the Raman scattering is typically $200 - 4000 \text{ cm}^{-1}$. The effect as such is very weak, approximately only 1 in 10^7 of incident photons is inelastically scattered and contributes to Raman signal. It is also common to consider only Stokes lines, as they have higher probability of occurrence compared to Anti-Stokes lines. This is given by Boltzmann distribution

$$p_i = \frac{e^{\frac{-\varepsilon_i}{k_B T}}}{\sum_{i=1}^M e^{\frac{-\varepsilon_i}{k_B T}}} \quad (2.59)$$

⁹1930 – The Nobel Prize in Physics "for his work on the scattering of light and for the discovery of the effect named after him"

where p_i is the probability of states i , ε_i the energy of state i , k_B the Boltzmann constant, T the absolute temperature of the system, and M is the number of states accessible to the system [37].

Therefore, as shown in Figure (2.17), Stokes lines have lower energy, and hence higher probability of occurrence. The spectra are usually plotted as intensity or counts per second (photons hitting a detector) against Raman shift given in wavenumbers [cm^{-1}] as

$$\Delta\omega = \frac{1}{\lambda_{\text{incident}}} - \frac{1}{\lambda_{\text{scattered}}} \quad (2.60)$$

where $\lambda_{\text{incident}}$ is the wavelength of incident light and $\lambda_{\text{scattered}}$ is the wavelength of inelastically scattered light going to the detector, which is usually a charge-coupled device (CCD) camera.

The choice of wavenumbers is apparent as it can be taken as a unit of energy. Figure (2.18) illustrates an example of Si/SiO₂ substrate with highlighted bands. The low signal near zero comes mainly from the laser source and elastic Rayleigh scattering. These signals are, however, very strong in comparison with Stokes lines, and thus they are filtered out in the Raman set-up, usually by so-called notch filter which is a band-stop filter for eliminating this huge signal. The main silicon phonon band at approximately 520 cm^{-1} is cut off in order to include other less intense signals from transversal acoustic (TA) and transversal optic (TO) phonon bands [38].

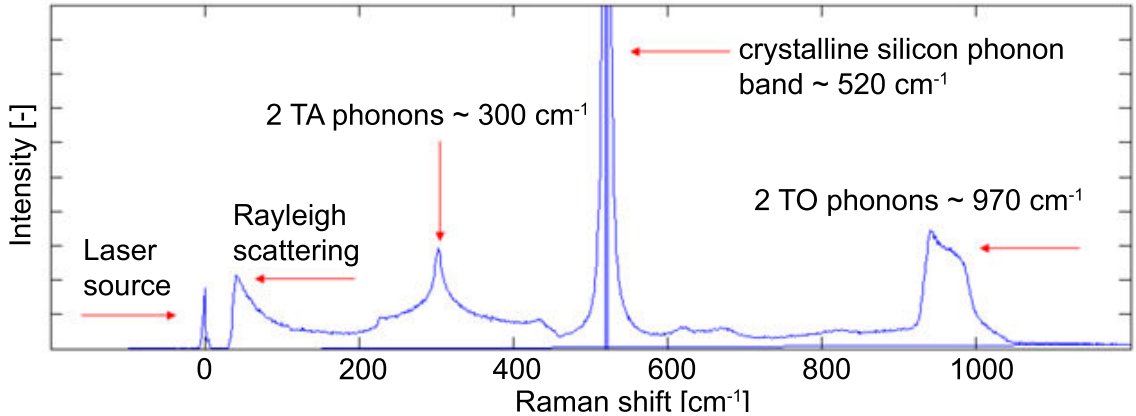


Figure 2.18: Example of Raman spectra for Si/SiO₂ substrate. Here are only Stokes lines visible, because they produce stronger signal in comparison with Anti-Stokes lines.

In summary, Raman spectroscopy is a very sensitive spectroscopic method enabling investigation of chemical bonds in a sample based on transition from the ground state vibrational energy level and ending at a higher vibrational energy level (Stokes scattering). It provides a specific chemical fingerprint of a material with fast spectra acquisition in the order of minutes along with easy sample preparation. One of the main advantage is the possibility to examine carbon-based samples (e.g. organic molecules, graphene). Therefore, it is widely used for confirmation of prepared molecular structure, as well as examining the degree of crystallinity in solid-state materials or estimating the quality of prepared structure (defects), that are also visible in the spectra.

2.6. Scanning Electron Microscopy (SEM)

This last section of theoretical chapter is written to provide brief introduction into the scanning electron microscopy for understanding images shown in experimental part. Primarily, why is it convenient to use a focused electron beam for the material characterisation.

The main advantage of SEM is the use of electrons instead of light in conventional optical microscopy. The physical interpretation of its principal advantage over light is most elegantly dealt with by taking into account quantum mechanics, especially the de Broglie hypothesis, which introduces wave-particle duality (i.e. every particle can be also considered as a wave). Therefore, visible light used for observations in optical microscope has wavelength of approximately $\lambda = 360 - 700$ nm. Such an optical system is also limited by diffraction, and thus it is possible to distinguish two points with distance between them of approximately $d \sim \lambda/2$. This fact, however, limits principally the optical microscopy to experience the maximal resolution of approximately 150 nm.

Therefore, by considering electron as the matter wave with the de Broglie wavelength

$$\lambda = \frac{h}{p} \quad (2.61)$$

where h is the Planck constant, and p is the momentum of a particles with mass m and speed v . Such an electron is accelerated in the SEM chamber by (high) voltage U . Kinetic energy of an electron can be expressed as

$$\frac{1}{2}m_e v^2 = eU. \quad (2.62)$$

When considering a typical accelerating voltage $U = 30$ keV, the speed of accelerated electron is obtained by expressing from the Equation (2.62) for v

$$v = \sqrt{\frac{2eU}{m_e}} \doteq 1 \cdot 10^8 \text{ ms}^{-1}. \quad (2.63)$$

The speed v obtained by these considerations can be now put into Equation (2.61)

$$\lambda = \frac{h}{p} = \frac{h}{m_e v} \doteq 0.0073 \text{ nm}. \quad (2.64)$$

This is of course a mere estimation, there are several negligences made during this deduction. The first one is that the speed $v \approx c/3$, is very close to the speed of light c . Therefore, normally it would be necessary to consider relativistic effects. However, when calculating for corrected electron wavelength, there is a negligible discrepancy in value for this case. The next approximation is made by omitting aberrations such as spherical, chromatic, diffraction, and astigmatism. All of these aberrations are making the final resolution limit worse. Nowadays, instruments come with systems designed to correct aberrations to some extent and order.

Despite of making several approximations and negligences, the effective resolution limit of SEM can be taken as < 1 nm, which is, compared to optical microscopy, still 150 times greater [39].

2.6. SCANNING ELECTRON MICROSCOPY (SEM)

Figure (2.19) shows schematically scanning electron microscope instrument with image acquisition and imaging accessories. The whole process from electron beam creation until SEM image can be illustratively divided into five steps that are important to mention.

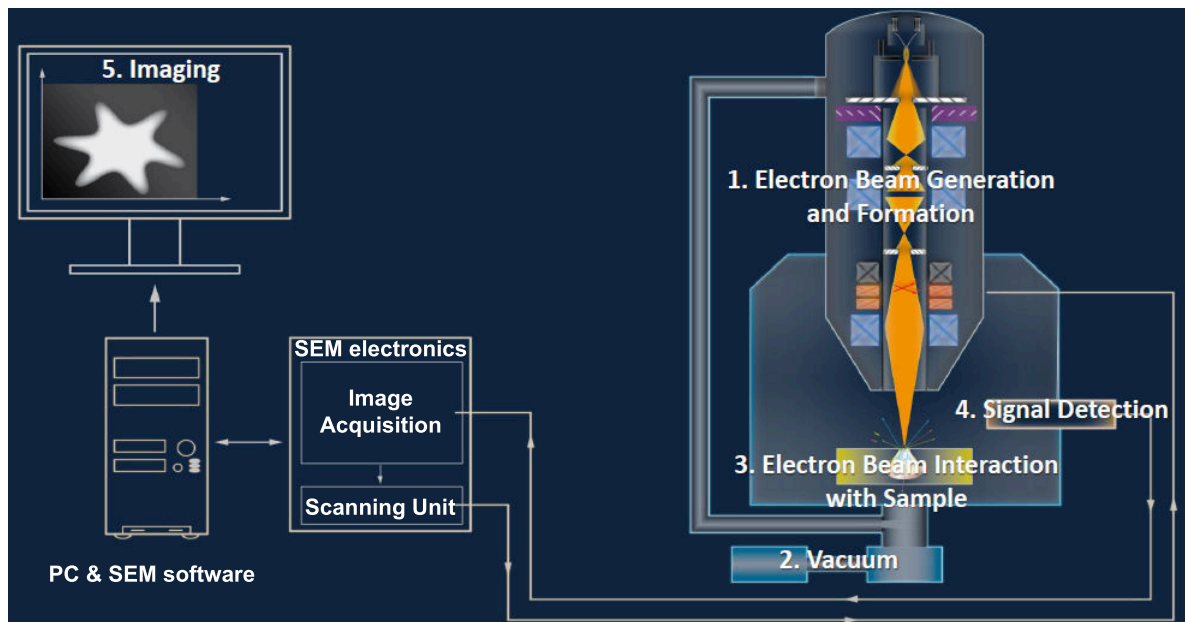


Figure 2.19: Scheme of SEM measurement unit. Adapted from [39]

The very first step is the formation of an electron beam, this is usually realised by ion source placed in a vacuum chamber. There are two main groups of sources: thermionic guns and field-emission guns. The first group is represented by the tungsten or LaB_6 filament. These sources have lifetime in hundreds of hours and often work in high vacuum regime ($p = 10^{-3} - 10^5$ Pa), and larger energy spread compared to the latter, field emission guns (e.g. Schottky gun). The advantage of field emission is lower energy spread and longer lifetime than thermionic guns. They also usually operate in the ultra high vacuum regime $p < 10^{-7}$ Pa. The vacuum serves to lower the probability of collision between the formed electron beam and particles inside the chamber [40].

The second interesting area is the interaction of accelerated electron beam with a specimen. The optical column serves to project the electron source onto a specimen. Both elastic and inelastic scattering occur when the beam hits the specimen. The final signal forming the image is the result of multiple scattering processes within the specimen. Exactly, by electron diffusion caused by the gradual loss of the kinetic energy and by lateral spreading caused by multiple elastic scattering. Therefore, electrons with different energies can be detected from various depths in the specimen. It is possible to detect contribution from secondary electrons (SE), backscattered electrons (BSE), Auger electrons (AE), and also x-ray. The most common detection is the secondary electrons (inelastically scattered from the emission of valence electrons), because these electrons can be extracted easily by positively biased collector grid placed on one side of the specimen due to their low exit energy of a few eV [41].

Finally, unlike optical microscope, where human eye is usually used as sufficient detector, in a SEM unit, the last task is to process the detected signal which is usually done by specialised image acquisition software with user interface from a particular company producing the SEM unit. To conclude, SEM is a reasonable characterisation method for examination of specimen's morphology.

2. THEORY

3. Experiment

This chapter provides a simple, step-by-step description of preparation and characterisation done during the work on this topic. It is important to note that the scope of the topic is multi-disciplinary and requires cooperation with several colleagues from various scientific areas. Therefore, as an author of this thesis, I will highlight and refer to work done in cooperation and give comments when necessary in order to understand why was it done this way.

I have decided to order this experimental section by compounds that were prepared and characterised herein. In total, five different compounds were subjected to investigation as graphene-based hybrid material. First and foremost, it was necessary to prepare and characterise reference samples (substrate, graphene, compounds) so that properties of consecutively prepared graphene-based hybrid material could be treated correctly. Hence, every compound and graphene is described as such, and afterwards, mixtures are presented.

The first compound was Copper(II)dibenzoylmethane - $\text{Cu}(\text{dbm})_2$ with chemical formula: $\text{C}_{30}\text{H}_{22}\text{CuO}_4$, which is a transition-metal complex with copper as a central atom surrounded by two dibenzoylmethane ligands. It is a potential quantum bit with rather long coherence time $t = 25 \mu\text{s}$, which is a time usable for quantum computations. After this time, the superposition of states $|0\rangle$ and $|1\rangle$ is interrupted by the environment, and thus is no longer suitable for performing quantum computations.

The second compound was N,N' -Bis(salicylidene)ethylenediaminonickel(II) - $\text{Ni}(\text{salen})$ with chemical formula: $\text{C}_{16}\text{H}_{16}\text{N}_2\text{NiO}_2$, which is a transition-metal complex with nickel bonded to two nearby oxygen atoms. This compound was investigated due to its square planar symmetry, which could change from diamagnetic to paramagnetic in the presence of graphene structure.

The third compound was [1,1 -Bis(diphenylphosphino)ferrocene]dibromocobalt(II) - $[\text{CoBr}_2(\text{dppf})]$ - DM15N with chemical formula: $\text{C}_{34}\text{H}_{28}\text{Br}_2\text{CoFeP}_2$, which is a cobalt ferrocene with two bromides bonded to the cobalt. This compound is a field induced single-molecule magnet.

The fourth compound was [1,1 -Bis(diphenylphosphino)ferrocene]dichlorocobalt(II) - $[\text{CoCl}_2(\text{dppf})]$ - DM18N with chemical formula: $\text{C}_{34}\text{H}_{28}\text{Cl}_2\text{CoFeP}_2$, which is a cobalt ferrocene with two chlorides bonded to the cobalt. This compound is, as well as DM15N, a field induced single-molecule magnet.

Finally, the last compound was - Tetrabutylammonium-bis(phthalocyanine)erbium - $[\text{ErPc}_2]^{-}(\text{TBA})^{+} \cdot 2\text{DMF}$ - ErPc_2 with chemical formula: $\text{C}_{86}\text{H}_{82}\text{ErN}_{19}\text{O}_2$, which is the erbium phthalocyanine double-decker with large g anisotropy. This compound is also a single-molecule magnet.

3.1. Preparation of Graphene-Based Hybrid Materials

This section presents a preparative method for graphene-based hybrid materials as a thin film. All samples were prepared by multiple modified Langmuir–Schaefer (LS) deposition. This method involved deposition of a graphene, in the form of a few-layer graphene (FLG), onto a Si/SiO₂ substrate. FLG can be imagined as several monolayers (10 – 20) of graphene stacked upon each other. The term LS deposition originates from classical Langmuir–Blodgett (LB) thin film deposition mentioned in Theory 2.3 section. There is, however, a difference in the direction of deposition process. Unlike LB deposition, which is done in the vertical manner, LS deposition is done horizontally. By the term modified, the use of elevated and tilted substrate is meant. In fact, the method can be imagined as a bathtub filled with a water containing impurities and dust. When the bathtub is drained, the impurities remain at the bottom of the bathtub. This is a fair analogy to what really happens during the deposition by this method.

Subsequently, different dissolved metal complexes were deposited onto a graphene-covered substrate in order to form a graphene-based hybrid material. There were totally two different, but similar in principle, Langmuir–Schaefer deposition set-ups used. The first one was solely used for the FLG deposition and the second one solely for the molecular deposition. All multiple modified LS depositions took place at the Department of Multilayers and Nanostructures, Slovak Academy of Sciences, Bratislava, Slovak Republic in cooperation with Dr. Dmytro Kostyuk and Dr. Peter Šiffalovič.

3.1.1. Few-Layer Graphene (FLG) – Deposition

Before the FLG deposition as such could be carried out, it was necessary to prepare a FLG suspension in advance. The FLG was prepared from expanded and milled graphite flakes that were subjected to a sonication followed by centrifugation and sedimentation. The expanded graphite can be obtained by introducing an intercalating medium (e.g. sulphuric or nitric acid) to the graphite and warming it up by the microwave irradiation [42], [43]. An analogy to a popcorn in a microwave oven can be applied. This expanded graphite is milled in order to reduce grain size. In the production of a graphene layer, steps towards miniaturisation of grains and separation of layers are made.

The expanded and milled graphite was sonicated for 60 minutes at the room temperature (25 °C) in an ultrasonic bath. The sonication helps to exfoliate graphite layers that tend to re-aggregate by the weak Van der Waals forces acting among them. Therefore, it is convenient to use a stabilisation agent as a sonication medium, which prevents the graphene layers from re-aggregation to graphite. In this case, *N*-Methyl-2-pyrrolidone (NMP) was used, because it minimises the interfacial tension between the graphene and the solvent, NMP itself in this case [20].

The prepared FLG suspension in NMP was centrifuged in order to separate supernatant from sediment. It was centrifuged at 10320 RPM for 30 minutes. Afterwards, supernatant was taken and left further to settle in a fridge ($T = 2 - 3^{\circ}\text{C}$) for a month. The final concentration of graphene in the suspension was 0.1 – 0.2 mg/mL with average size of nano-sheets: 300 nm and average thickness of nano-sheets 5 – 10 nm (i.e. 10 – 20 layers).

3.1. PREPARATION OF GRAPHENE-BASED HYBRID MATERIALS

Figure (3.1) shows experimental set-up for modified Langmuir–Schaefer deposition which started by injecting the FLG suspension onto a sub-phase (deionised water in this case) surface (1). The movable barriers (2) were slowly closed and reduced the surface area of a through top (1). The process of a layer formation was observed by optical microscope (3) with visual output (4) to a monitor. A Wilhelmy plate (5), usually a piece of filtration paper, was used to measure the surface pressure. (6) is the Si/SiO₂ substrate on which the FLG deposition took place. And finally, the suction pump (7), by which the water was sucked out, and thus the water level was lowered and the deposition was done. The term modified stands for the deposition carried out by elevating and titling the substrate. This was done by placing metal nuts of different sizes underneath the substrates.

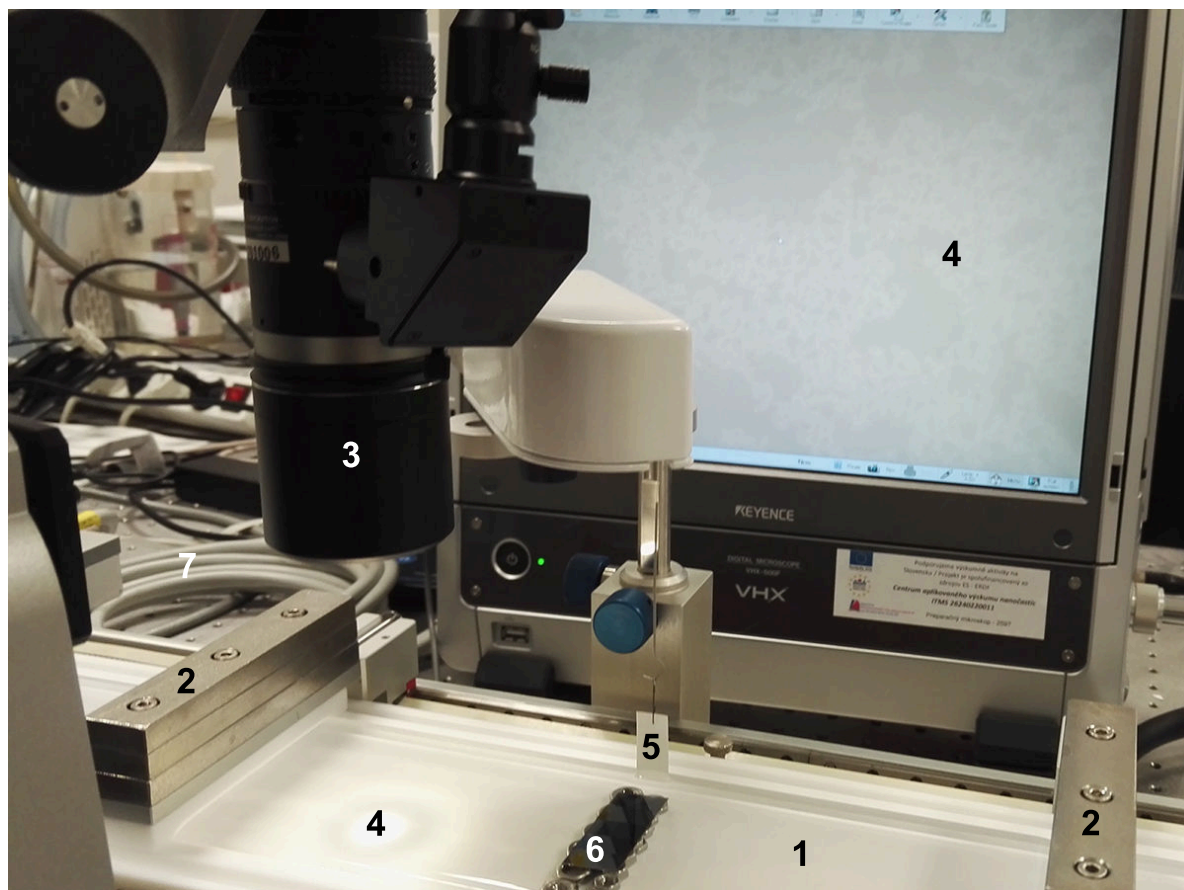


Figure 3.1: Image of Langmuir–Schaefer set-up for FLG deposition. Numbers indicate individual components of the whole so-called 'through'. (1) Through top with injected FLG suspension, (2) movable barriers, (3) optical microscope, (4) visual output, (5) surface pressure sensor, (6) Si/SiO₂ substrates for deposition, and (7) suction pump.

After the first FLG deposition was made, samples were annealed at 800 °C for 30 minutes. This step helped to get rid of the remaining water from the deposition and to stabilise layer on the substrate. Finally, Si/SiO₂ with a deposited FLG was prepared (graphene-covered substrate) by this first modified Langmuir–Schaefer deposition. The main advantage of this method is apparent, it is possible to use manifold of various substrates at the same time during the deposition.

3. EXPERIMENT

3.1.2. Molecular Deposition

The second, molecular, deposition was held right after the first FLG deposition was done. Firstly, it was necessary to dissolve metal complexes that were prepared in the form of crystals. Table (3.1) shows solubility of metal complexes in appropriate solvents: chloroform, CHCl_3 -(CL), dichloromethane, CH_2Cl_2 -(DCM), and dimethylformamide, $(\text{CH}_3)_2\text{NC}(\text{O})\text{H}$ -(DMF).

Table 3.1: Solubility of used metal complexes in organic solvents.

Molecule	$\text{Cu}(\text{dbm})_2$	$\text{Ni}(\text{salen})$	DM15N	DM18N	ErPc_2
Solvent	CL	DCM	DCM	DCM	DMF
Solubility	Moderate	High	High	High	High

Figure (3.2) shows experimental set-up for the second modified Langmuir–Schaefer deposition which started by injecting dissolved metal complexes onto a sub-phase (also deionised water) surface (1). The movable barriers (2) were slowly closed and reduced the surface area of a through top (1). A Wilhelmy plate (3), usually a piece of filtration paper, was also used to measure the surface pressure. (4) represents the graphene-covered Si/SiO_2 substrate from previous FLG deposition. And finally, the suction pump (5), by which the water was sucked out, and thus the water level was lowered and the deposition done. The term modified stands for the deposition carried out by elevating and titling the substrate by a flat metal washer placed under the graphene-covered substrate.

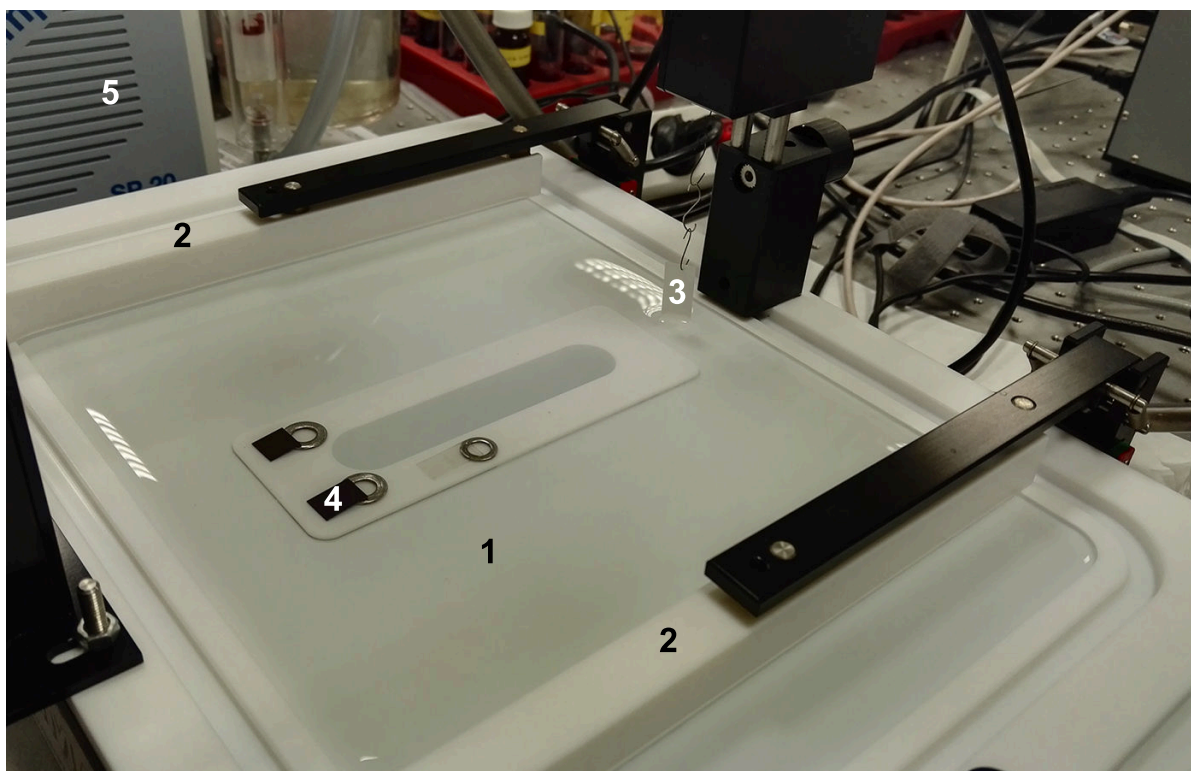


Figure 3.2: Image of Langmuir–Schaefer set-up for molecular deposition. Numbers indicate individual components of the whole so-called 'through'. (1) Through top with injected molecular complexes, (2) movable barriers, (3) surface pressure sensor, (4) graphene-covered Si/SiO_2 substrate, and (5) suction pump.

3.1. PREPARATION OF GRAPHENE-BASED HYBRID MATERIALS

Figures (3.3) and (3.4) illustrate the first step of second, molecular, deposition. The through top was filled with deionised water. Dissolved metal complexes were injected onto a water sub-phase until no further spreading was visible. Compounds formed an oil-like structure on the water/air interface, which was made visible by exploiting the reflection from a fluorescent lamp from the room ceiling. The movable barriers were closed to a certain surface pressure estimated by blank measurements (without substrates) for every compound. This will be discussed for each individual compound in the later characterisation section Isotherms 3.5.2. The total area A of the through for molecular deposition was 483.3 cm^2 , and the speed for closing the barriers $20.4\text{ cm}^2/\text{min}$ was the same for every molecular deposition.

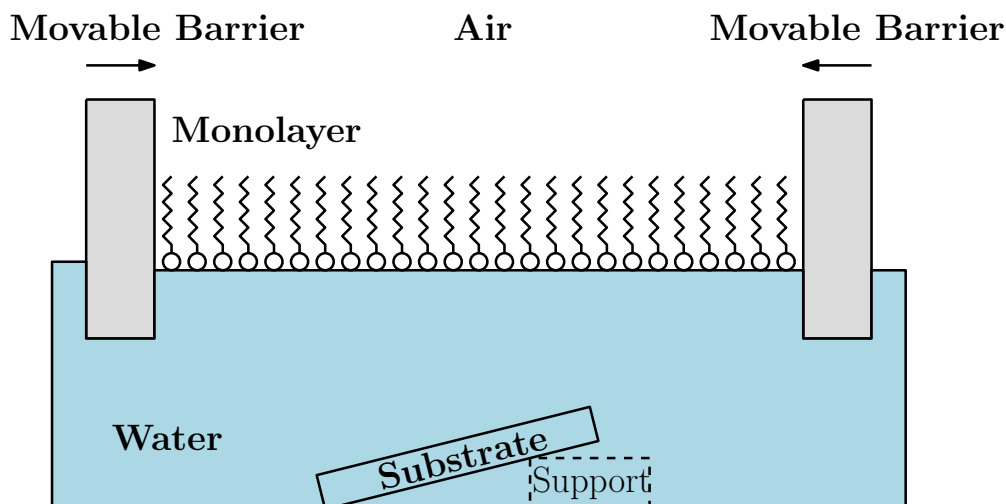


Figure 3.3: Schematic side view of molecular deposition. Graphene-covered substrate was elevated and tilted by a flat washer.

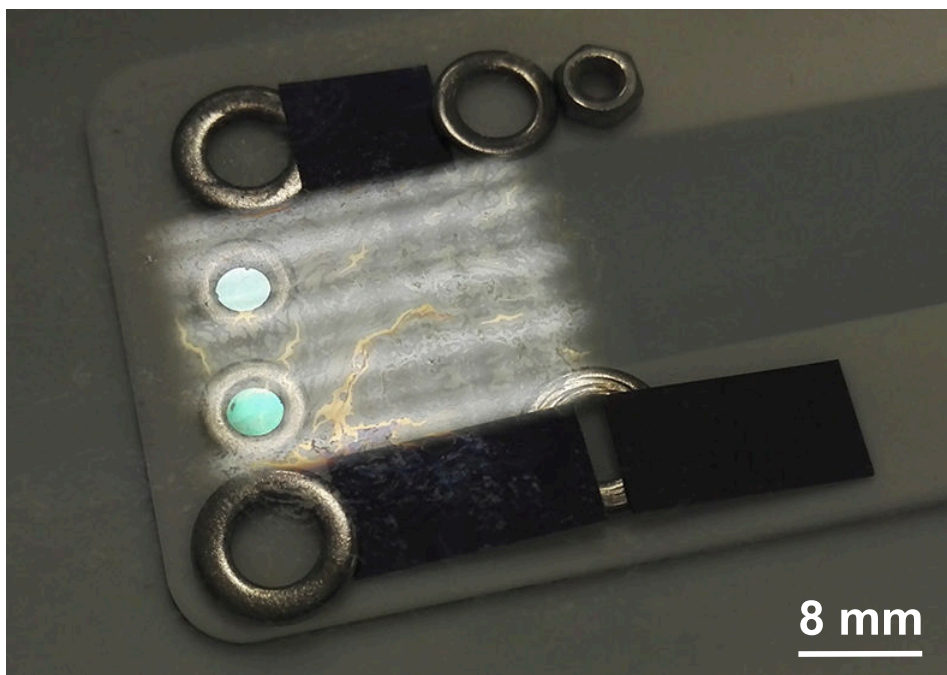


Figure 3.4: Image taken by a camera revealing the oil-like molecular layer on the water sub-phase.

3. EXPERIMENT

The following Figures (3.5) and (3.6) illustrate the second step of second, molecular, deposition. The closing of movable barriers was stopped. Subsequently, a suction pump was connected to the through and the water level was lowered. The compounds were deposited as the level reached the graphene-covered substrate.

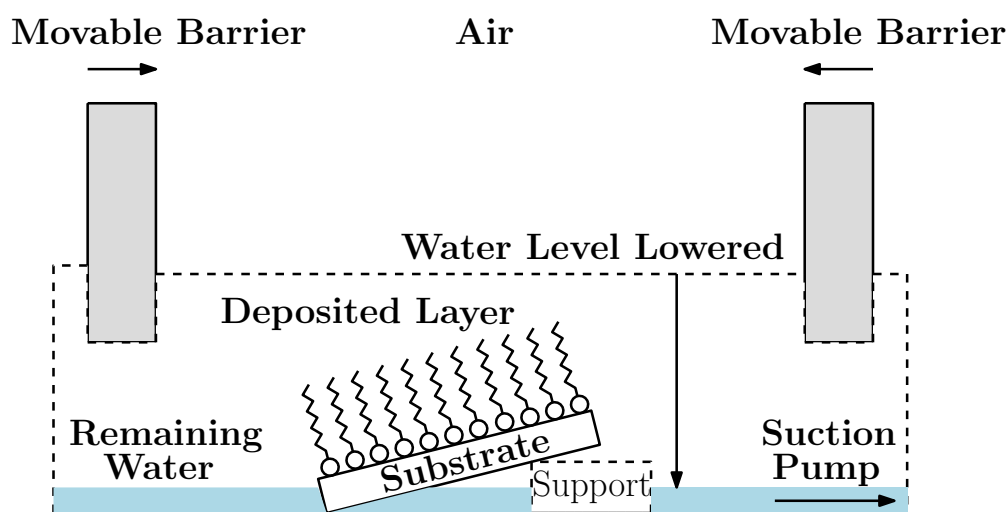


Figure 3.5: Schematic side view of the second step of molecular deposition. Graphene-covered substrate is covered by the molecular layer as the suction pump sucked out the through and the water level was lowered.



Figure 3.6: Image taken by a camera showing the deposited molecular layer on the graphene-covered substrate.

By this deposition, a solution with one type of compound can be deposited onto numerous different substrates with negligible interference among them. This multiple modified Langmuir–Schaefer deposition is scalable, reproducible, and presents a feasible deposition route for various metal complexes.

3.1. PREPARATION OF GRAPHENE-BASED HYBRID MATERIALS

Figure (3.7) illustrates the final product of deposition. The base of these multilayer samples is boron doped Si(100) substrate with the thickness of $500\ \mu\text{m}$. On top of this layer lies the SiO_2 with the thickness of $500\ \text{nm}$. The FLG layer deposited by the first modified Langmuir–Schaefer deposition was $5 - 10\ \text{nm}$ thick. The final layer is composed of different metal complexes deposited onto the graphene-covered substrate.

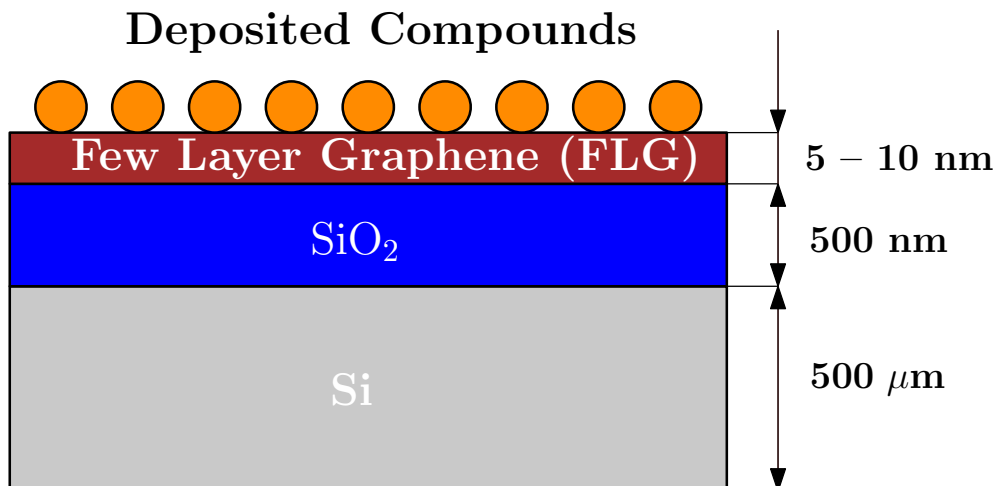


Figure 3.7: Scheme of the prepared graphene-based hybrid material.

Table 3.2: Summary of all prepared samples by the multiple modified Langmuir–Schaefer deposition. The first row indicates the substrate (layer in contact with compounds) used.

Molecule	Si/SiO ₂ (1)	FLG (2)	CVD (3)	MoS ₂ - S (4)	MoS ₂ - C (5)
Cu(dbm)₂	✓	✓	✓	-	-
Ni(salen)	✓	✓	✓	-	-
DM15N	✓	✓	✓	-	-
DM18N	✓	✓	✓	✓	✓
ErPc₂	✓	✓	✓	✓	✓

Table (3.2) summarises all samples prepared by the multiple modified Langmuir–Schaefer deposition. There were prepared reference samples consisting of bare Si/SiO₂ substrates + compounds (1). The next set of samples was graphene-covered substrates (2), that were mainly investigated. In addition, there were also additional molecular depositions made, such as onto a CVD-prepared graphene (3), and onto two transition metal dichalcogenides (4) and (5). The first one (4) MoS₂ - S was prepared at the Slovak Academy of Sciences, Bratislava. The second one (5) MoS₂ - C was commercially available. This MoS₂ material belongs to so-called '2D' materials along with graphene. They were, however, not particularly investigated in this project. The point of this list was to stress out the potential and applicability of this deposition method onto large variety of substrates. The depositions were done in cooperation at Slovak Academy of Sciences, Bratislava, Slovak Republic.

3. EXPERIMENT

3.2. Characterisation of Graphene-Based Hybrid Materials

The structure of characterisation section is as follows. First of all, resistance measurements carried out right after deposition are mentioned and high frequency electron paramagnetic set-up is introduced. Subsequently, characterisation of pristine few-layer graphene (FLG), as well as individual compounds on graphene-covered substrate, is presented.

3.3. Resistance Measurements

Figure (3.8) illustrates the resistance measurement. The voltage $U = 5\text{ V}$ was applied between (1) and (4) pins. Voltage was measured between (2) and (3) pins and by simple Ohm's law $R = \frac{U}{I}$ expressed as resistance R . To be strictly correct, electrical impedance Z was measured. Nevertheless, only real part $Re(Z)$ was considered. The distance between pins was 1 mm.

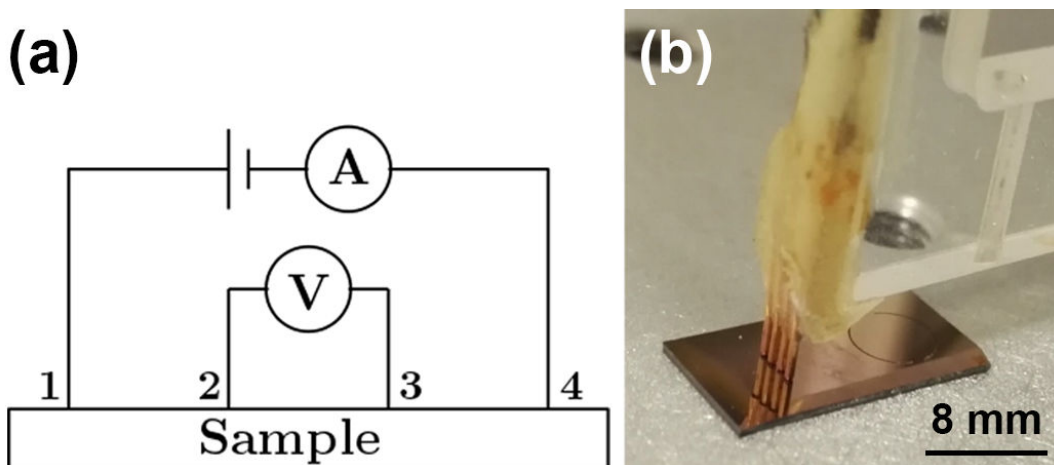


Figure 3.8: (a) Scheme of four-point probe set-up, (b) image of experimental set-up for four-point probe measurement.

Table 3.3: Resistance measurements on samples immediately after deposition.

	Reference	Cu(dbm) ₂	Ni(salen)	DM15N	DM18N	ErPc ₂
Substrate	50 GΩ	63 GΩ	60 GΩ	60 GΩ	65 GΩ	62 GΩ
FLG	65.4 kΩ	75 kΩ	33.5 kΩ	55 kΩ	131 kΩ	107 kΩ
CVD	584 Ω	1.46 kΩ	653 Ω	24 kΩ	19 kΩ	2 kΩ

Table (3.3) revealed that slightly worse resistance (i.e. improved conductance) was for Ni(salen) on FLG and DM15N on FLG. These results, however, have to be taken critically and further investigation with more sensitive techniques is necessary in order to confirm these results.

3.3.1. High Frequency EPR Spectrometer

The basics of HFEPR originate from the standard EPR spectrometer mentioned in Theoretical section 2.4.4. There are, however, several adjustments and differences between these two instruments. In the following section, a scheme of particular HFEPR instrument, at which HFEPR measurements took place is presented.

Figure (3.9) illustrates the main set-up components of HFEPR spectrometer located at the University of Stuttgart, Germany. The tunable microwave source (1) provides a radiation of frequency: $\nu = 82 - 1100$ GHz, which is propagated by a quasi-optics (2). The higher frequencies are accessible by amplifying and multiplying the microwave base frequency: $\nu = 8 - 12$ GHz. The variable temperature insert (3), $T = 1.8 - 300$ K, is put in a tunable superconducting magnet (4) capable of magnetic field up to ± 17 T. The microwave detection is provided by a InSb bolometer (5) cooled by the liquid nitrogen and helium in order to increase its sensitivity.

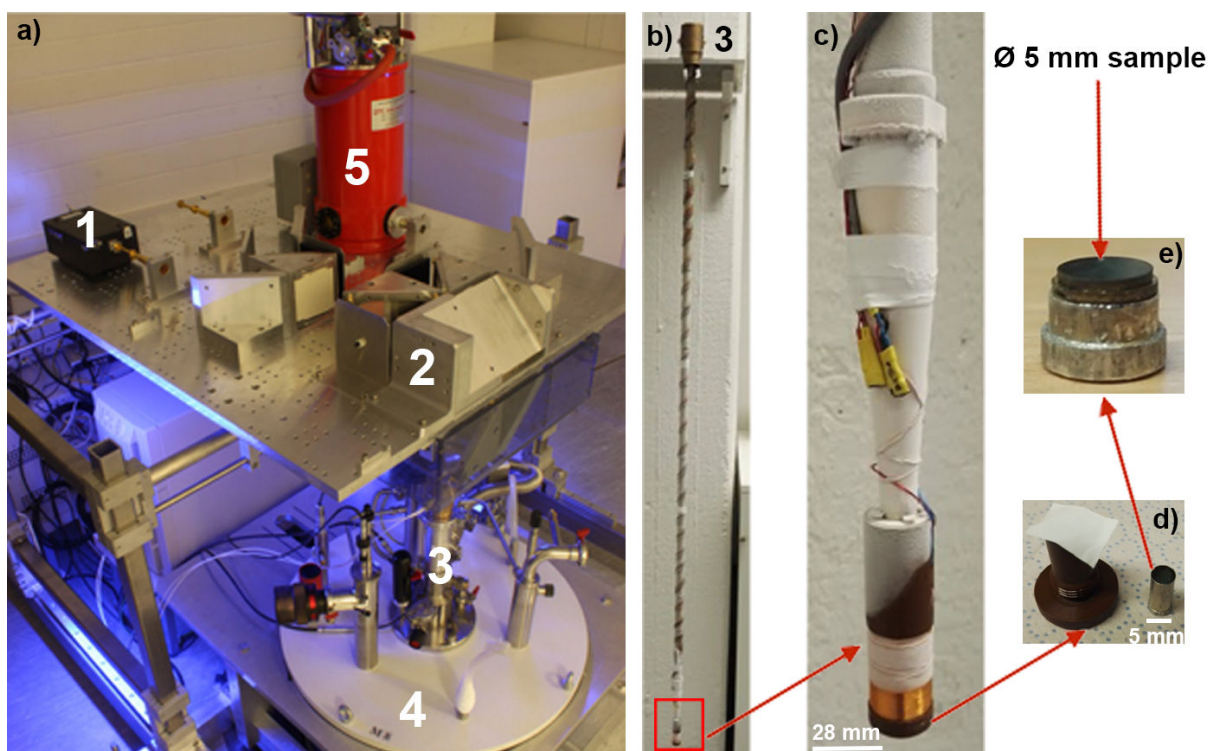


Figure 3.9: The HFEPR spectrometer in Stuttgart. (a) Indication of set-up components, (b) variable temperature insert (VTI), (c) detail of sample-rod head with modulation coil, at which the alternating current (AC) with known noise frequency is applied and form so-called 'lock-in' amplification of signal (first derivative of absorption signal is detected), (d) sample insert with support, and (e) $\varnothing 5$ mm sample in the form of a pressed pellet (for a bulk measurements) or thin film (deposited compounds on graphene-covered substrate).

3. EXPERIMENT

Figure (3.10) illustrates the mechanism of wave propagation through a quasi-optical table. The starting microwave-source path (green) is reflected by elliptical mirror and split into a Faraday rotator and back to the power monitor. The microwave passes through the Faraday rotator and wire polariser before it is transmitted through a corrugated wave-guide to the sample. The sample cavity is placed inside a superconducting magnet and modulation coil. The AC field modulation enables to lower the signal-to-noise ratio and to detect very weak signals. This is the basics of 'lock-in' technique used widely in spectroscopic instruments. This is also a reason, why the first derivative of absorption signal is observed by EPR measurements. To conclude, this particular HFEPR set-up enables advanced spectroscopy for a variety of samples by tuning the microwave, magnetic field, and temperature.

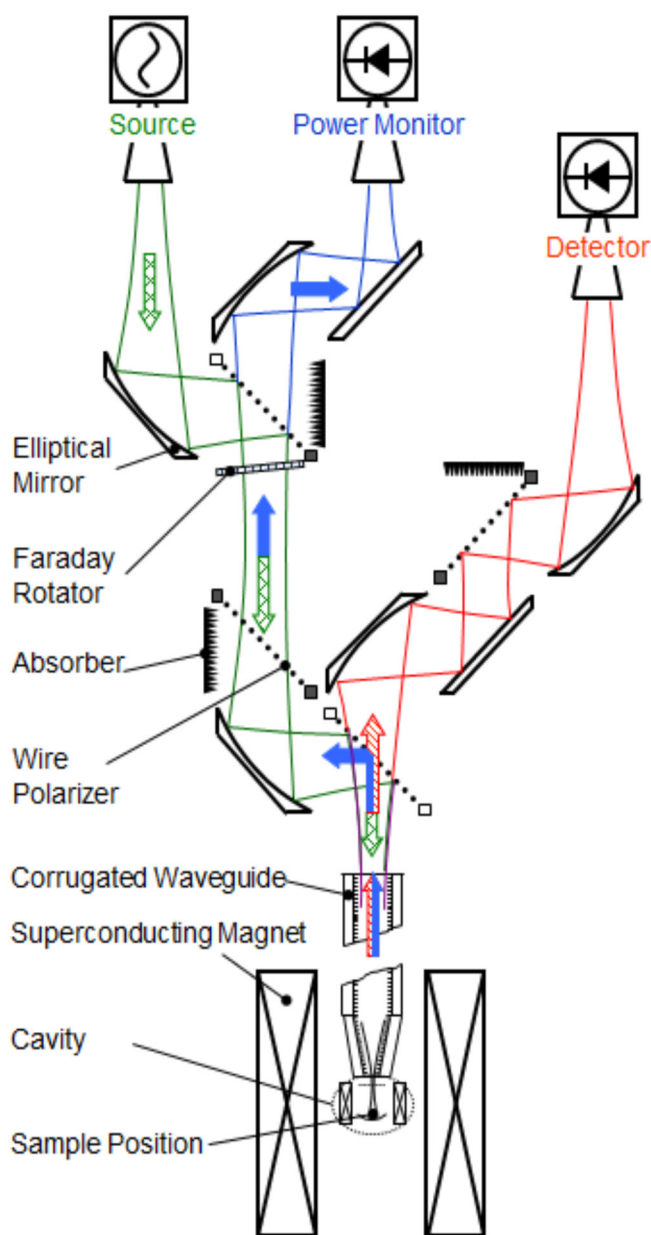


Figure 3.10: Scheme of HFEPR instrument located at University of Stuttgart, Germany. With permission of Dr. Petr Neugebauer.

3.4. Few-Layer Graphene (FLG)

First and foremost, it was necessary to characterise the FLG as such, because it served as the interface for the graphene-based hybrid material between the Si/SiO₂ substrate and deposited compounds.

3.4.1. Raman Spectroscopy

Figure (3.11) shows the measured Raman spectrum for FLG on Si/SiO₂ substrate in the region of graphene bands. In total, three peaks were observed, the so-called *G* band appeared at 1591 cm⁻¹ and the *G'* band at 2711 cm⁻¹. In the case of FLG, as it can be considered as a disordered graphene sample, the *D* band, which is approximately at half of the frequency of *G'* band, appeared. This is so-called disorder-induced *D* band.

The *G* band corresponds to doubly degenerate (iTO and LO) phonon mode at the Brillouin zone centre. The *G*-band is the only band coming from a normal first order Raman scattering process in graphene. On the contrary, the *G'* and *D* bands originate from a second-order process involving two iTO phonons near the *K* point for the *G'* band or on iTO phonon and one defect in the case of the *D*-band [44]. To sum up, FLG can be treated as a system with induced defect. Therefore, *D* band is observable and the intensity is higher. For instance, CVD grown graphene has only two major visible peaks: *G* at around 1600 cm⁻¹, and *G'* band at around 2700 cm⁻¹.

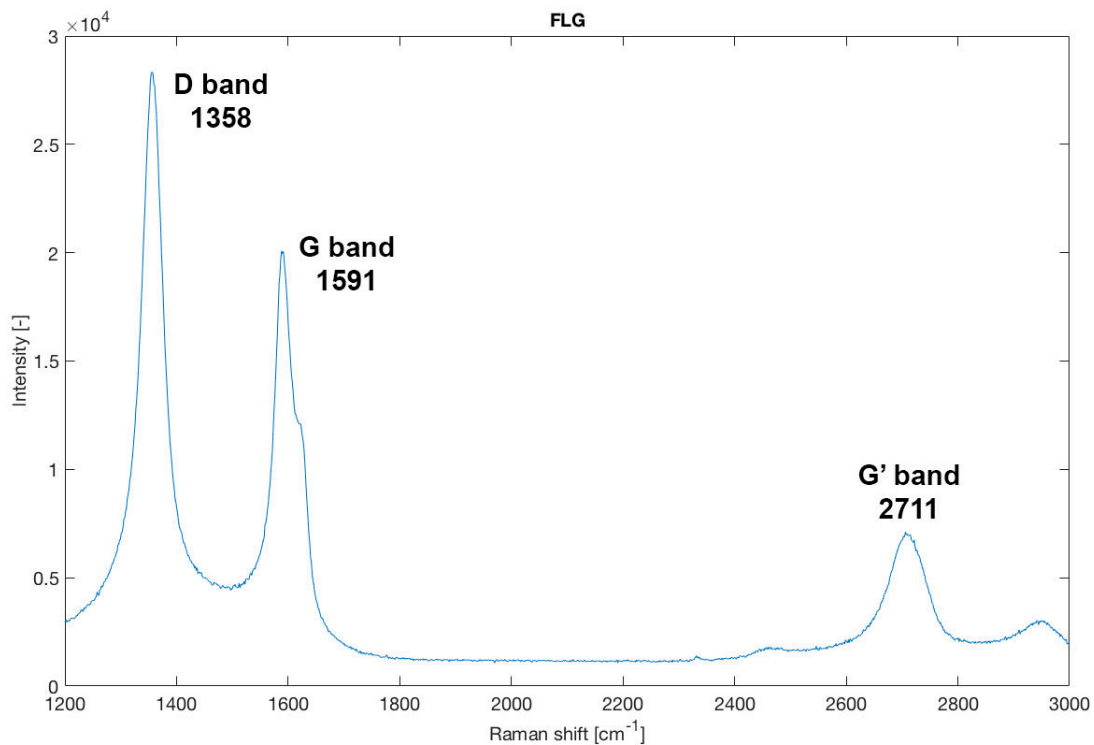


Figure 3.11: Raman spectrum of FLG. Excitation wavelength was 532 nm. Spectrum was acquired at MUNI in Brno, Czech Republic.

3. EXPERIMENT

3.4.2. High Frequency EPR

Figures (3.12) and (3.13) represent HFEPR spectra for graphene-covered substrate. The FLG spectra exhibited $g \approx 2.005 \approx g_e$. The substrate for FLG was boron doped p-type (100) Si/SiO₂ substrate with resistivity $\rho = 10 - 20 \Omega\text{-cm}$. The conductivity is inverse resistivity, giving the $\sigma = (0.05 - 0.1) \text{ S/cm}$. It was chosen in order to reduce influence around $g \approx g_e$ spectra. Nevertheless, it is generally difficult to treat spectra exhibiting values close to g_e as they might represent impurities or substrate.

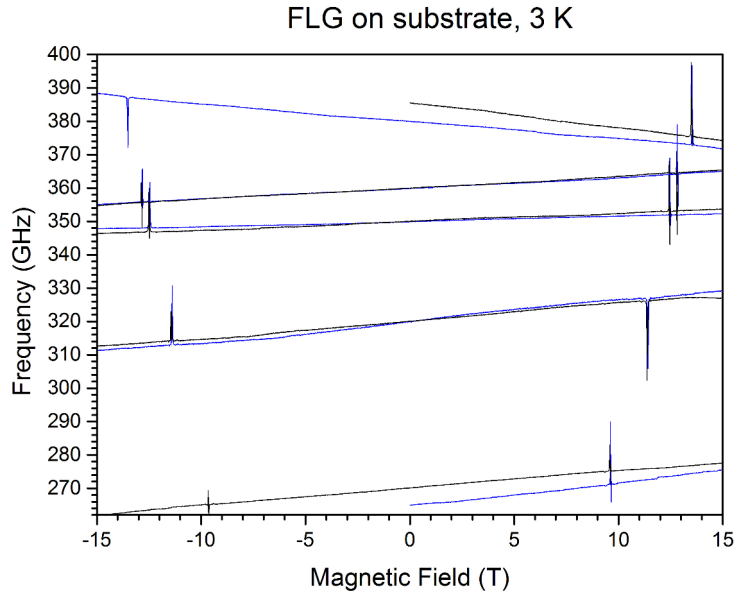


Figure 3.12: HFEPR spectra of FLG on Si/SiO₂ substrate for four frequencies at $T = 3 \text{ K}$.

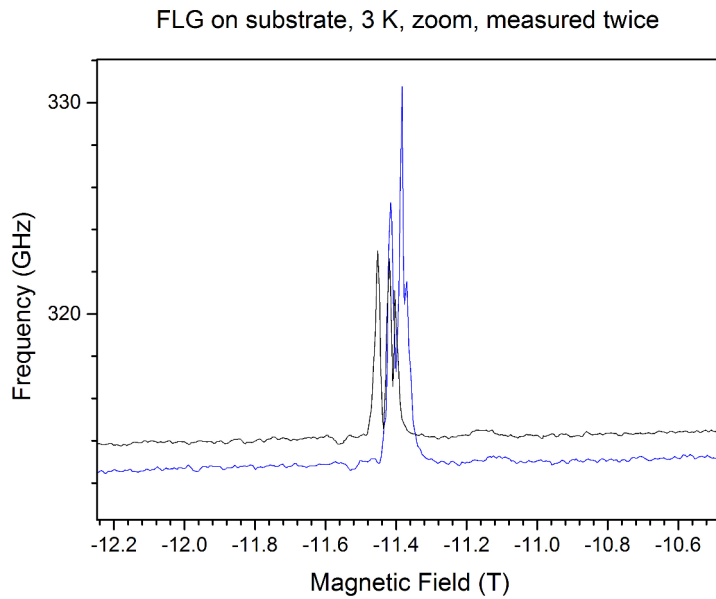


Figure 3.13: Detail of HFEPR spectra of FLG on Si/SiO₂ substrate for $\nu = 320 \text{ GHz}$ at $T = 3 \text{ K}$.

3.4.3. Scanning Electron Microscopy

Figure (3.14) shows a wrinkled, cloud-like structure of FLG deposited on Si/SiO₂. This few-layer formation of graphene was prioritised to, for instance, CVD graphene because of its morphology, which could provide better adhesion of compounds than strictly single-layer graphene.

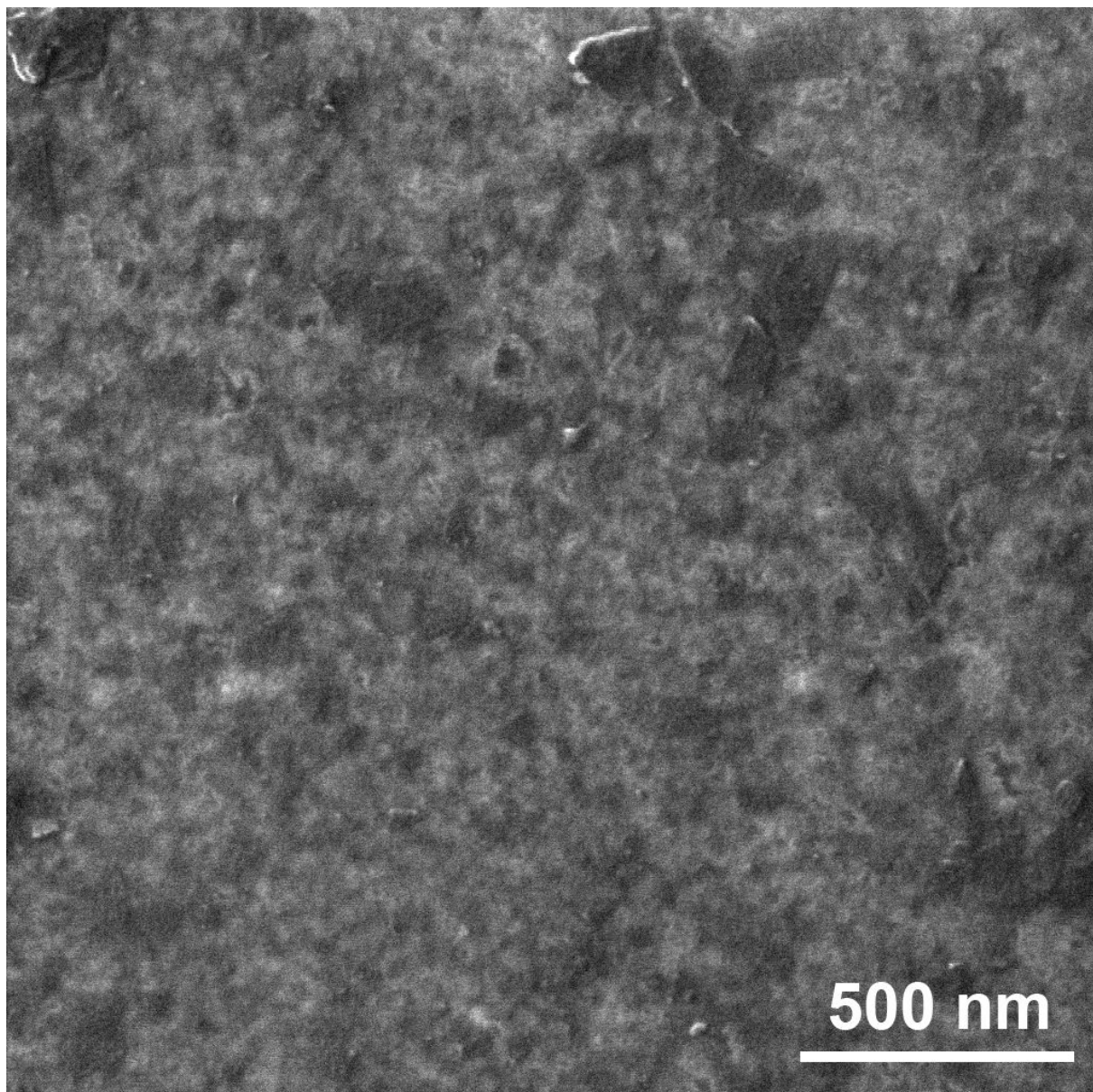


Figure 3.14: SEM image of FLG on Si/SiO₂. Voltage used: 30 kV. Detector: secondary electrons. Image was acquired at CEITEC - BUT, Czech Republic.

3. EXPERIMENT

3.5. Cu(dbm)₂

3.5.1. Synthesis and Structure

The first investigated compound was Cu(dbm)₂. The synthesis of this copper complex was described in several sources such as [45], [46]. The following synthetic route was chosen in order to prepare this compound. Copper(II) chloride dihydrate (1 mmol, 170 mg) was dissolved in water (15 mL) (Figure 3.15a–left beaker). Simultaneously, a solution of dibenzoylmethane (2 mmol, 458 mg) and potassium hydroxide (1.4 mmol, 80 mg) in ethanol/water mixture with 15:1 ratio (Figure 3.15a–right beaker) was added drop-wise to the copper solution. The resultant solution was stirred by a magnetic stirrer for 30 min. Afterwards, the precipitate was separated by a paper filtration and washed once by pure ethanol and demineralised water with consecutive vacuum filtration for 12 h. The yield of this synthesis was 347 mg.

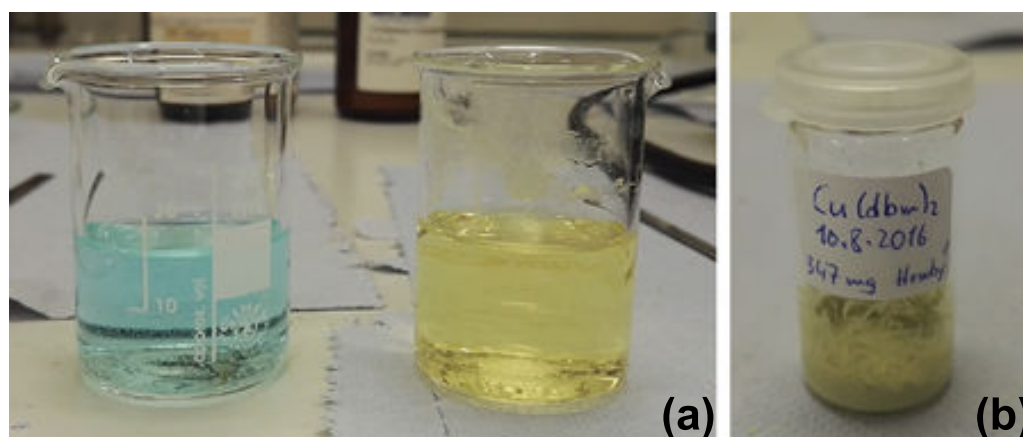


Figure 3.15: Synthesis of Cu(dbm)₂ compound. (a) The left beaker represents the solution with copper chloride and the right represents the solution with potassium hydroxide, (b) the final appearance of prepared Cu(dbm)₂ in the form of a green-coloured crystals.

Table 3.4: Precursors used for the synthesis of Cu(dbm)₂

Reagent	Molar mass [$\frac{\text{g}}{\text{mol}}$]	Amount of substance [mmol]	Mass [mg]
CuCl₂·2H₂O	170.48	1	170
KOH	56.11	1.4	80
Dibenzoylmethane	229.25	2	458

The following Table (3.5) shows results of elemental analysis for calculated and measured values of C and H atom. There is also a comparison with reference values mentioned. The final substance was in a fair agreement with reference and calculated and confirming that the synthesis was successful. The synthesis and elemental analysis were done at the University of Stuttgart, Germany.

Table 3.5: Elemental analysis for Cu(dbm)₂. *Calculated molar mass for C₃₀H₂₂CuO₄.

Element	Calculated*	Measured	Reference [45]	Reference [46]
C	70.65	71.73	70.37	70.60
H	4.35	4.58	3.98	4.33

Figure (3.16) shows a structure of prepared Cu(dbm)₂. The Cu(II) is surrounded by two dibenzoylmethane ligands.

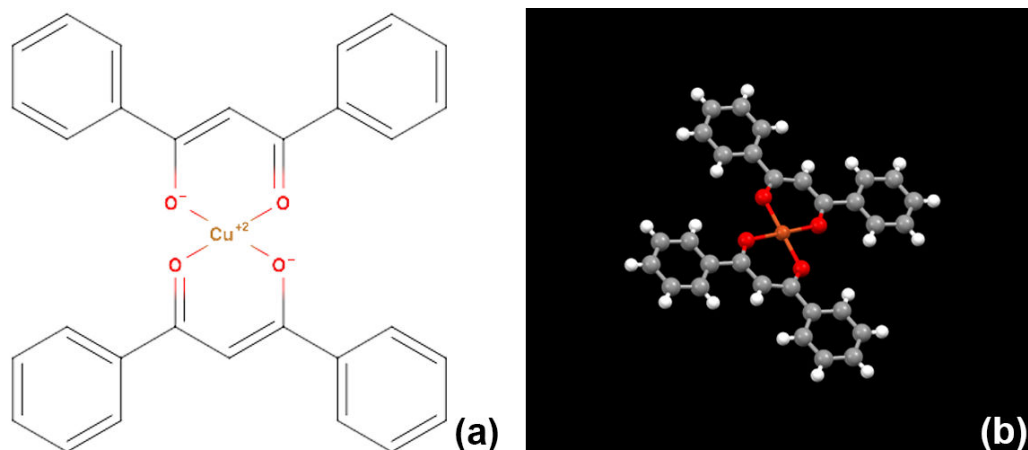


Figure 3.16: Illustration of Cu(dbm)₂ compound. (a) 2D sketch of chemical structure, (b) 3D view on the compound with measured distance $d = 13.6 \text{ \AA}$ between two furthest lying carbon atoms.

3.5.2. Isotherms

Figures (3.17) and (3.18) show isotherms (a curve on a pV diagram at the constant temperature) for Cu(dbm)₂ compound obtained during the blank deposition and actual deposition onto substrates, respectively. The graph was obtained by plotting the surface pressure Π , measured by Wilhelmy plate, against the area per molecule a , which was derived from equation mentioned in Theoretical section 2.40, giving the final expression as follows

$$a = \frac{AN_A}{cV} \quad (3.1)$$

where A is the actual through top area, N_A is Avogadro constant, c is the molar concentration of the solution, and V is the volume injected onto a water sub-phase. The molar concentration for both 'Finding' and 'Deposition' of Cu(dbm)₂ was 5 mM ($M = \text{mol/L}$). The volume $V_{\text{FINDING}} = 750 \text{ \mu L}$ and $V_{\text{DEPOSITION}} = 1400 \text{ \mu L}$. The isotherm is a very first characteristic of the compound regarding the deposition step. During the 'Finding' deposition, the isotherm was estimated to be at $\Pi = 25 \text{ mN/m}$ (i.e. where the curve starts to saturate). This pressure was then applied during the deposition onto substrates.

The process of finding a correct isotherm is crucial for formation of the ideal monolayer. This was, however, an uneasy task for metal compounds. Firstly, the monolayer was usually visible only as an oil-like structure on the water/air interface. Secondly, the injecting took place until no rapid spreading of compounds on the water surface occurred. Thirdly, it was necessary to consider energetic and geometric size of a compound for an ideal alignment on the water surface. To sum up, determination of an ideal concentration of solution, volume, and application of pressure has a high priority when depositing from a liquid-phase. Incorrect estimation can lead to formation of aggregates that are caused by insufficient area per molecule a left for the compound on the surface during the monolayer formation. Therefore, a simple rule can be applied when treating the nano-scale: "Less is more".

3. EXPERIMENT

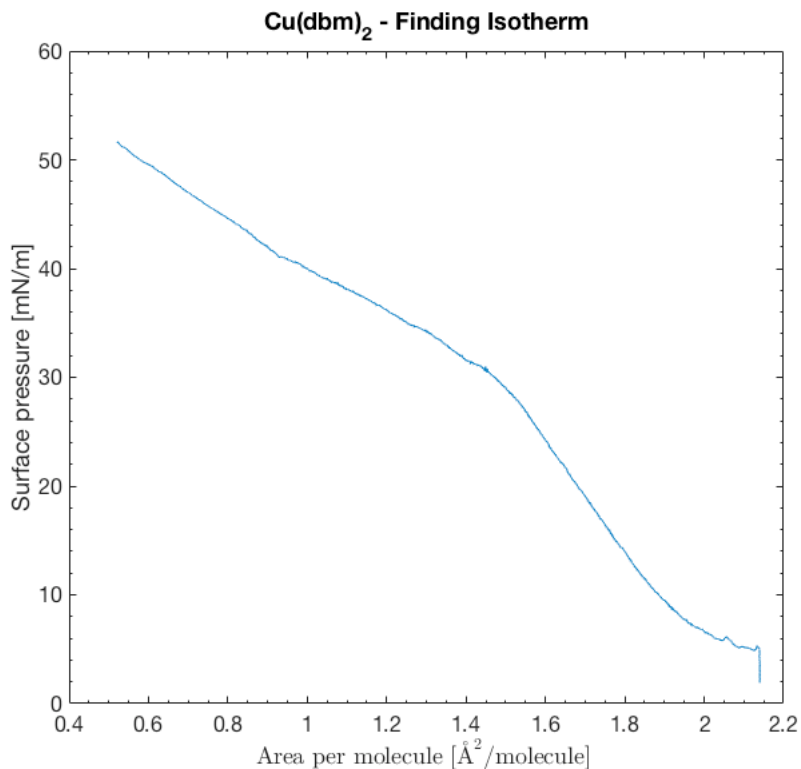


Figure 3.17: Graph of 'Finding' an isotherm for Cu(dbm)₂ compound. This was done by measuring the surface pressure Π versus area per molecule a for a blank deposition (i.e. without substrates).

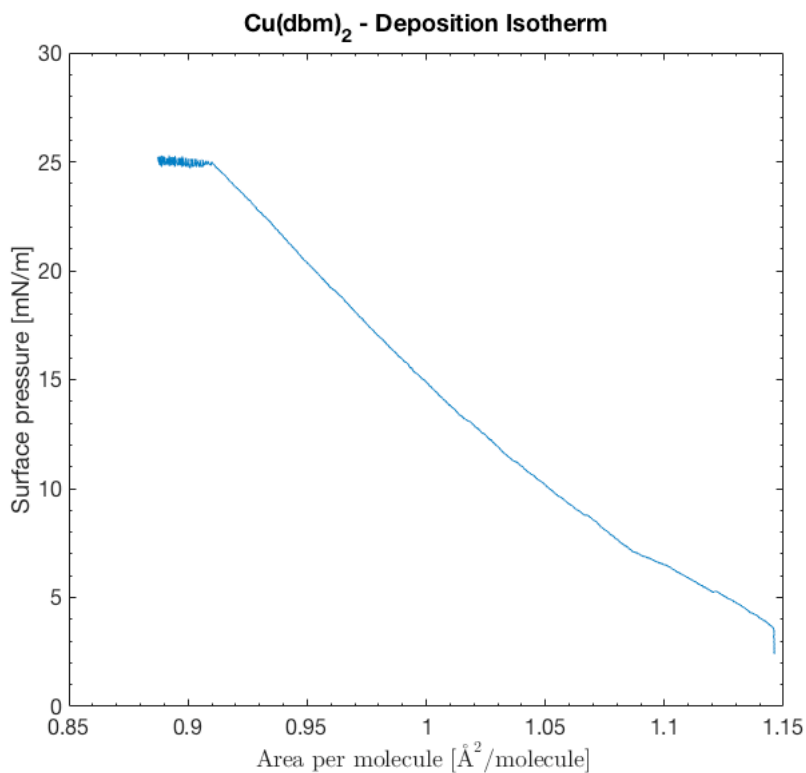


Figure 3.18: Graph of 'Deposition' isotherm for Cu(dbm)₂ compound. The surface pressure $\Pi = 25$ mN/m was applied for the deposition.

3.5.3. Raman Spectroscopy

Figure (3.19) shows Raman spectrum for powder Cu(dbm)₂. Peaks found are in accordance with another observation [47].

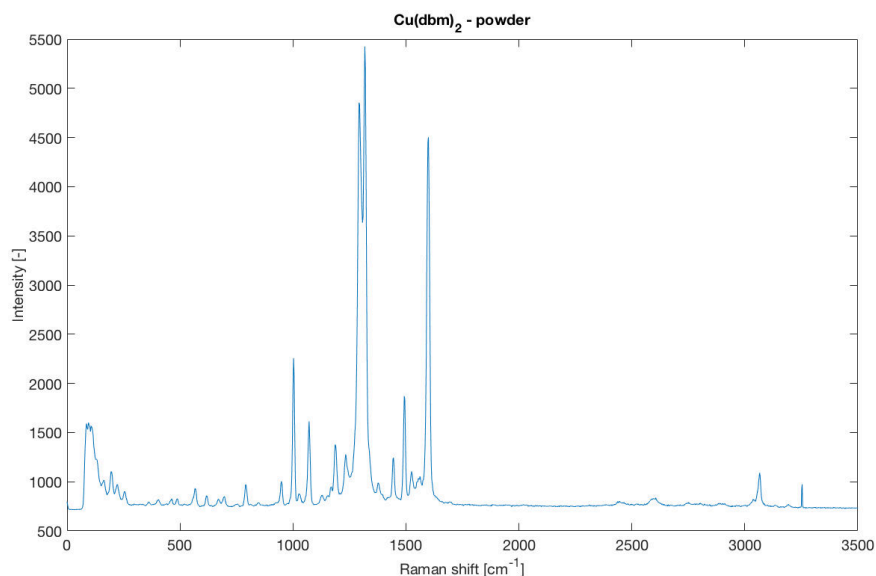


Figure 3.19: Raman spectrum for powder Cu(dbm)₂. Excitation wavelength was 532 nm. Spectrum was acquired at SAS in Bratislava, Slovak Republic.

Figure (3.20) shows spectrum for deposited thin film. There are three contributions to overall spectrum: Si/SiO₂ substrate (2.18), FLG (3.11), and powder spectrum (3.19). Cu(dbm)₂ peaks are nicely visible after deposition because of bigger aggregates formed on the substrate.

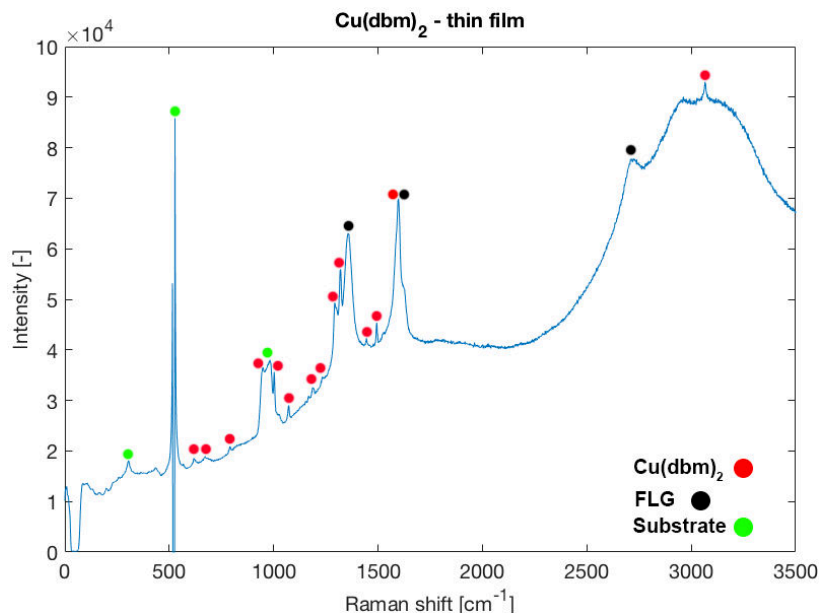


Figure 3.20: Raman spectrum for Cu(dbm)₂ deposited on the graphene-covered substrate. Excitation wavelength was 532 nm. Spectrum was acquired at MUNI in Brno, Czech Republic.

3. EXPERIMENT

3.5.4. High Frequency EPR

First and foremost, reference bulk pellet (i.e. all magnetic moment orientations) was measured at high frequency electron parameter resonance (HFEPR) set-up. This reference step was applied for every compound. The process of determination zero-field splitting parameters D , E , and g -value components was following:

- 1) Estimate of parameters was obtained by *ab initio* simulations.
- 2) HFEPR spectra were measured experimentally.
- 3) HFEPR spectra were fit according to measurements by calculations performed by EasySpin, a toolbox for MATLAB, and compared with simulated values.

Figure (3.21) shows measured HFEPR spectra of bulk $\text{Cu}(\text{dbm})_2$. In this case, hyperfine-tensor A components were determined.

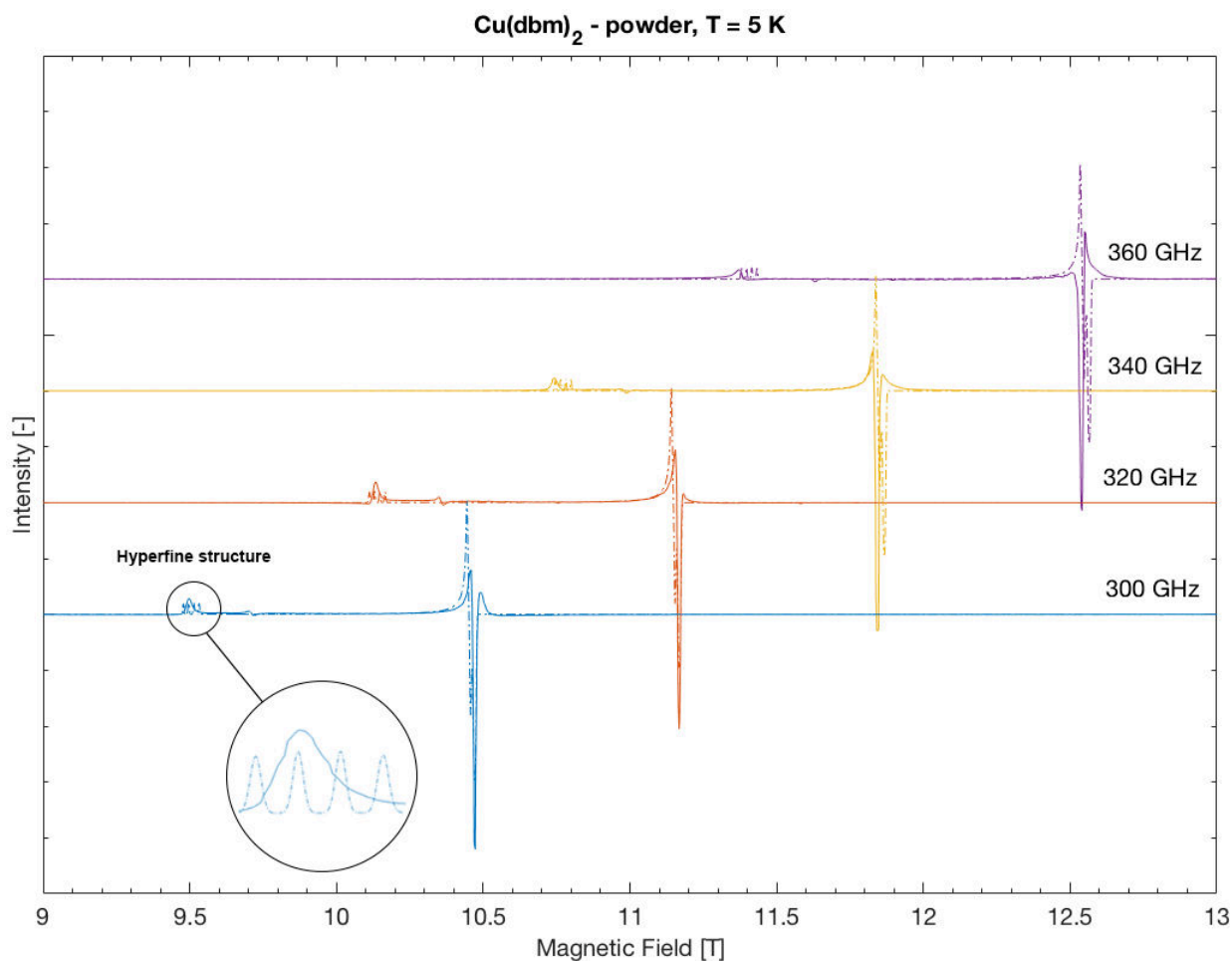


Figure 3.21: HFEPR spectra of $\text{Cu}(\text{dbm})_2$ for four frequencies $T = 5$ K. Full lines represent measured data, dashed lines represent fit. With permission of Ing. Michal Kern.

Table 3.6: Parameters for two-system spectrum of $\text{Cu}(\text{dbm})_2$ on FLG showed by following Figures (3.22) and (3.23).

Parameters	Spin	A_x [MHz]	A_y [MHz]	A_z [MHz]	g_x	g_y	g_z
$\text{Cu}(\text{dbm})_2$	1/2	76.4	84.7	550	2.047	2.051	2.255
FLG	1/2	-	-	-	2.005	2.005	2.005

Figures (3.22) and (3.23) illustrate $\text{Cu}(\text{dbm})_2$ on graphene-covered substrate.

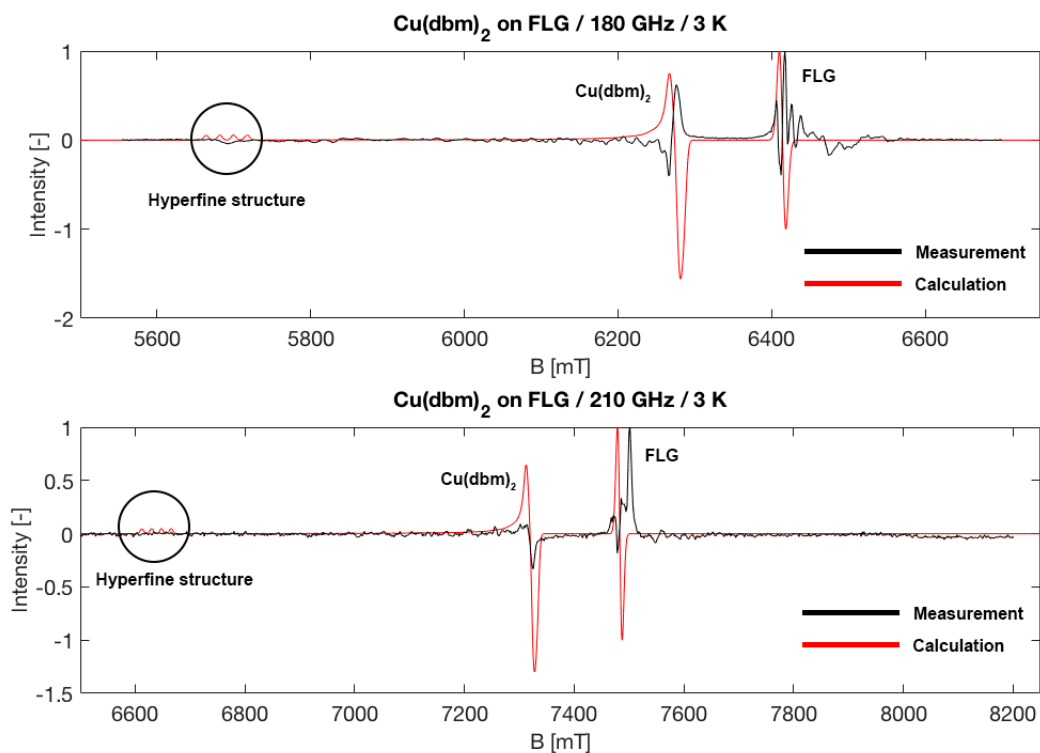


Figure 3.22: HFEPR spectra of $\text{Cu}(\text{dbm})_2$ for $\nu = 180$ GHz and $\nu = 210$ GHz at $T = 3$ K.

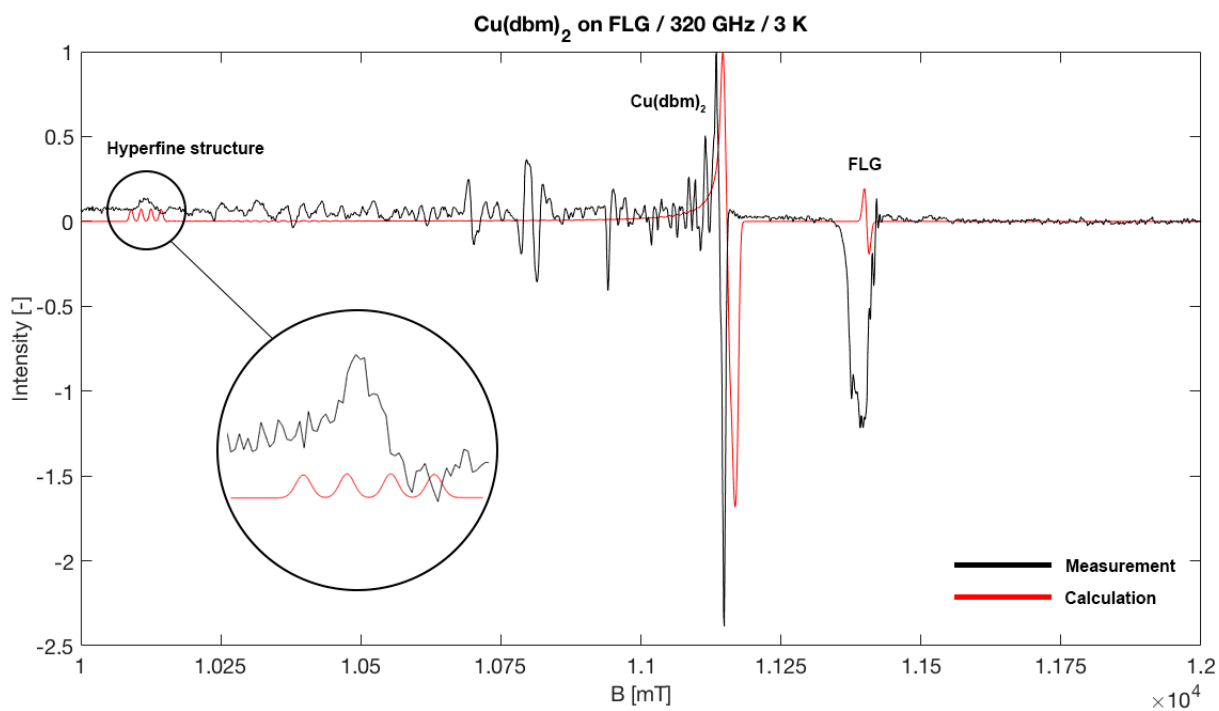


Figure 3.23: Detail of HFEPR spectrum of $\text{Cu}(\text{dbm})_2$ for $\nu = 320$ GHz at $T = 3$ K.

3. EXPERIMENT

3.5.5. Scanning Electron Microscopy

Figure (3.24) shows SEM image of deposited $\text{Cu}(\text{dbm})_2$ on the graphene-covered substrate. This compound is moderately soluble in chloroform, which lead to formation of bigger aggregates. One of them was observed in this SEM image. Molar concentration of solution was $c = 5 \text{ mM}$. Approximate size of formed crystals was $0.5 - 5 \mu\text{m}$. The grey structure behind corresponds to FLG and black background to the Si/SiO_2 substrate.

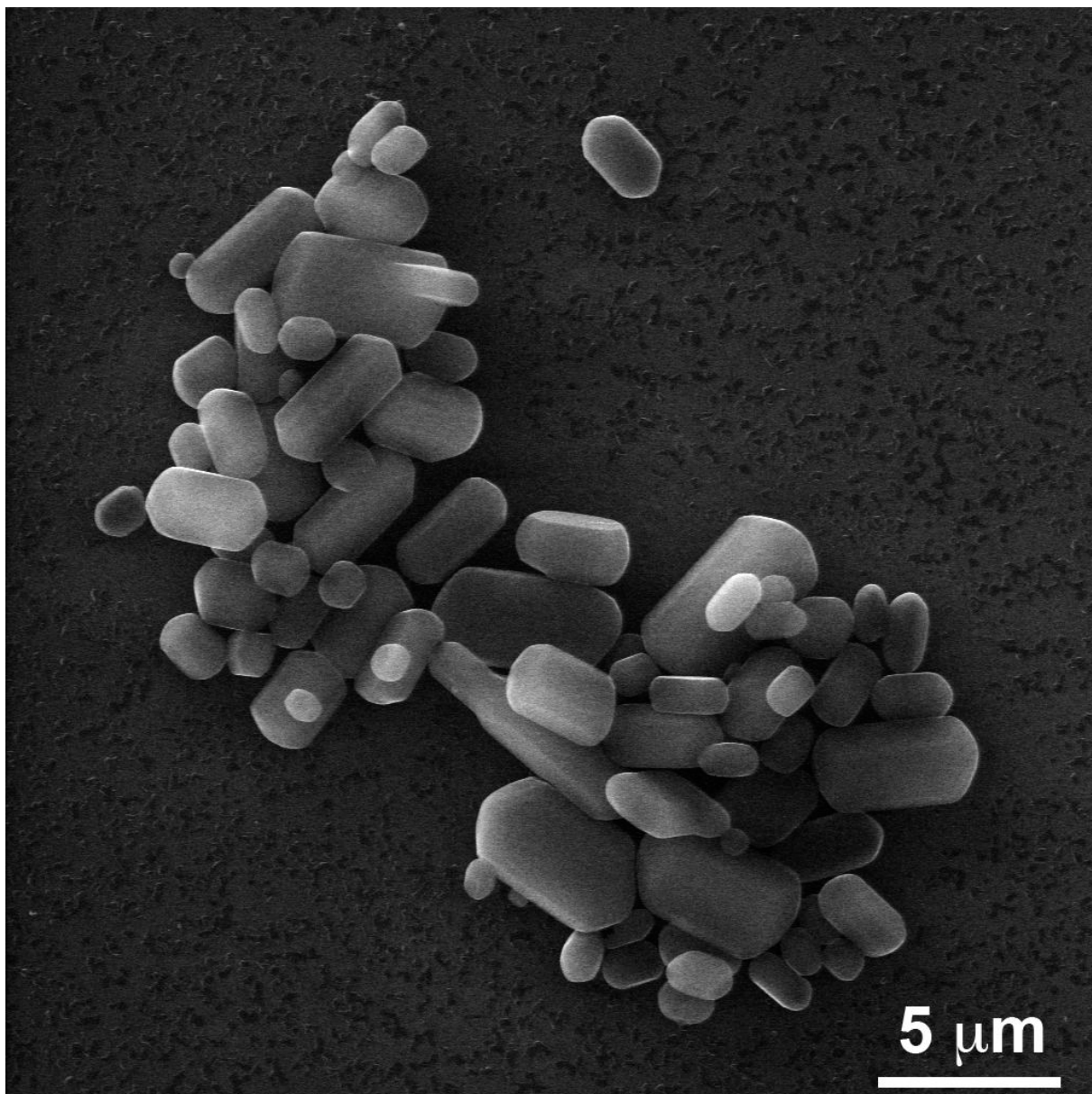


Figure 3.24: SEM image of $\text{Cu}(\text{dbm})_2$ on the graphene-covered substrate. Voltage used: 30 kV. Detector: secondary electrons. Image was acquired at CEITEC - BUT, Czech Republic.

3.6. Ni(salen)

3.6.1. Synthesis and Structure

The second investigated compound was Ni(salen). The compound was synthesised at Palacký University Olomouc, Czech Republic. The synthetic route was according to [48]. This complex was investigated due to its square planar geometry. Our presumption was, that it could change its arrangement in the vicinity of the nickel centre due to the non-covalent/semi-covalent contact with graphene resulting in change of its magnetic state from diamagnetic to paramagnetic.

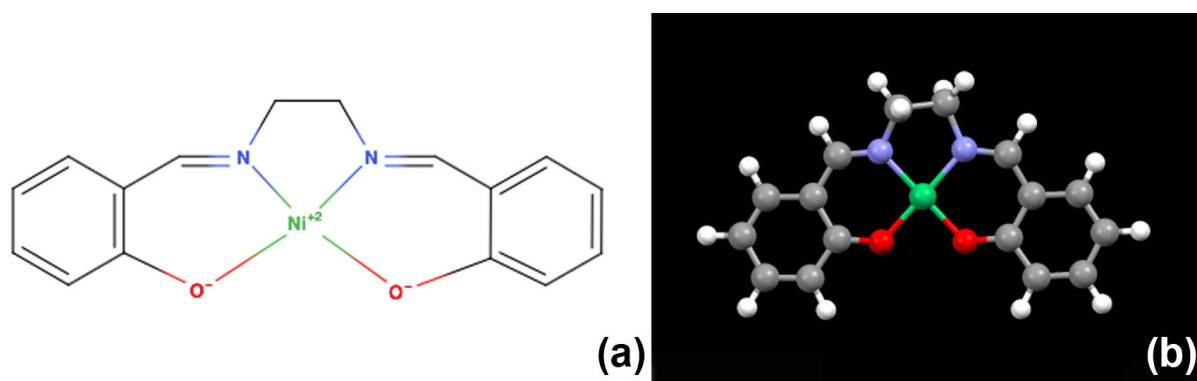


Figure 3.25: Illustration of Ni(salen) compound. (a) 2D sketch of chemical structure, (b) 3D view on the compound with measured distance $d = 10.8 \text{ \AA}$ between two furthest lying carbon atoms.

3.6.2. Isotherms

Figures (3.26) and (3.27) show isotherms for Ni(salen) compound obtained during the blank deposition and actual deposition onto substrates, respectively. The graph was obtained by plotting the surface pressure Π , measured by Wilhelmy plate, against the area per molecule a , which was derived from equation mentioned in Theoretical section 2.40, giving the final expression as follows

$$a = \frac{AN_A}{cV} \quad (3.2)$$

where A is the actual through top area, N_A is Avogadro constant, c is the molar concentration of the solution, and V is the volume injected onto a water sub-phase. The molar concentration for both 'Finding' and 'Deposition' of Ni(salen) was 5 mM ($M = \text{mol/L}$). The volume $V_{\text{FINDING}} = 250 \mu\text{L}$ and $V_{\text{DEPOSITION}} = 250 \mu\text{L}$. The isotherm is a very first characteristic of the compound regarding the deposition step. During the 'Finding' deposition, the isotherm was estimated to be at $\Pi = 15 \text{ mN/m}$ (i.e. where the curve starts to saturate). This pressure was then applied during the deposition onto substrates.

3. EXPERIMENT

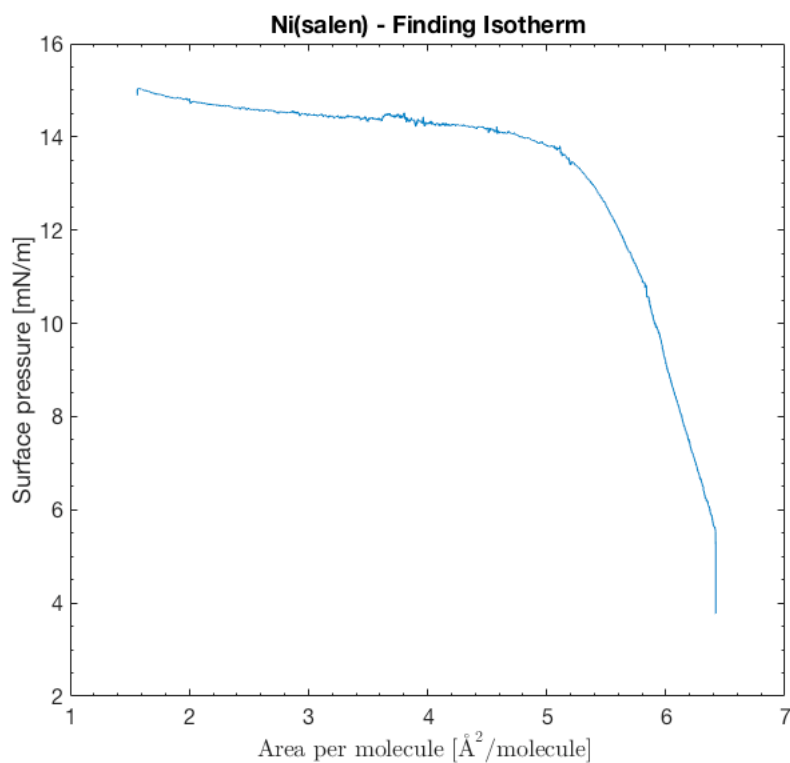


Figure 3.26: Graph of 'Finding' an isotherm for Ni(salen) compound. This was done with measuring the surface pressure Π versus area per molecule a for a blank deposition (i.e. without substrates).

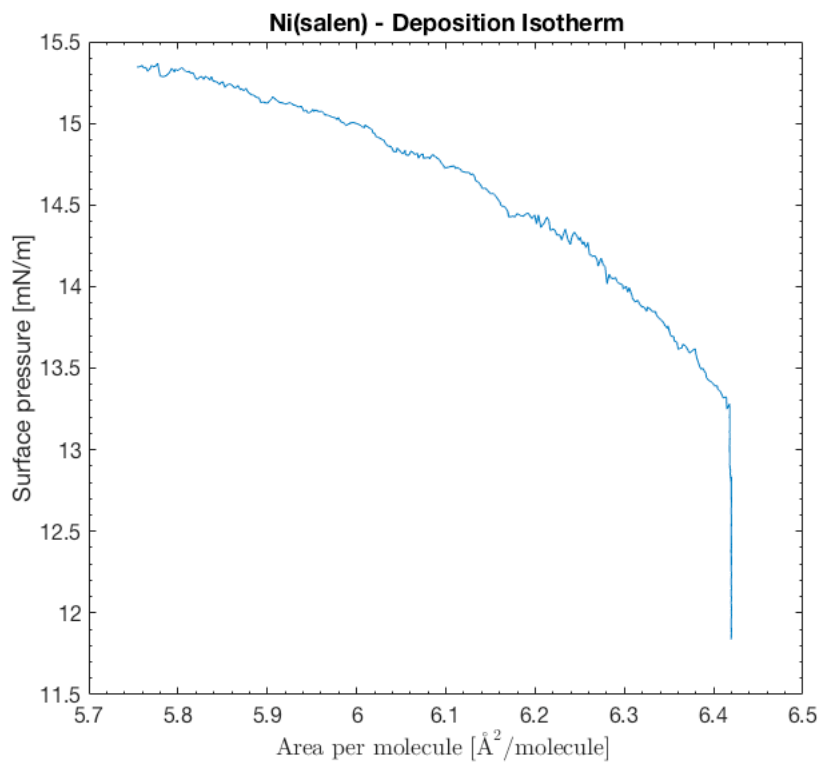


Figure 3.27: Graph of 'Deposition' isotherm for Ni(salen) compound. The surface pressure $\Pi = 15 \text{ mN/m}$ was applied for the deposition.

3.6.3. Raman Spectroscopy

Figure (3.28) shows Raman spectrum for powder Ni(salen). Peaks found are in accordance with other observations [49].

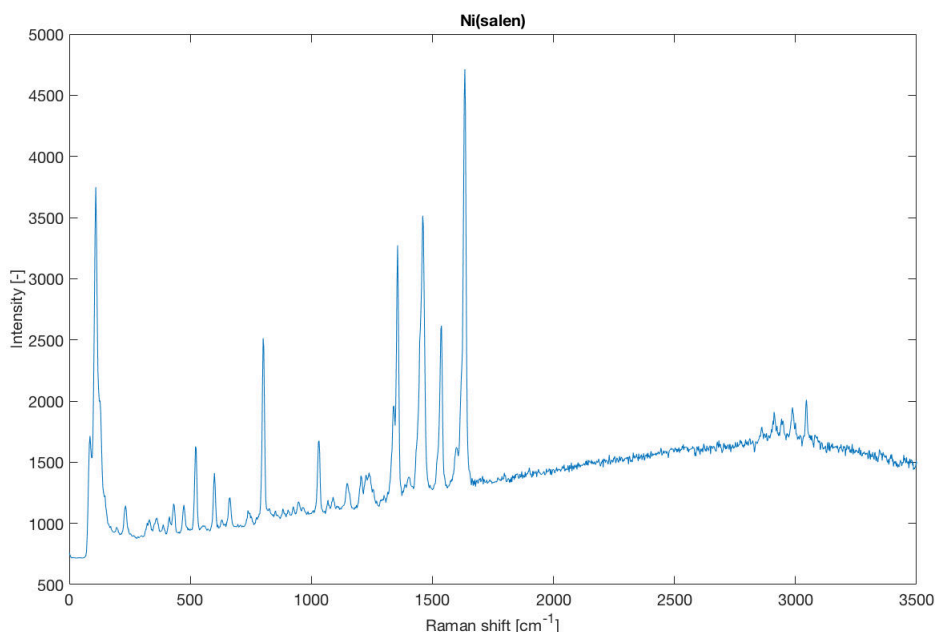


Figure 3.28: Raman spectrum for powder Ni(salen). Excitation wavelength was 532 nm. Spectrum was acquired at SAS in Bratislava, Slovak Republic.

Figure (3.29) shows spectrum for deposited thin film. There were only two contributions observed: Si/SiO₂ substrate (2.18) and FLG (3.11) with no sign of powder (3.28) spectrum. This can be attributed to thickness of deposited needle-like structures. This compound had also the worst coverage and homogeneity.

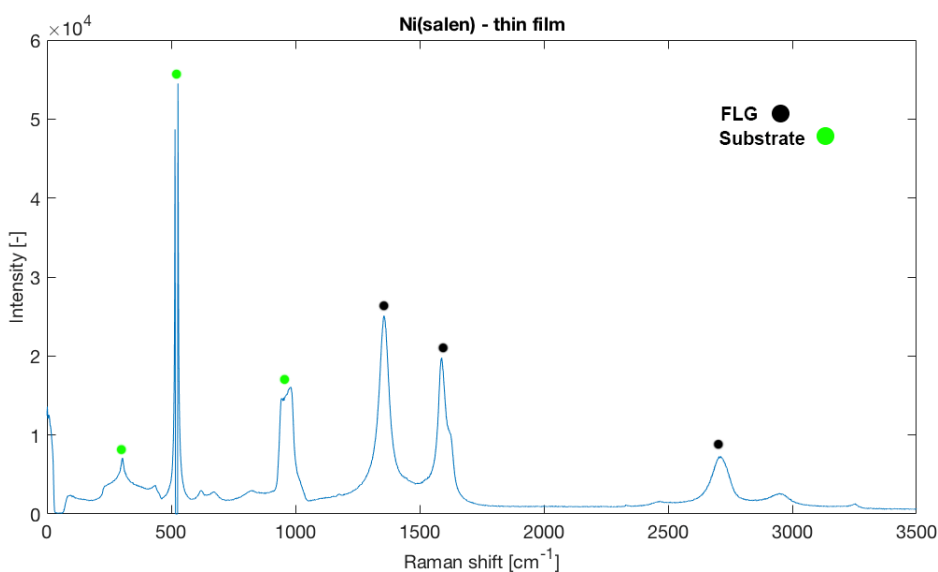


Figure 3.29: Raman spectrum for deposited Ni(salen) on graphene-covered substrate. Excitation wavelength was 532 nm. Spectrum was acquired at MUNI in Brno, Czech Republic.

3. EXPERIMENT

3.6.4. High Frequency EPR

Figures (3.30) and (3.31) show HFEPR measurements of Ni(salen) compound which gives very weak signals at around $g \approx 2.023$ and $g \approx 1.988$. The Ni(salen) has $3d^8$ square planar low-spin configuration with no unpaired electrons. Therefore, such compound is so-called EPR silent and only spectra $g \approx g_e$, resulting from impurities, substrate, and FLG, were observed.

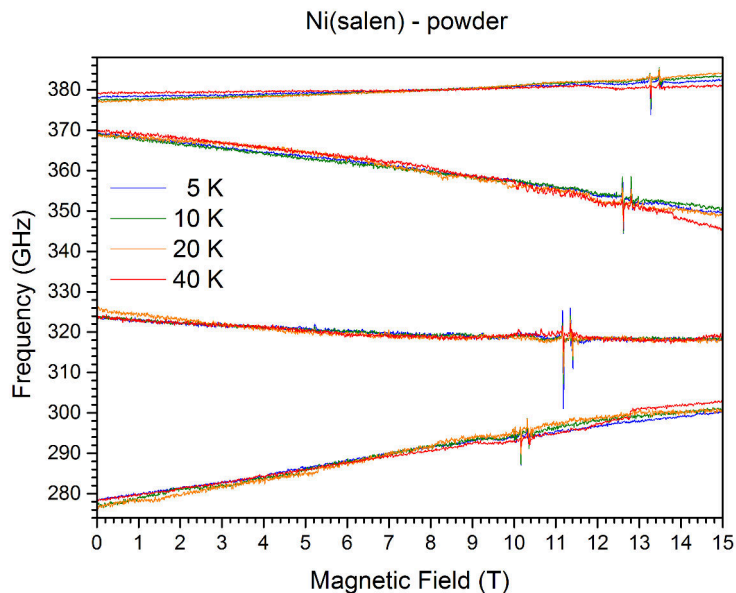


Figure 3.30: HFEPR spectra of temperature dependant Ni(salen) powder for four frequencies.

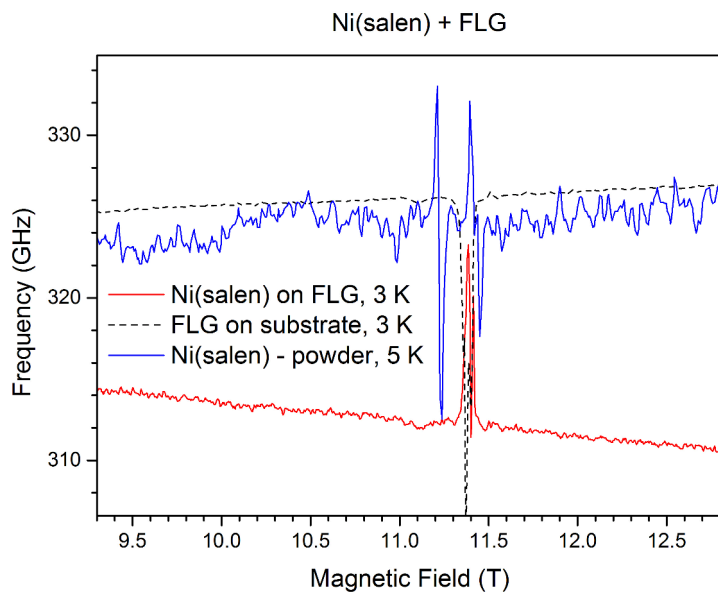


Figure 3.31: Comparison of Ni(salen) on FLG, graphene-covered substrate, and powder Ni(salen).

3.6.5. Scanning Electron Microscopy

Figure (3.32) shows SEM image of deposited Ni(salen) on the graphene-covered substrate. This compound is highly soluble in dichloromethane. Molar concentration of solution was $c = 5$ mM. Approximate size of crystals formed was $(0.5 - 10) \mu\text{m}$. The apparent needle-like structure is caused by the preferential growth rate along $\langle 010 \rangle$ direction [50]. The grey structure behind corresponds to FLG and black background to the Si/SiO₂ substrate.

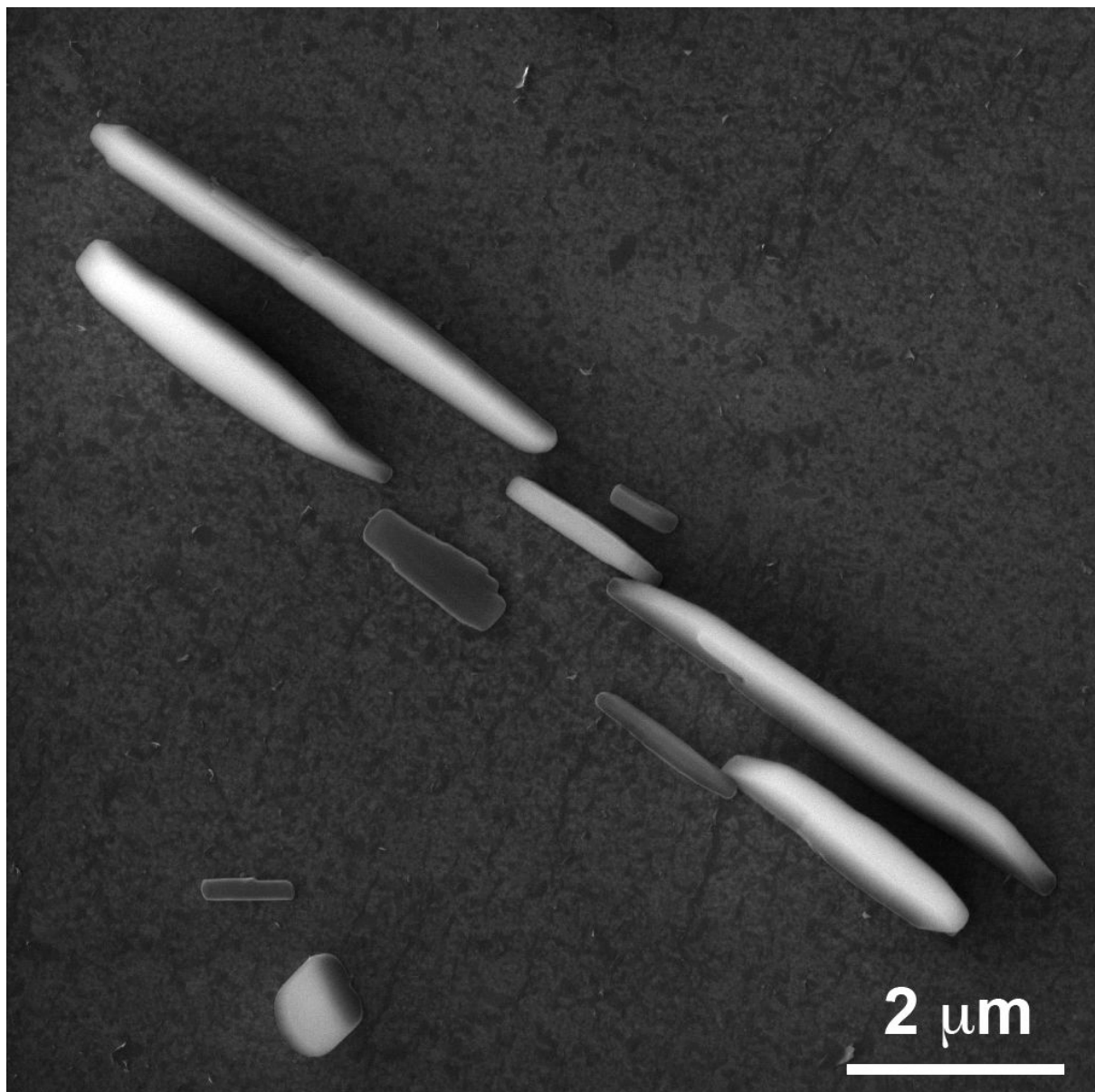


Figure 3.32: SEM image of Ni(salen) on the graphene-covered substrate. Voltage used: 30 kV. Detector: secondary electrons. Image was acquired at CEITEC - BUT, Czech Republic.

3. EXPERIMENT

3.7. DM15N

3.7.1. Synthesis and Structure

The third investigated compound was DM15N. The compound was synthesised at the Palacký University Olomouc, Czech Republic. For the synthesis, 164 mg of CoBr_2 was dissolved in 20 mL of methanol under the inert N_2 atmosphere. Afterwards, 277 mg of DPPF-(1,1 -Ferrocenediyl-bis(diphenylphosphine)) was dissolved in 30 mL of dichloromethane, and added to the first solution. The colour of formerly blue solution turned upon addition of DPPF to green colour. The final crystalline product was prepared by slow-diffusion of diethyl ether in the prepared solution. Final crystals were filtered and dried. Figure (3.33) illustrates the molecular structure of this cobalt ferrocene with two bromides.

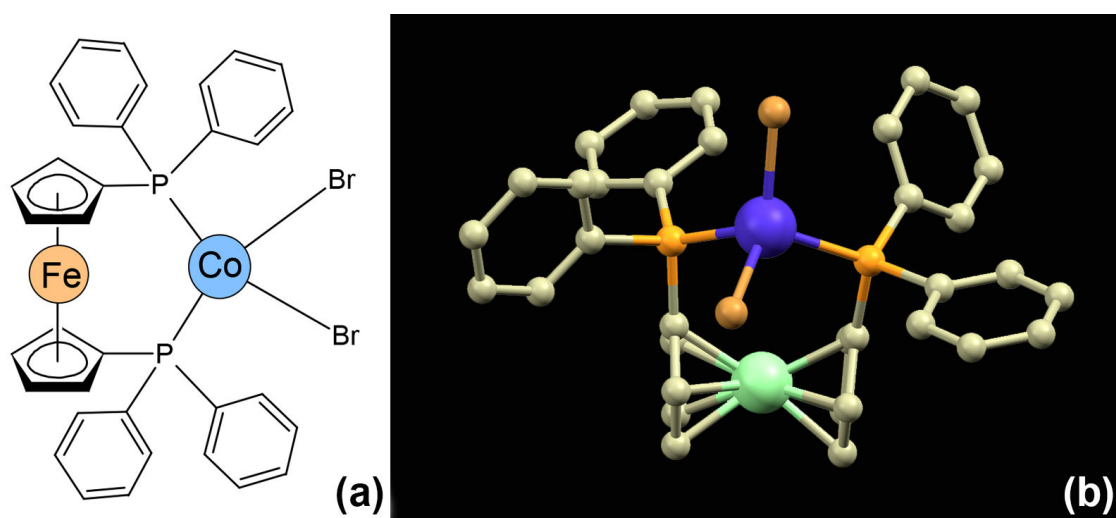


Figure 3.33: Illustration of DM15N compound. (a) 2D sketch of chemical structure, (b) 3D view on the compound with measured distance $d = 11.5 \text{ \AA}$ between two furthest lying carbon atoms. Hydrogen atoms are omitted for the sake of clarity. With permission of Dr. Ivan Nemeec.

3.7.2. Isotherms

Figures (3.34) and (3.35) show isotherms for DM15N compound obtained during the blank deposition and actual deposition onto substrates, respectively. The graph was obtained by plotting the surface pressure Π , measured by Wilhelmy plate, against the area per molecule a , which was derived from equation mentioned in Theoretical section 2.40, giving the final expression as follows

$$a = \frac{AN_A}{cV} \quad (3.3)$$

where A is the actual through top area, N_A is Avogadro constant, c is the molar concentration of the solution, and V is the volume injected onto a water sub-phase. The molar concentration for both 'Finding' and 'Deposition' of DM15N was 5 mM ($\text{M} = \text{mol/L}$). The volume $V_{\text{FINDING}} = 200 \text{ \mu L}$ and $V_{\text{DEPOSITION}} = 200 \text{ \mu L}$. The isotherm is a very first characteristic of the compound regarding the deposition step. During the 'Finding' deposition, the isotherm was estimated to be at $\Pi = 28 \text{ mN/m}$ (i.e. where the curve starts to saturate). This pressure was then applied during the deposition onto substrates.

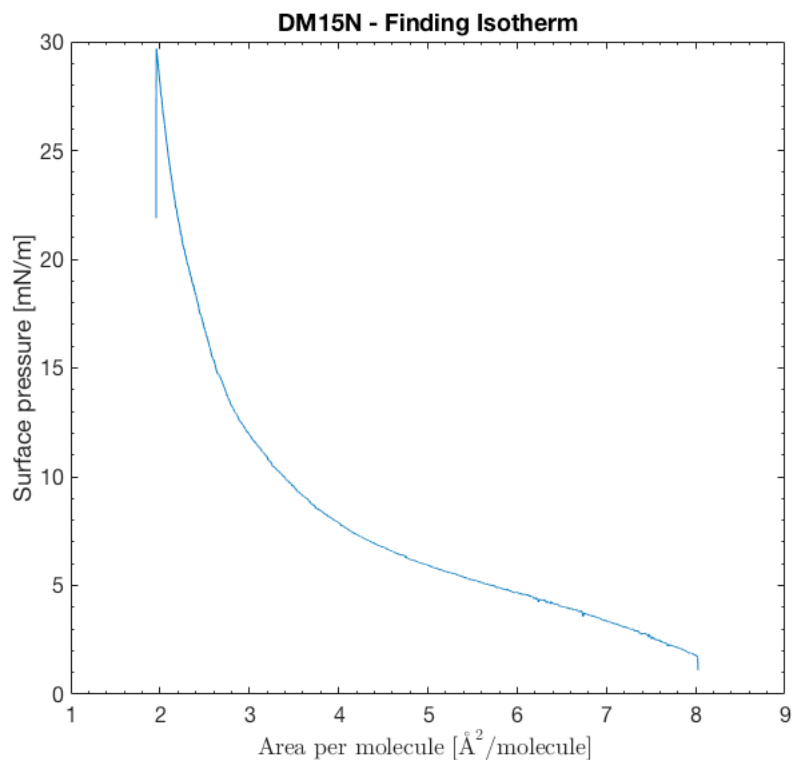


Figure 3.34: Graph of 'Finding' an isotherm for DM15N compound. This was done with measuring the surface pressure Π versus area per molecule a for a blank deposition (i.e. without substrates).

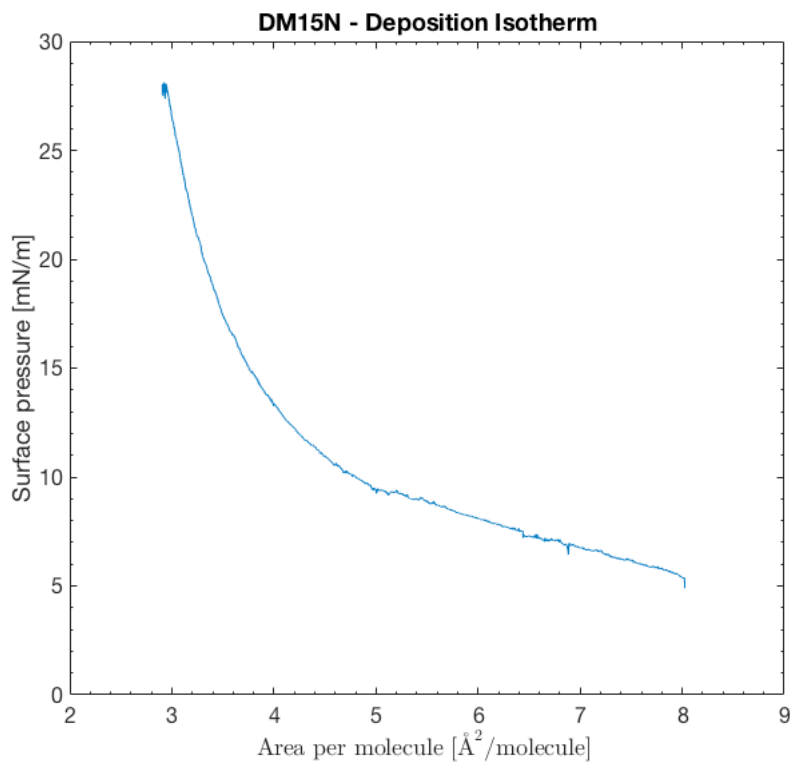


Figure 3.35: Graph of 'Deposition' isotherm for DM15N compound. The surface pressure $\Pi = 28 \text{ mN/m}$ was applied for the deposition.

3. EXPERIMENT

3.7.3. Raman Spectroscopy

Figure (3.36) shows Raman spectrum for powder DM15N.

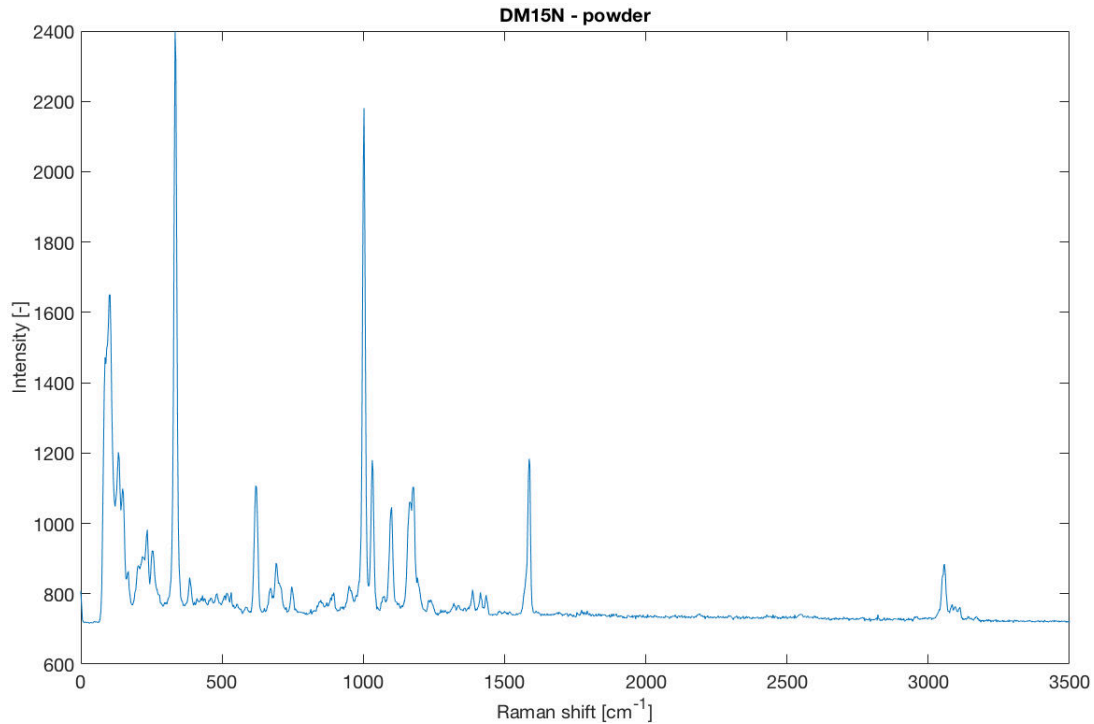


Figure 3.36: Raman spectrum for powder DM15N. Excitation wavelength was 532 nm. Spectrum was acquired at SAS in Bratislava, Slovak Republic.

Figure (3.37) shows spectrum for deposited thin film. There were three contributions observed: Si/SiO₂ substrate (2.18) and FLG (3.11), and DM15N (3.36) powder spectrum. The intensity of DM15N signal was, however, not very strong in comparison to Si/SiO₂ substrate and FLG layer, albeit microRaman was used. This can be attributed to film thickness. Consequently, only one specific peak for DM15N was observed.

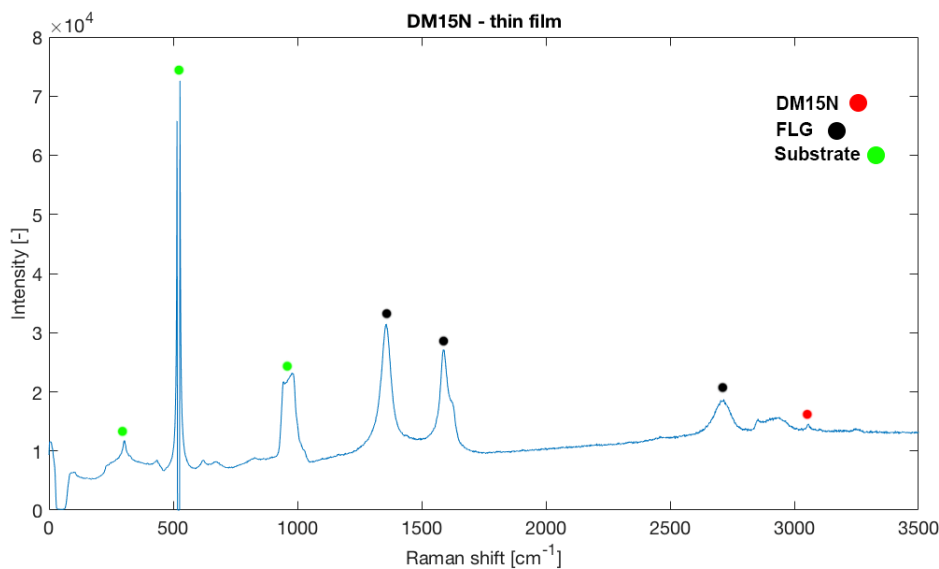


Figure 3.37: Raman spectrum of DM15N deposited on graphene-covered substrate. Excitation wavelength was 532 nm. Spectrum was acquired at MUNI in Brno, Czech Republic.

3.7.4. High Frequency EPR

The cobalt ferrocene DM15N contains two transition metals. Cobalt has $3d^7$ octahedral high-spin configuration with 3 unpaired electrons. Iron has octahedral low-spin $3d^6$ electron configuration with no unpaired electron and is EPR silent, and thus the final spin number is $3/2$.

Figure (3.38) shows measured HFEPR spectra of DM15N. Table (3.7) illustrates that zero-field splitting parameters D and E , as well as g -value components, are in fair agreement with theoretical simulation. At this point, it is important to note, that one of the recent interest is to narrow the gap between theory and experiment. Moreover, feedback to chemists in order to fine tune properties of prepared single-molecule magnets is another priority.

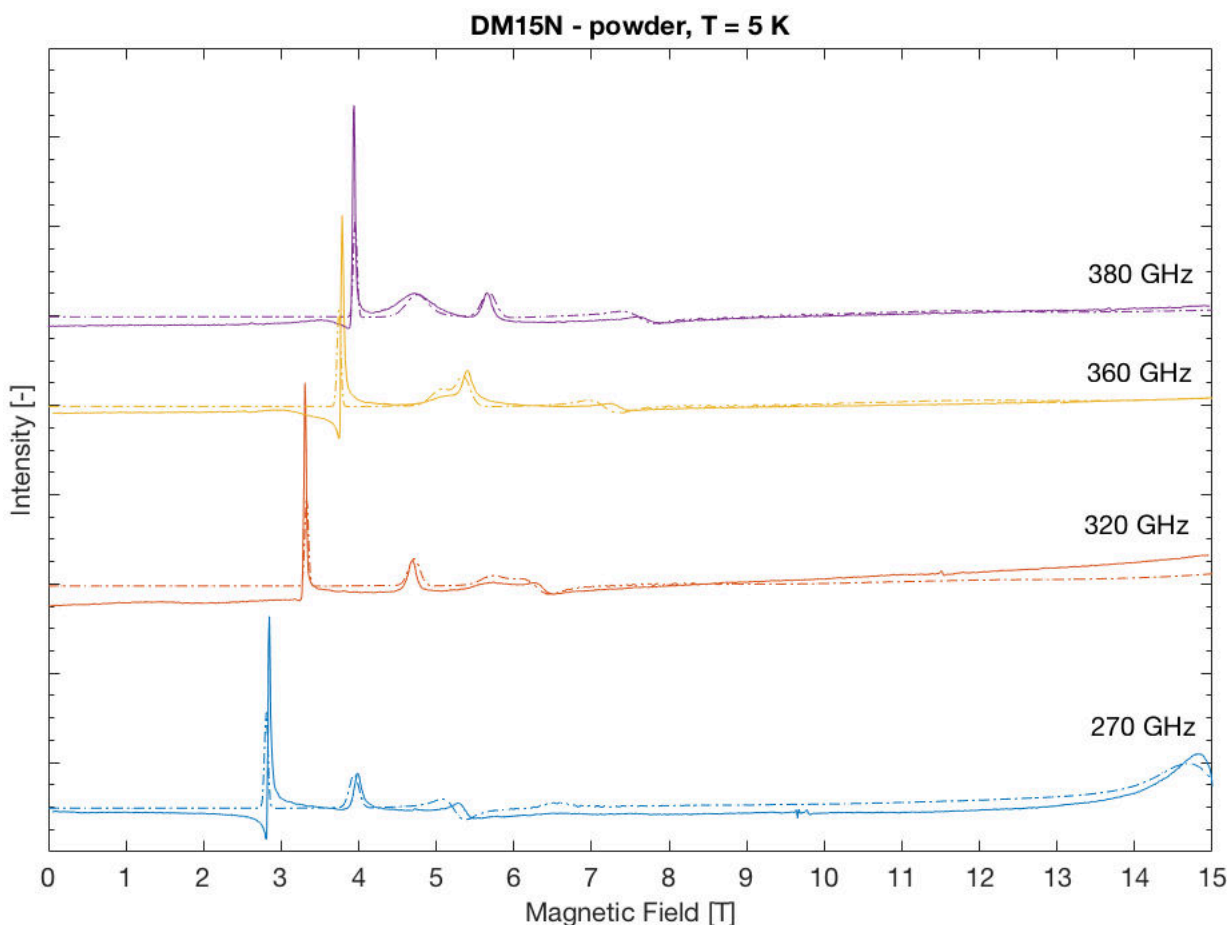


Figure 3.38: HFEPR spectra for four frequencies at $T = 5$ K. Full lines represent measurement and dashed lines represent fit.

Table 3.7: Comparison of CASSCF/NEVPT2 *ab initio* simulation and HFEPR measurement.

Parameters	Spin	D [cm^{-1}]	E [cm^{-1}]	g_x	g_y	g_z
CASSCF/NEVPT2	$3/2$	-9.78	-1.04	2.20	2.22	2.31
HFEPR	$3/2$	-11.20	-1.01	2.22	2.22	2.31

3. EXPERIMENT

Figure (3.39) shows a temperature dependence of DM15N compound revealing an evident shift in peak intensities as the temperature was risen.

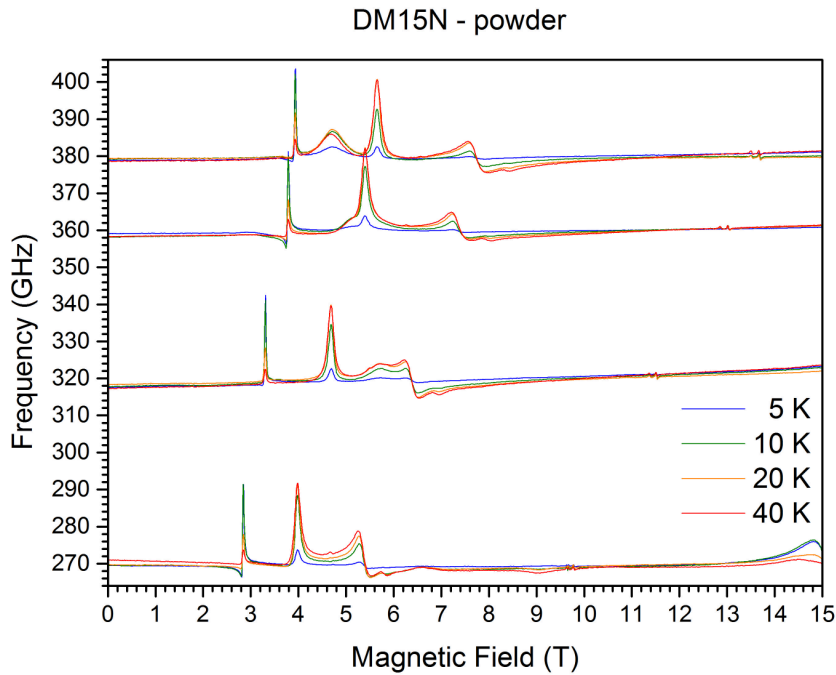


Figure 3.39: Temperature dependence of DM15N measured by HFEPR spectroscopy.

Figure (3.40) shows spectrum for DM15N compound on graphene-covered substrate in the form of a thin film. The black line represents measurement and red calculation for DM15N - bulk, peaks from 3 – 6 T, and an electron peak around 11.4 T originating from FLG. The $g = 2.005$ was used for the fit.

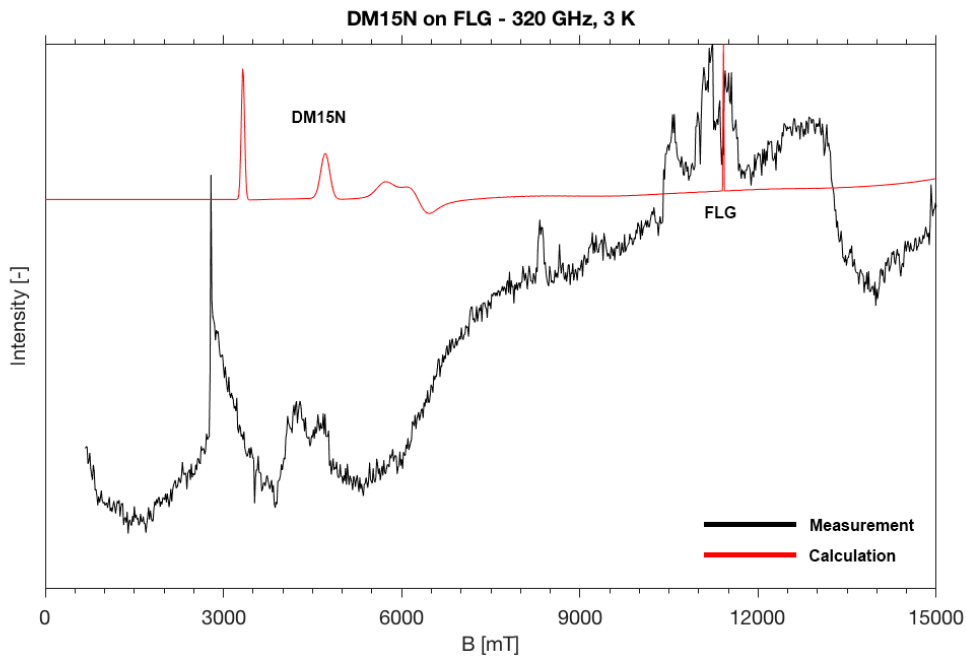


Figure 3.40: DM15N on graphene-covered substrate at $\nu = 320$ GHz and $T = 3$ K.

Figure (3.41) shows detail of spectrum of DM15N compound on FLG in the form of a thin film. The black line represents measurement and red calculation for DM15N - bulk.

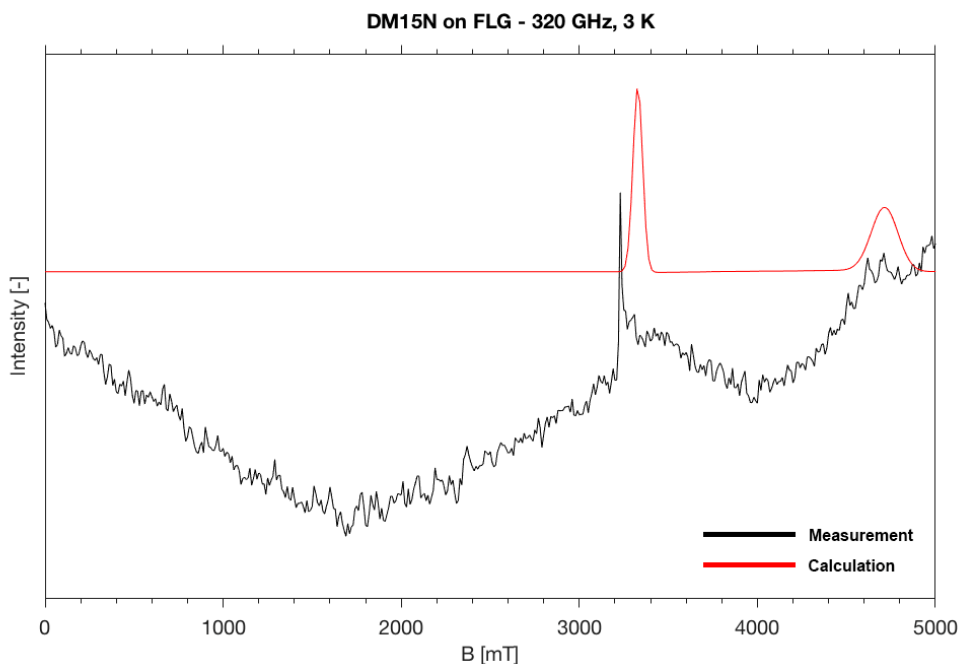


Figure 3.41: Detail of DM15N on graphene-covered substrate.

Figure (3.42) illustrates DM15N on FLG from Figure (3.41) with magnetic field swept from -5 T to 5 T and fitted with Drude conductivity revealing the charge carrier mobility $\mu = 3500 \text{ cm}^2 \text{ V}^{-1} \text{ s}^{-1}$, which is slightly higher than for bulk graphite $\mu = 3000 \text{ cm}^2 \text{ V}^{-1} \text{ s}^{-1}$ [51].

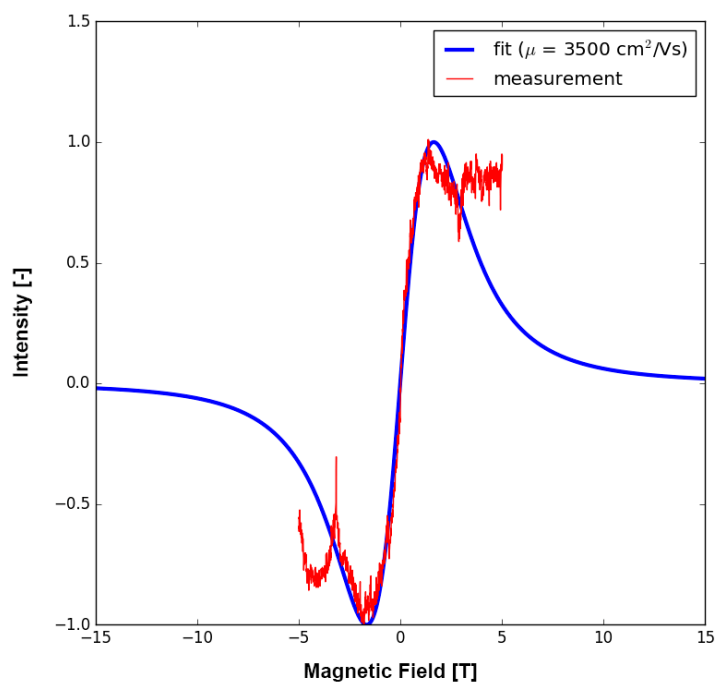


Figure 3.42: Measured DM15N compound and fitted according to classical Drude conductivity model. With help of Dipl.-Chem. Dominik Bloos.

3. EXPERIMENT

3.7.5. Scanning Electron Microscopy

Figure (3.43) shows SEM image of deposited DM15N on the graphene-covered substrate. This compound is highly soluble in dichloromethane. Molar concentration of solution was $c = 5$ mM. Approximate size of crystals formed was $0.2 - 1 \mu\text{m}$. The apparent puzzle-like structure is characteristic for this compound. The grey structure behind corresponds to FLG and black background to the Si/SiO₂ substrate.

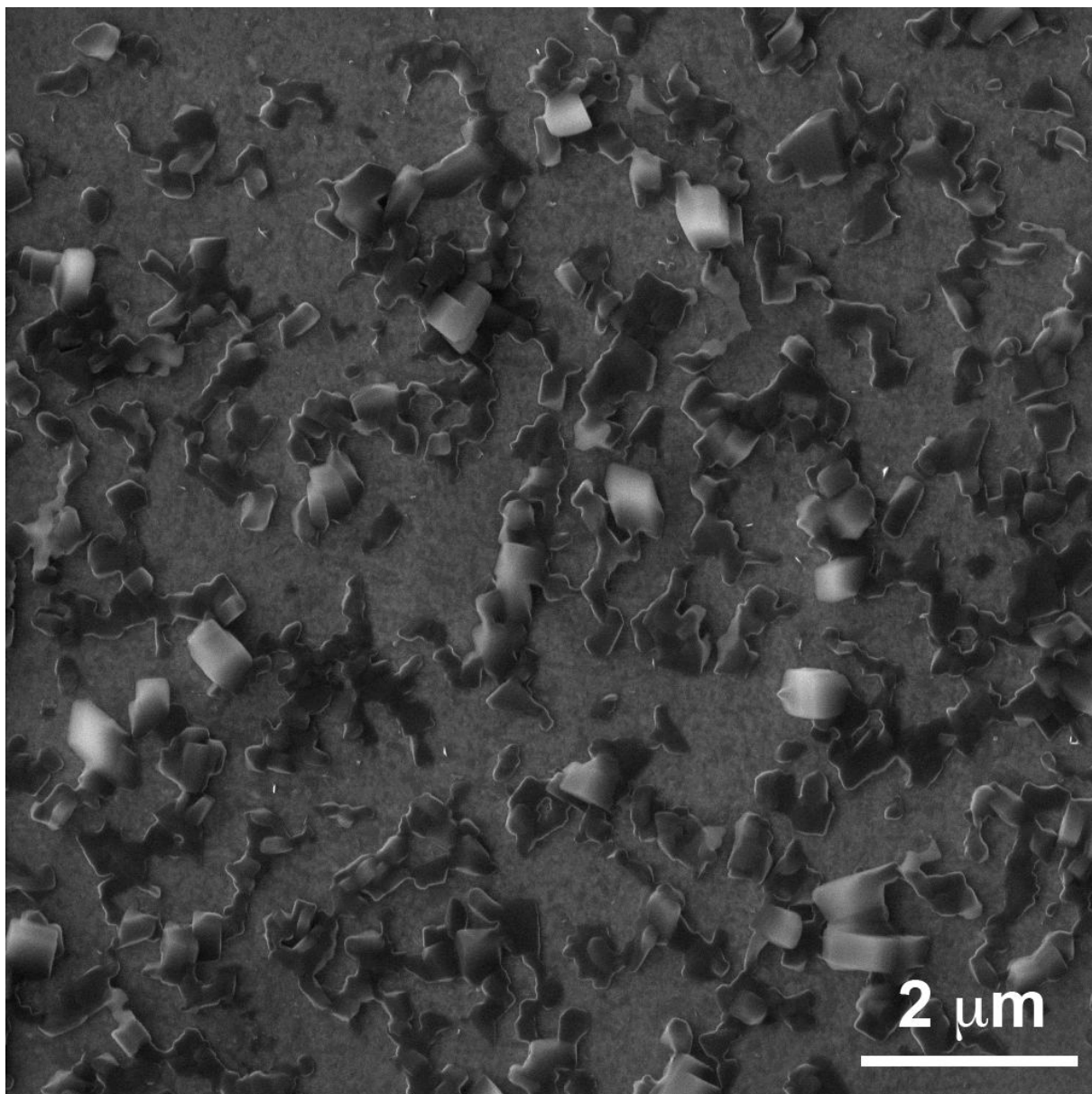


Figure 3.43: SEM image of DM15N on the graphene-covered substrate. Voltage used: 10 kV. Detector: secondary electrons. Image was acquired at CEITEC - BUT, Czech Republic.

3.8. DM18N

3.8.1. Synthesis and Structure

The second to last investigated compound was DM18N. The compound was also synthesised at the Palacký University Olomouc, Czech Republic. For the synthesis, 64.5 mg of CoCl_2 was dissolved in 20 mL of methanol under the inert N_2 atmosphere. Afterwards, 250 mg of DPPF-(1,1-Ferrocenediyl-bis(diphenylphosphine)) was dissolved in 30 mL of dichloromethane, and added to the first solution. The colour of formerly blue solution turned upon addition of DPPF to green colour. The final crystalline product was prepared by slow-diffusion of diethyl ether in the prepared solution. Final crystals were filtered and dried. Figure (3.44) illustrates the molecular structure of this cobalt ferrocene with two chlorides.

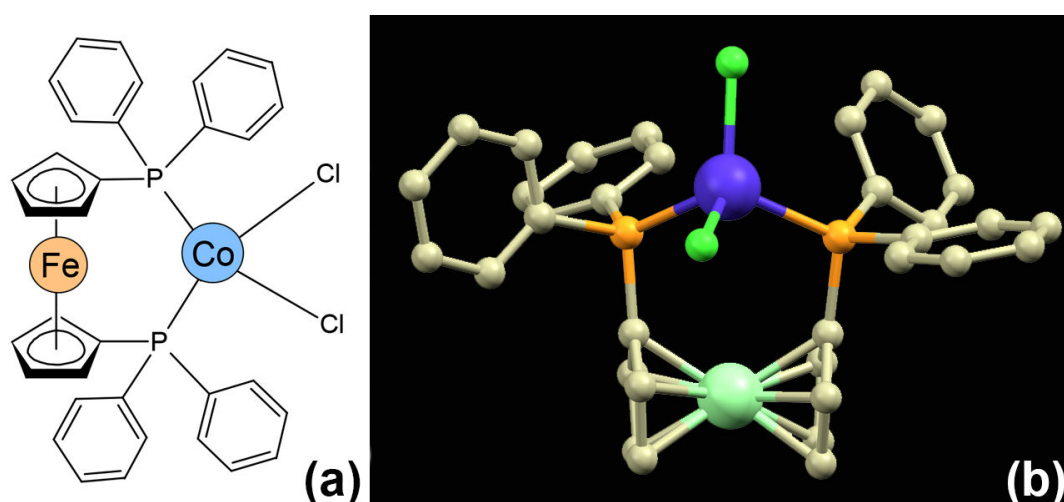


Figure 3.44: Illustration of DM18N compound. (a) 2D sketch of chemical structure, (b) 3D view on compound with measured distance $d = 11.5 \text{ \AA}$ between two furthest lying carbon atoms. Hydrogen atoms are omitted for the sake of clarity. With permission of Dr. Ivan Nemeč.

3.8.2. Isotherms

Figures (3.45) and (3.46) show isotherms for DM18N compound obtained during the blank deposition and actual deposition onto substrates, respectively. The graph was obtained by plotting the surface pressure Π , measured by Wilhelmy plate, against the area per molecule a , which was derived from equation mentioned in Theoretical section 2.40, giving the final expression as follows

$$a = \frac{AN_A}{cV} \quad (3.4)$$

where A is the actual through top area, N_A is Avogadro constant, c is the molar concentration of the solution, and V is the volume injected onto a water sub-phase. The molar concentration for both 'Finding' and 'Deposition' of DM18N was 5 mM ($M = \text{mol/L}$). The volume $V_{\text{FINDING}} = 250 \text{ \mu L}$ and $V_{\text{DEPOSITION}} = 300 \text{ \mu L}$. The isotherm is a very first characteristic of the compound regarding the deposition step. During the 'Finding' deposition, the isotherm was estimated to be at $\Pi = 27 \text{ mN/m}$ (i.e. where the curve starts to saturate). This pressure was then applied during the deposition onto substrates.

3. EXPERIMENT

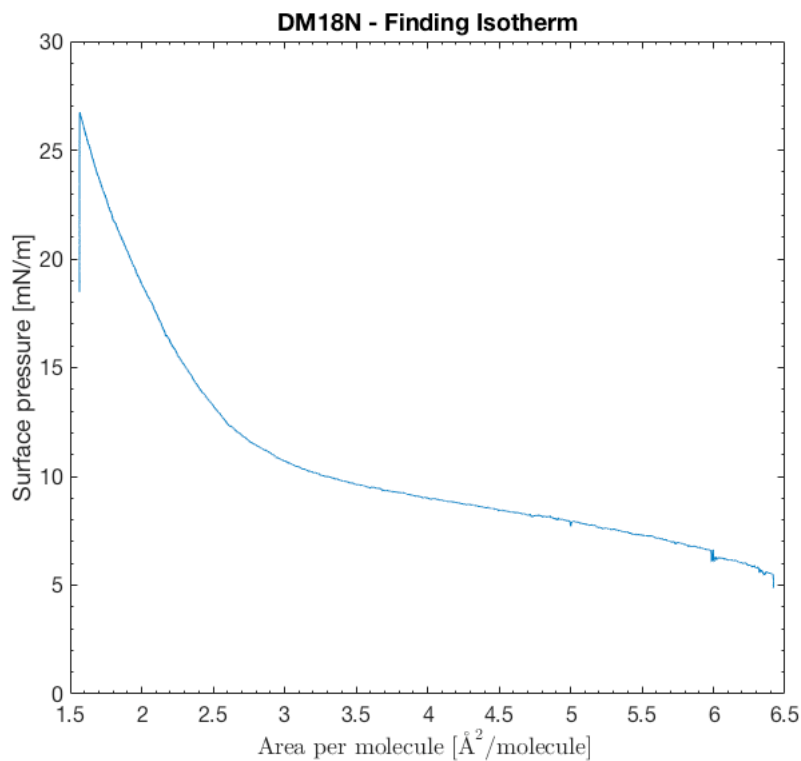


Figure 3.45: Graph of 'Finding' an isotherm for DM18N compound. This was done with measuring the surface pressure Π versus area per molecule a for a blank deposition (i.e. without substrates).

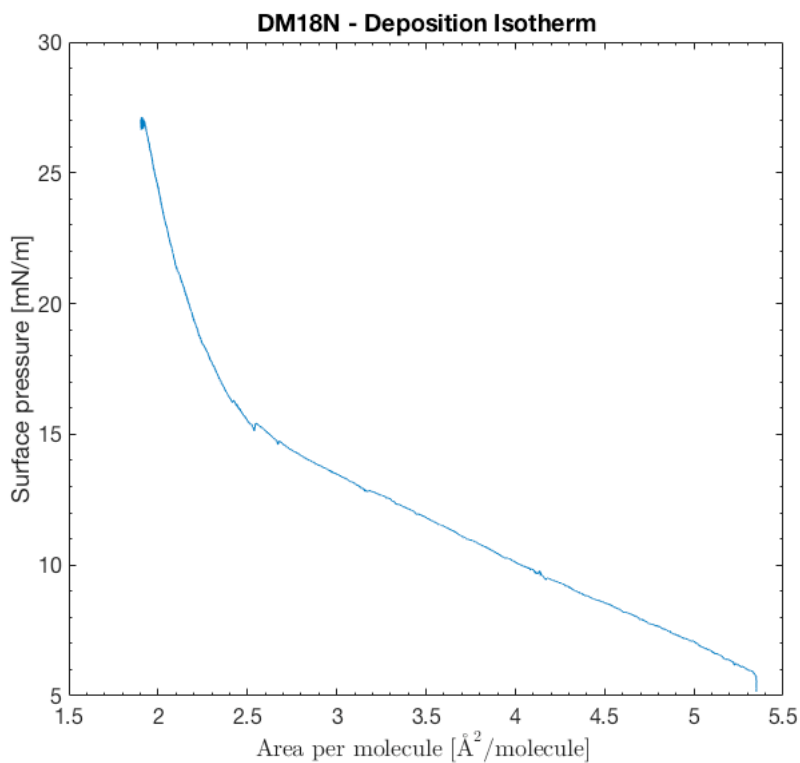


Figure 3.46: Graph of 'Deposition' isotherm for DM18N compound. The surface pressure $\Pi = 27 \text{ mN/m}$ was applied for the deposition.

3.8.3. Raman Spectroscopy

Figure (3.47) shows Raman spectrum for powder DM18N.

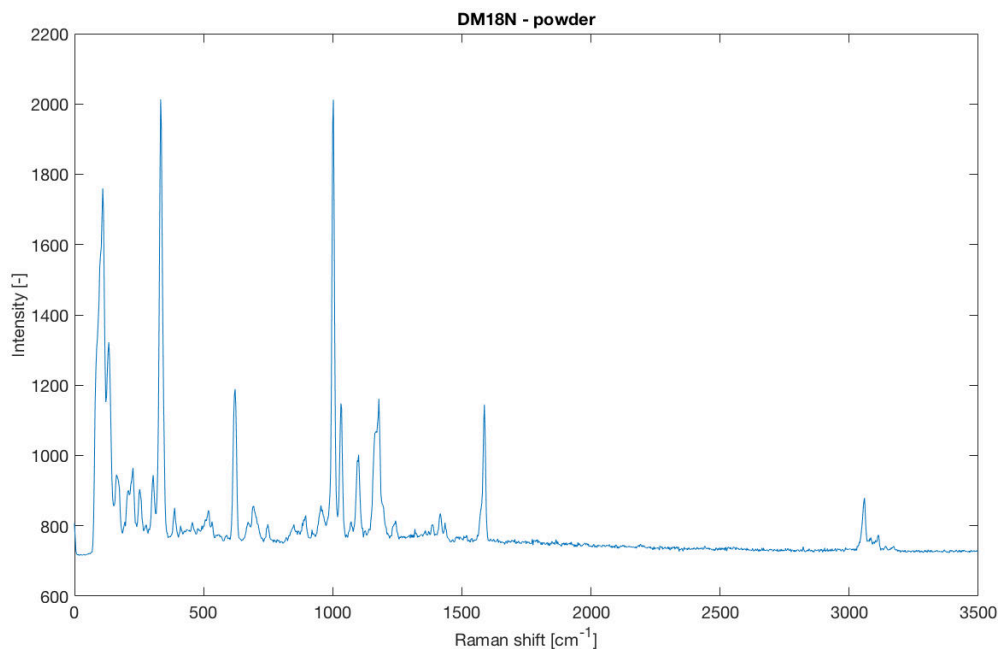


Figure 3.47: Raman spectrum for powder DM18N. Excitation wavelength was 532 nm. Spectrum was acquired at SAS in Bratislava, Slovak Republic.

Figure (3.48) shows spectrum for deposited thin film. There were three contributions observed: Si/SiO₂ substrate (2.18) and FLG (3.11), and DM18N (3.47) powder spectrum. The spectrum is similar to that of DM15N Figure (3.37). The signal of deposited DM18N is weak. This can be attributed to film thickness. Similarly to DM15N, only one specific peak for DM18N was observed.

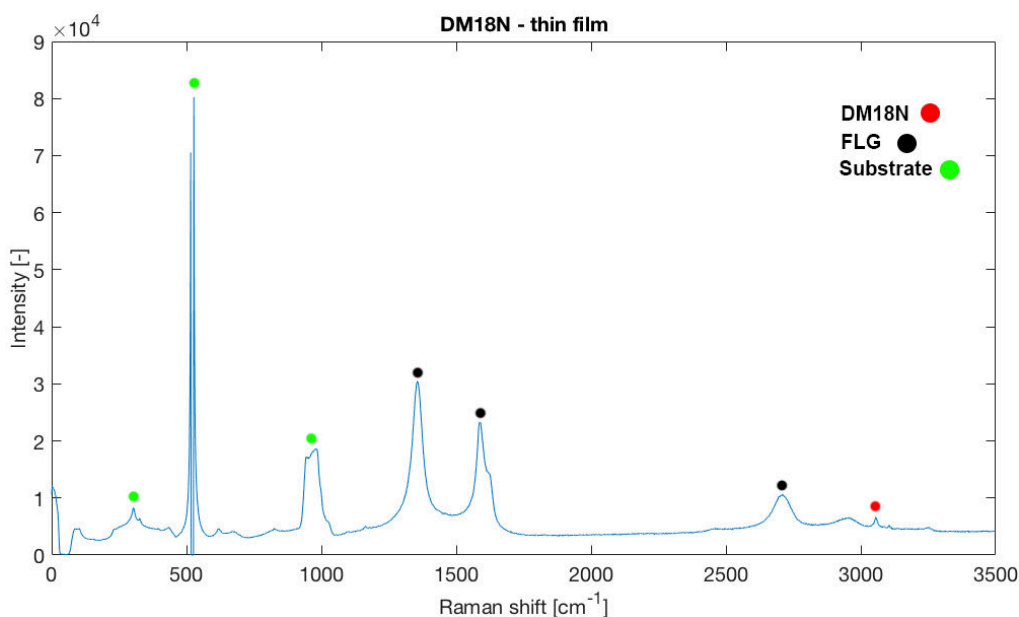


Figure 3.48: Raman spectrum of DM18N deposited on graphene-covered substrate. Excitation wavelength was 532 nm. Spectrum was acquired at MUNI in Brno, Czech Republic.

3. EXPERIMENT

3.8.4. High Frequency EPR

The cobalt ferrocene DM18N contains two transition metals. Cobalt has $3d^7$ octahedral high-spin configuration with 3 unpaired electrons. Iron has octahedral low-spin $3d^6$ electron configuration with no unpaired electron and is EPR silent, and thus the final spin number is $3/2$.

Figure (3.49) shows measured HF-EPR spectra of DM18N. Table (3.8) illustrates that zero-field splitting parameters D and E , as well as g -value components, are in fair agreement with theoretical simulation.

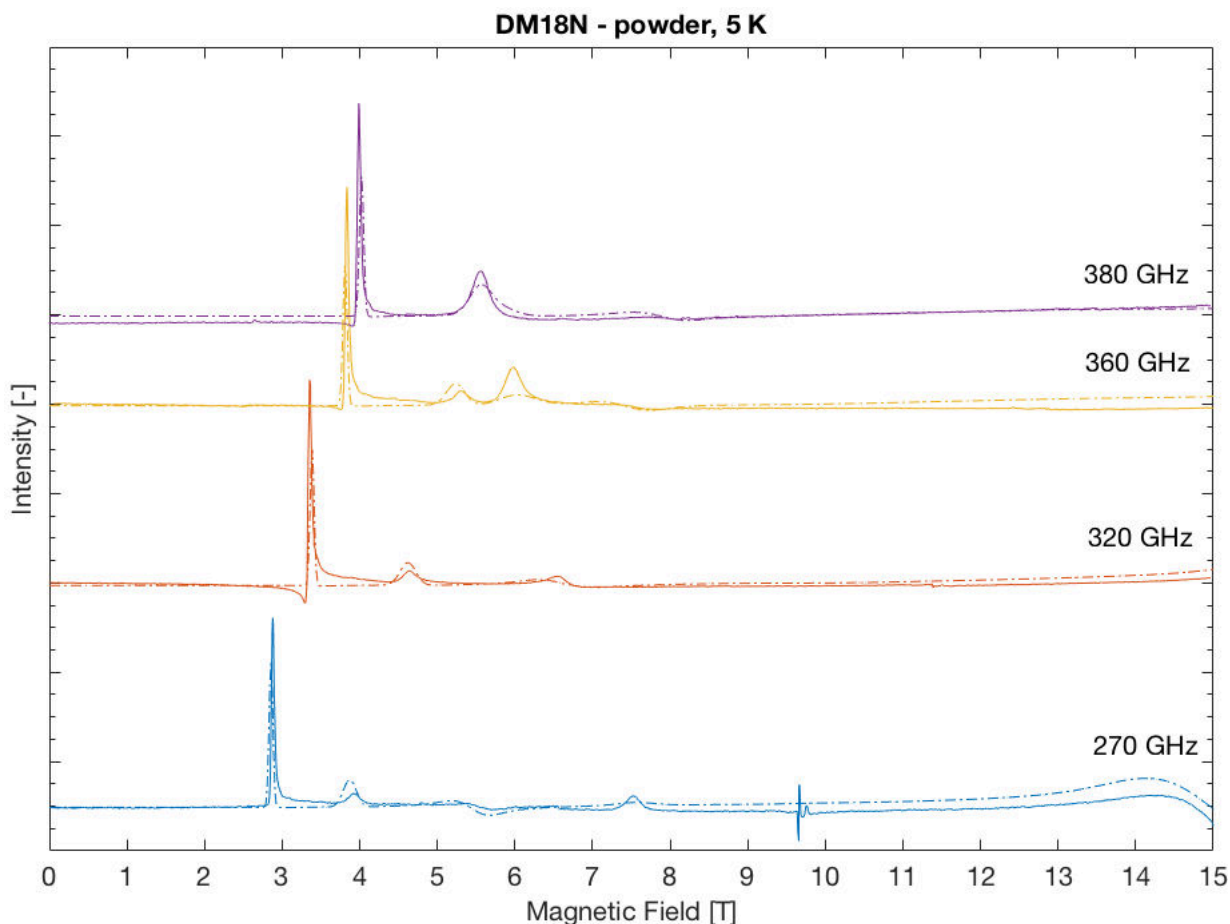


Figure 3.49: HF-EPR spectra of DM18N for four frequencies at $T = 5$ K. Full lines represent measurement and dashed lines represent fit.

Table 3.8: Comparison of CASSCF/NEVPT2 *ab initio* simulation and HF-EPR measurement.

Parameters	Spin	D [cm^{-1}]	E [cm^{-1}]	g_x	g_y	g_z
CASSCF/NEVPT2	$3/2$	-12.51	-1.54	2.18	2.20	2.31
HF-EPR	$3/2$	-12.00	-1.32	2.20	2.20	2.28

Figure (3.50) shows a temperature dependence of DM18N compound revealing an evident shift in peak intensities as the temperature was risen.

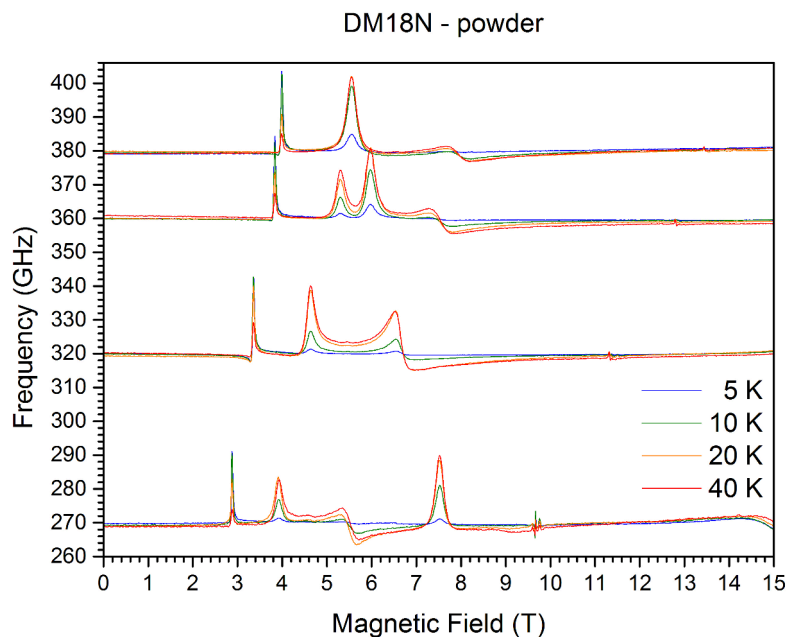


Figure 3.50: Temperature dependence of DM18N measured by HFEPR spectroscopy.

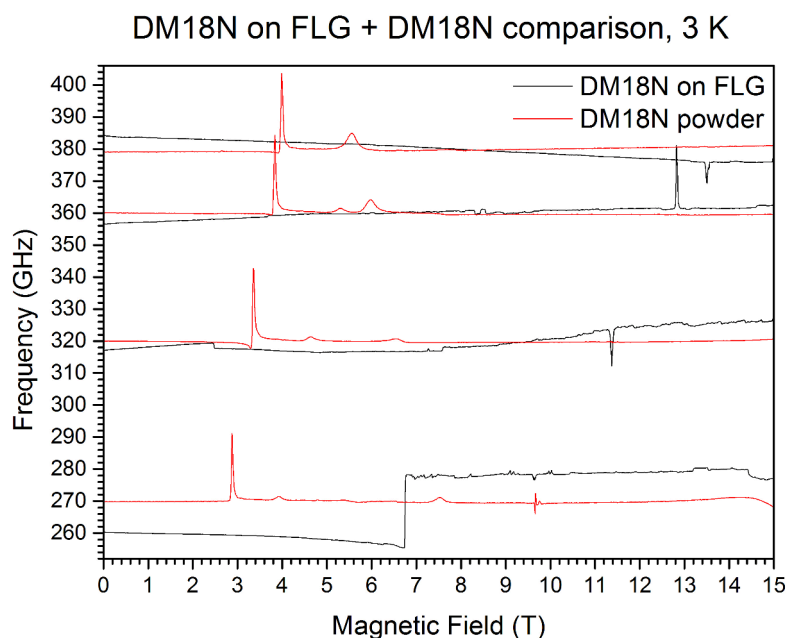


Figure 3.51: HFEPR spectra of DM18N compound on graphene-covered substrate for four frequencies at $T = 3$ K. Black lines represent measurement and red lines represent fit.

3. EXPERIMENT

3.8.5. Scanning Electron Microscopy

Figure (3.52) shows SEM image of deposited DM18N on the graphene-covered substrate. This compound is highly soluble in dichloromethane. Molar concentration of solution was $c = 5$ mM. This compound tends to form puzzle-like structure similar to that of DM15N shown in Figure (3.43).

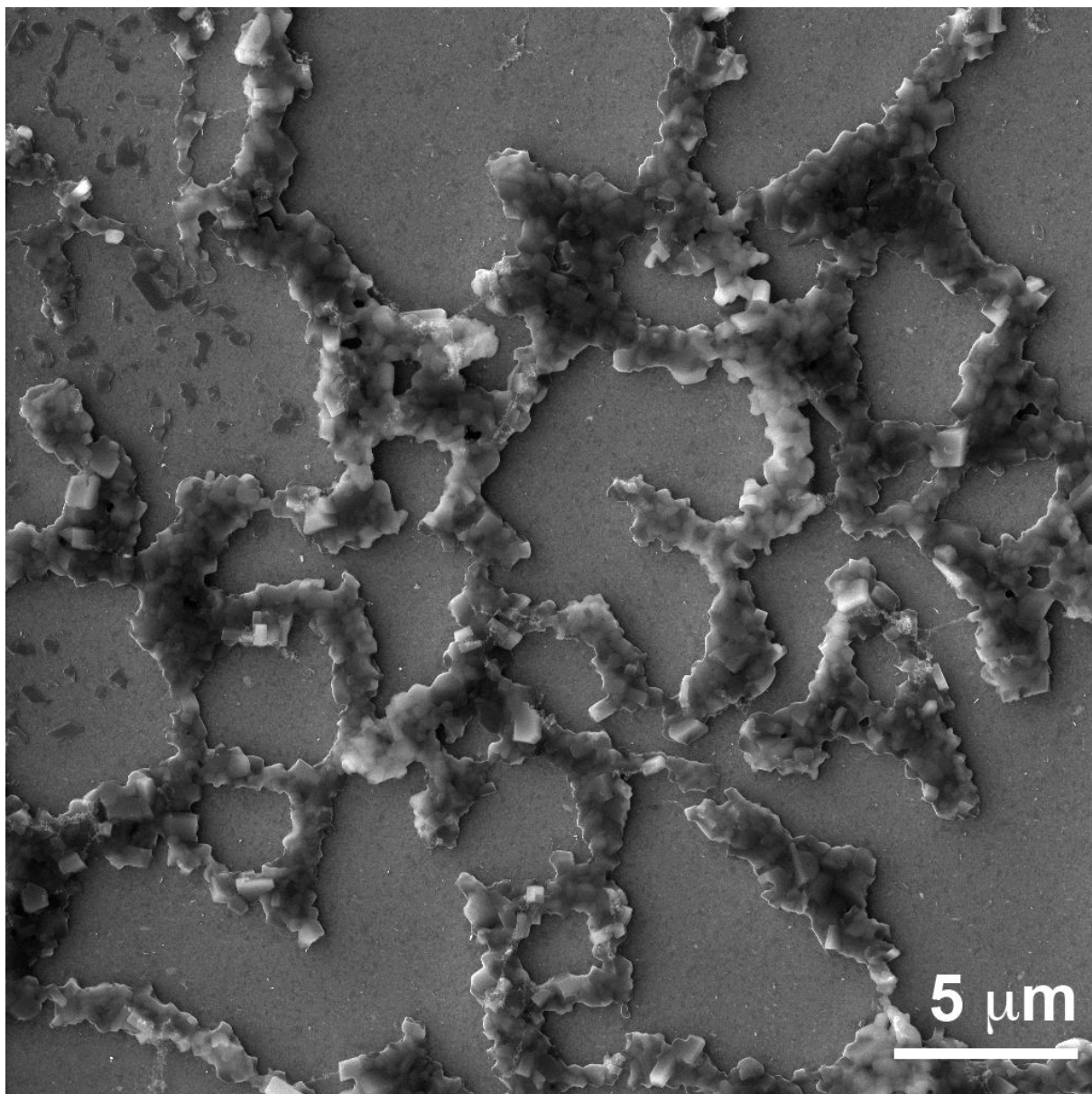


Figure 3.52: SEM image of DM18N on the graphene-covered substrate. Voltage used: 10 kV. Detector: secondary electrons. Image was acquired at CEITEC - BUT, Czech Republic.

3.9. ErPc₂

3.9.1. Synthesis and Structure

The last investigated compound was erbium phthalocyanine double-decker ErPc₂. The compound was synthesised at University of Stuttgart by the synthetic route described in Maria Dörfel's PhD thesis [52]. Figure (3.53) illustrates the structure of the erbium double-decker.

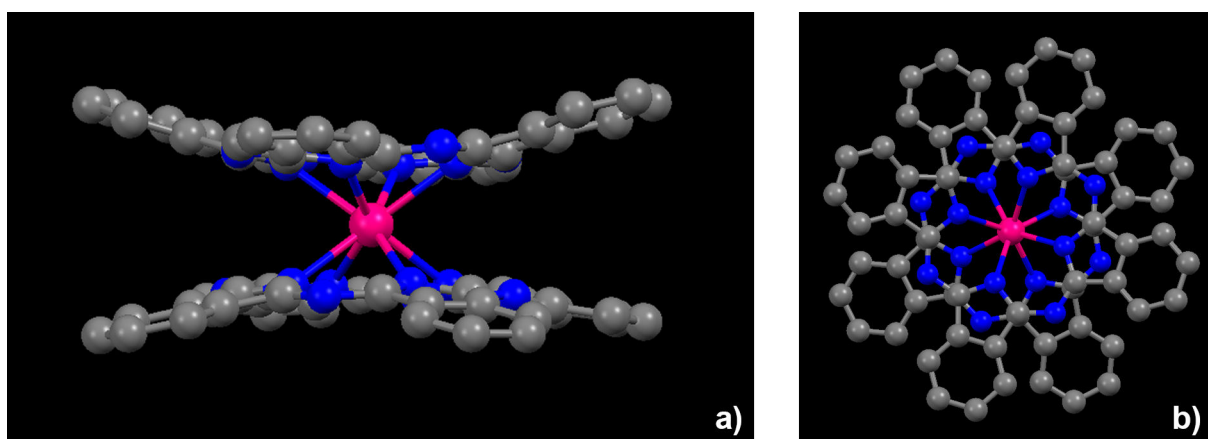


Figure 3.53: Illustration of ErPc₂ compound. (a) Front view, (b) side view on the compound with measured distance $d = 13.0 \text{ \AA}$ between two furthest lying carbon atoms. Hydrogen atoms and counter ion-tetrabutylammonium (TBA) are omitted for the sake of clarity.

3.9.2. Isotherms

Figures (3.54) and (3.55) show isotherms for ErPc₂ compound obtained during the blank deposition and actual deposition onto substrates, respectively. The graph was obtained by plotting the surface pressure Π , measured by Wilhelmy plate, against the area per molecule a , which was derived from equation mentioned in Theoretical section 2.40, giving the final expression as follows

$$a = \frac{AN_A}{cV} \quad (3.5)$$

where A is the actual through top area, N_A is Avogadro constant, c is the molar concentration of the solution, and V is the volume injected onto a water sub-phase. The molar concentration for both 'Finding' and 'Deposition' of ErPc₂ was 1 mM ($M = \text{mol/L}$). The volume $V_{\text{FINDING}} = 175 \text{ \mu L}$ and $V_{\text{DEPOSITION}} = 150 \text{ \mu L}$. The isotherm is a very first characteristic of the compound regarding the deposition step. During the 'Finding' deposition, the isotherm was estimated to be at $\Pi = 30 \text{ mN/m}$ (i.e. where the curve starts to saturate). This pressure was then applied during the deposition onto substrates.

3. EXPERIMENT

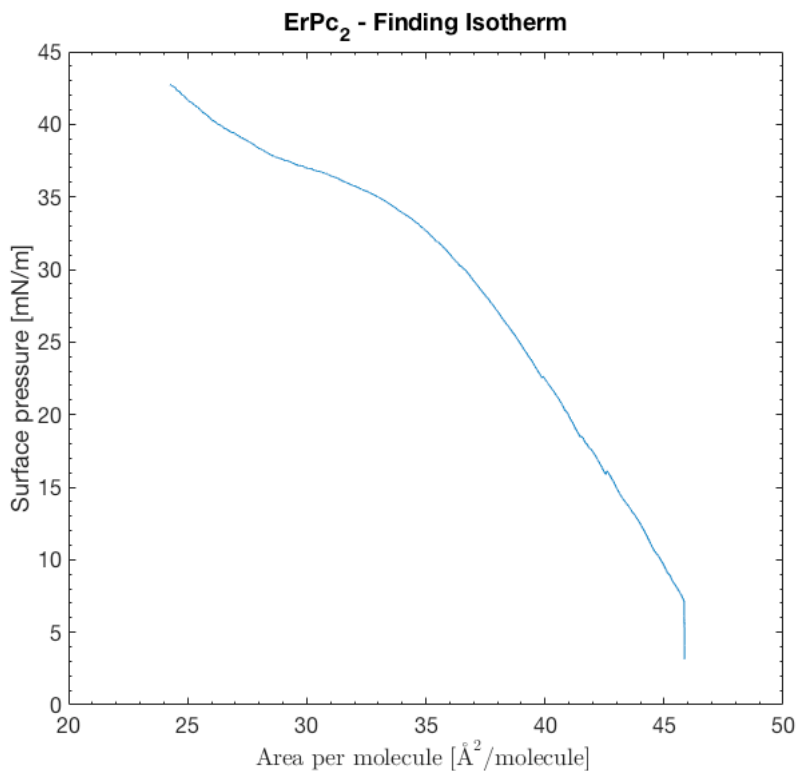


Figure 3.54: Graph of 'Finding' an isotherm for ErPc₂ compound. This was done with measuring the surface pressure Π versus area per molecule a for a blank deposition (i.e. without substrates).

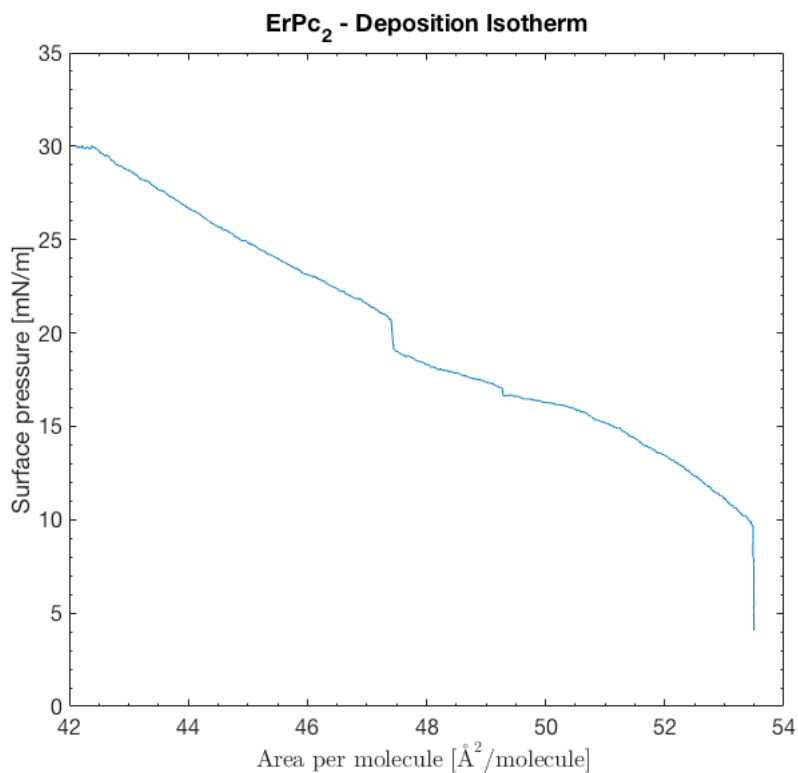


Figure 3.55: Graph of 'Deposition' isotherm for ErPc₂ compound. The surface pressure $\Pi = 30$ mN/m was applied for the deposition.

3.9.3. Raman Spectroscopy

Figure (3.56) shows Raman spectrum for powder ErPC₂.

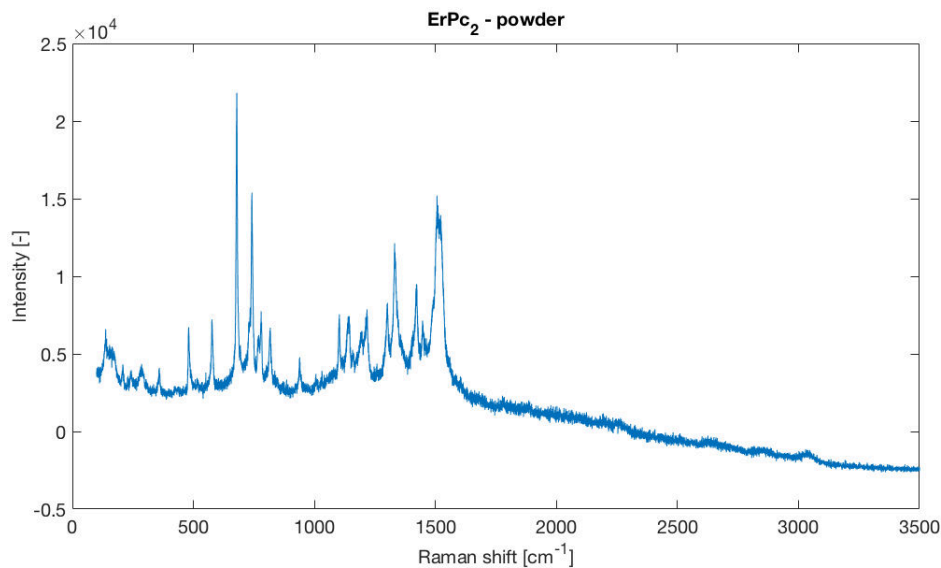


Figure 3.56: Raman spectrum for powder ErPC₂. Excitation wavelength was 632.8 nm. Spectrum was acquired at University of Stuttgart, Germany.

Figure (3.57) shows spectrum for deposited thin film. There were three contributions observed: Si/SiO₂ substrate (2.18) and FLG (3.11), and ErPC₂ (3.56) powder spectrum.

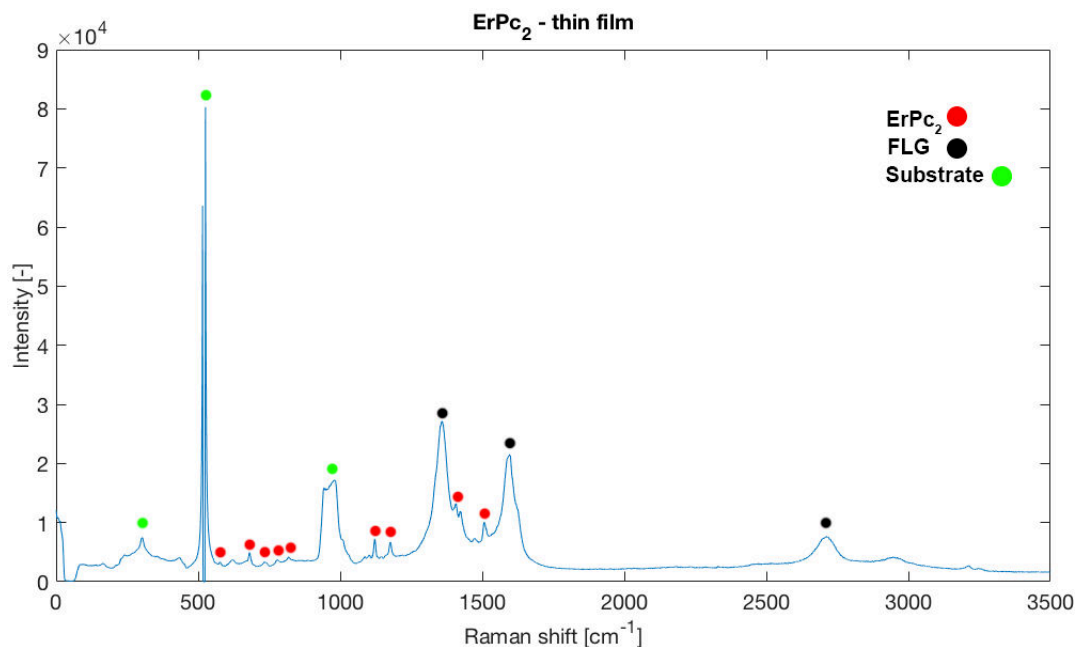


Figure 3.57: Raman spectrum of ErPC₂ deposited on graphene-covered substrate. Spectrum was acquired at MUNI in Brno, Czech Republic

3. EXPERIMENT

3.9.4. High Frequency EPR

The phthalocyanine double-decker ErPc_2 was fitted by using data from Maria Dörfel's PhD thesis [52]. Figure (3.58) shows measured HFEPR spectra of ErPc_2 . Table (3.9) illustrates that g-value components are in fair agreement with theoretical simulation.

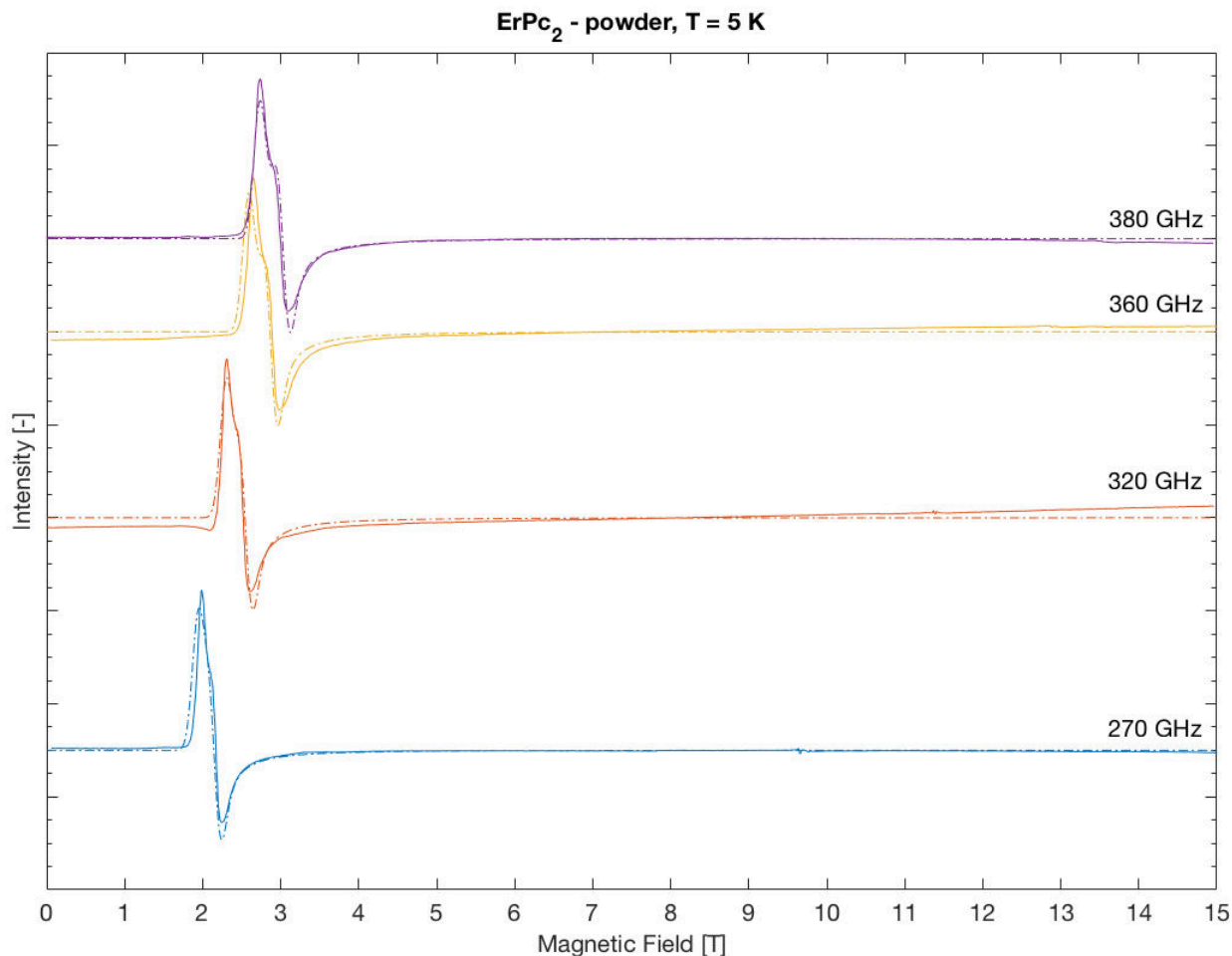


Figure 3.58: HFEPR spectra of ErPc_2 for four frequencies at $T = 5$ K. Full lines represent measured data, dashed lines represent fit.

Table 3.9: Comparison of CASSCF *ab initio* simulation, X band measurement, and HFEPR measurement.

Parameters	Spin	g_x	g_y	g_z
CASSCF	1/2	10.17	8.95	1.21
X band	1/2	9.28	9.53	1.66
HFEPR	1/2	9.95	8.95	1.21

Figure (3.59) shows a temperature dependence of ErPc₂ compound revealing no evident shift in peak intensities as the temperature was risen.

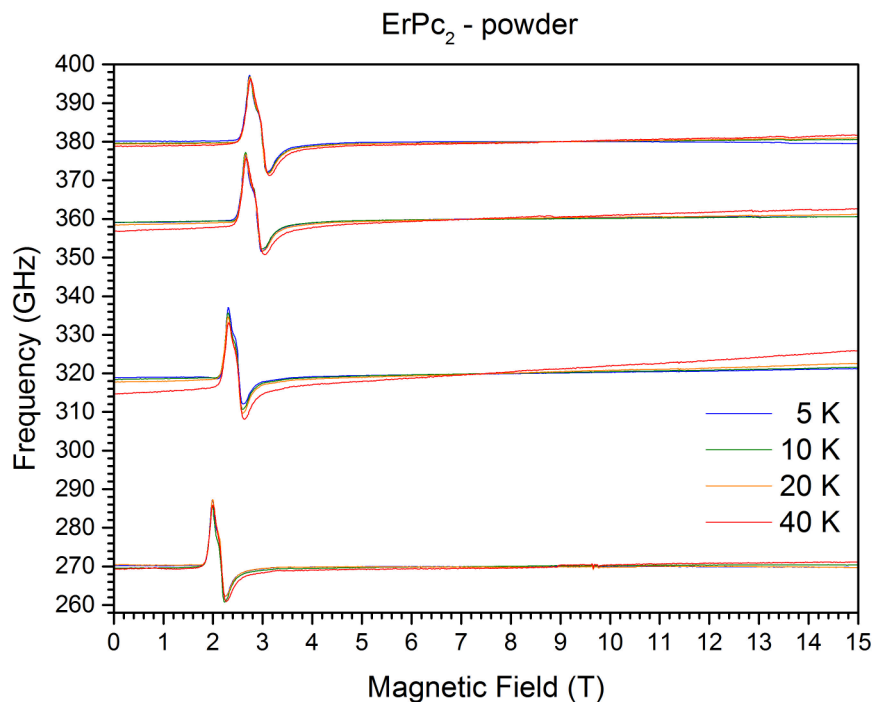


Figure 3.59: Temperature dependence of ErPc₂ measured by HFEPR spectroscopy.

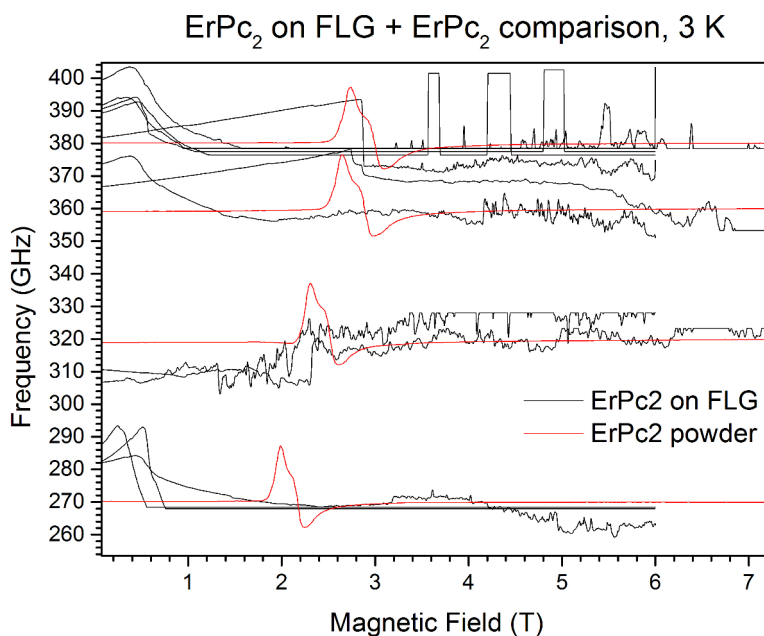


Figure 3.60: HFEPR spectrum of ErPc₂ compound on graphene-covered substrate for four frequencies at $T = 3$ K. Black lines represent measurement and red lines represent fit.

3. EXPERIMENT

3.9.5. Scanning Electron Microscopy

Figure (3.61) shows SEM image of deposited ErPc_2 on the graphene-covered substrate. This compound is highly soluble in dimethylformamide. Molar concentration of solution was $c = 1 \text{ mM}$. Approximate size of crystals formed was 20 - 200 nm. It showed fair homogeneity at the nano-scale.

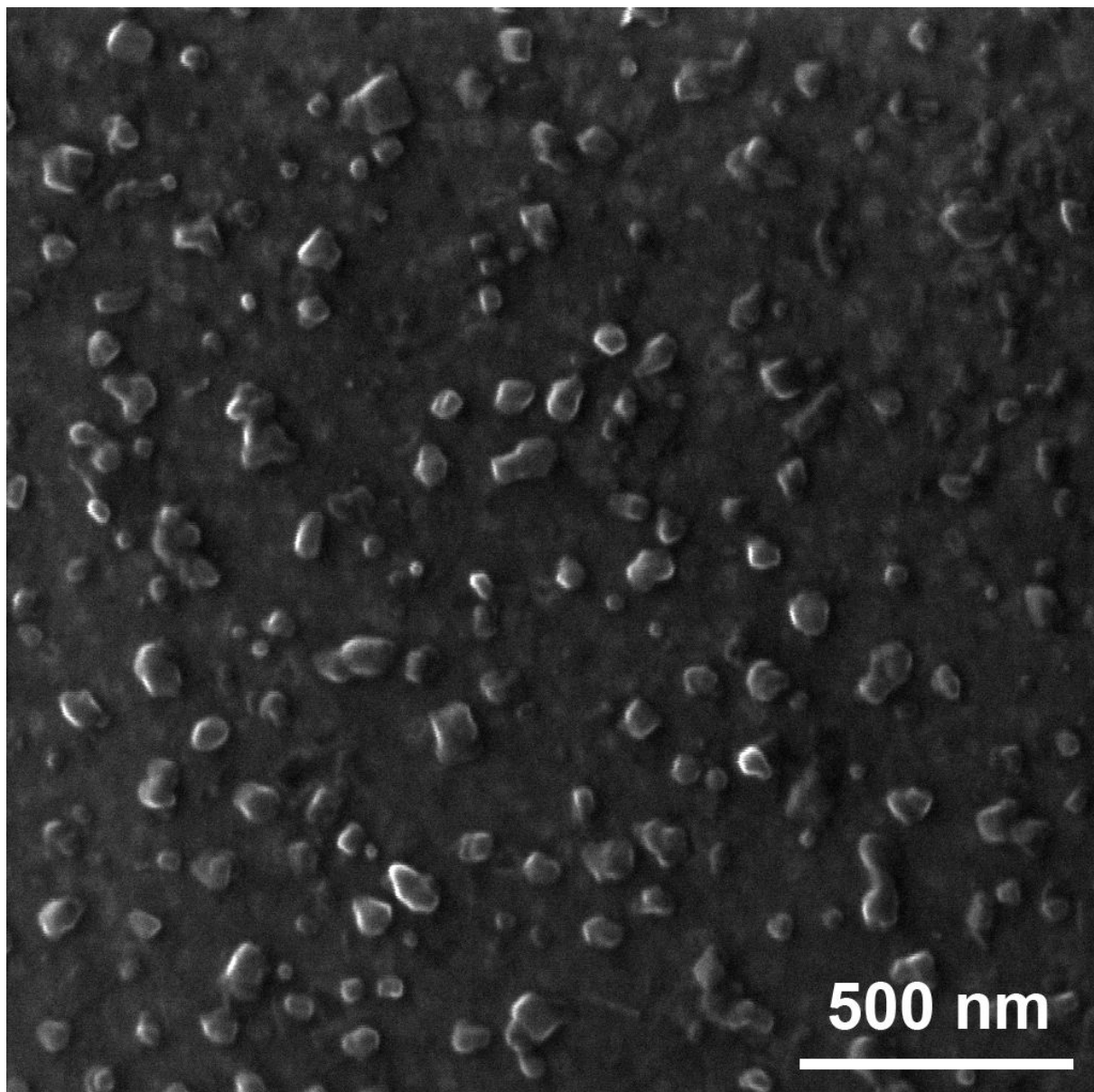


Figure 3.61: SEM image of ErPc_2 on the graphene-covered substrate. Voltage used: 10 kV. Detector: secondary electrons. Image was acquired at CEITEC - BUT, Czech Republic.

Figures (3.62) and (3.63) illustrate homogeneity of surface coverage and dendrite-like structure at larger scale for ErPC₂ compound, respectively. However, this pattern has to be interpreted critically. There is also a counter ion–tetrabutylammonium (TBA) present, and thus also contributes to the final image.

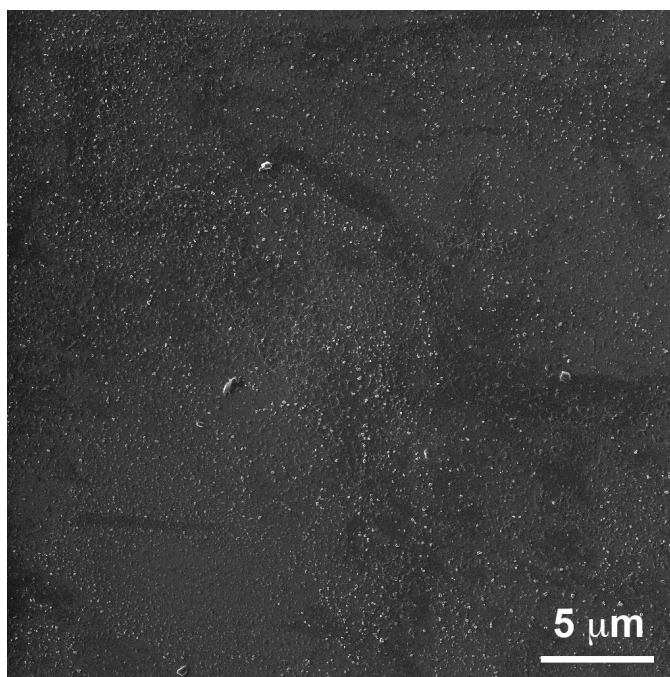


Figure 3.62: SEM image revealing distribution and homogeneity of deposited ErPC₂ compound. Image was acquired at CEITEC BUT, Brno, Czech Republic. Voltage used: 10 kV. Detector: secondary electrons.

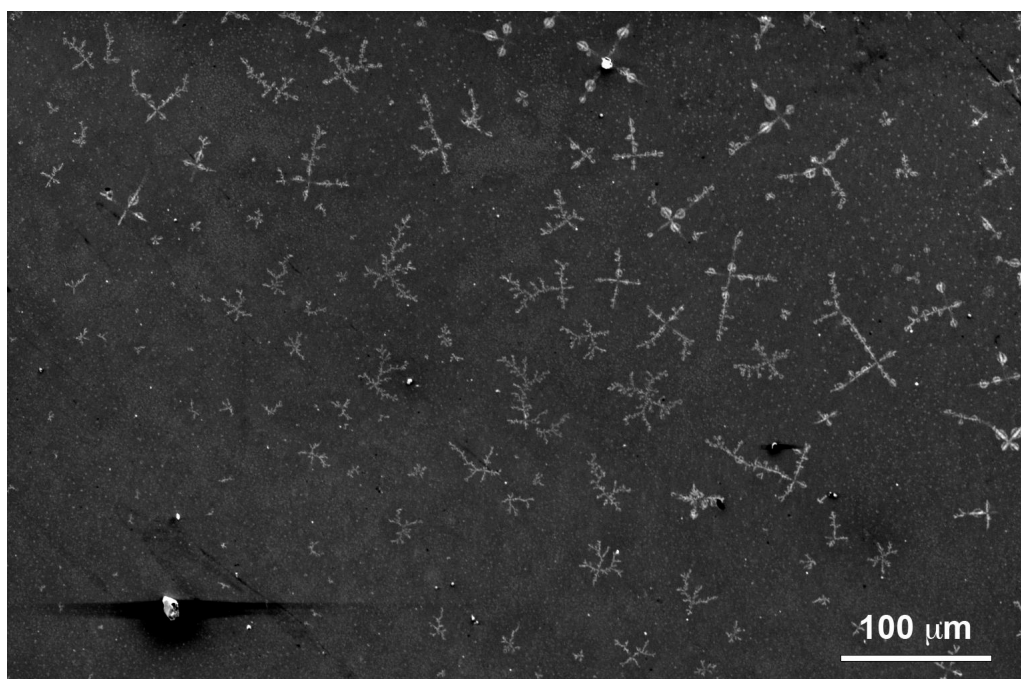


Figure 3.63: SEM image of dendrite-like structure of ErPC₂ compound on graphene-covered substrate. Image was acquired at Max Planck Institute in Stuttgart, Germany. Voltage used: 5 kV. Detector: secondary electrons.

3. EXPERIMENT

4. Conclusions

In conclusion, graphene-based hybrid materials were prepared by multiple modified Langmuir–Schaefer deposition method and characterised by spectroscopic means, namely high frequency electron paramagnetic resonance (HFEPN) and Raman spectroscopy. Moreover, morphology of prepared samples was revealed by scanning electron microscopy. Electronic properties were approximatively estimated by four-point probe resistance measurements (3.3).

First and foremost, I would like to discuss results obtained during preparative and characterisation steps. When it comes to the preparative steps, isotherms played crucial role in final homogeneity and size of deposited compounds. For the characterisation, Raman spectroscopy and scanning electron microscopy (SEM) confirmed structure of compounds. During this work, superconducting quantum interference device (SQUID) was also used to measure magnetic properties of DM18N on graphene-covered substrate and reference graphene-covered substrate. There was, however, no reproducible magnetic difference observed. This was ascribed to huge diamagnetic contribution from substrate. Diamagnetic corrections were treated by Pascal’s constants [53].

Isotherms represent the very first step in deposition by Langmuir–Schaefer method. They are different for every compound and represent a curve in pV diagram obtained during the molecular deposition at constant temperature. In this case, $V_{\text{THROUGH}} = A$ and actual ‘through’ area A was expressed in area per molecule a . This parameter denoted how much space was left at the air/water interface for a compound to spread. When the a is left too small, compounds tend to shrink and form aggregates. On the contrary, for a too larger, compounds are not homogeneously distributed on the substrate. This parameter is closely connected to used molar concentration c and volume V . By lowering or increasing c it is possible to tune molecular formation on the substrate. The best homogeneity with smallest particle size was for observed for ErPc₂ with the lowest molar concentration c .

Table 4.1: Calculated area per molecule a left, molar concentration c used, and volume V used.

Compound	Cu(dbm) ₂	Ni(salen)	DM15N	DM18N	ErPc ₂
c [mM]	5	5	5	5	1
V [μL]	1400	250	200	300	150
a [Å ² /molecule]	0.9	5.8	3	2	42

The suggested improvement was done by simply measuring distance d of two furthest lying carbon atoms in every compound, making a square value, and suggesting this to be estimation for how large area per molecule a should be left. The measurement of dimension was done in Mercury using the Cambridge Crystallographic Data Centre (CCDC) for

4. CONCLUSIONS

particular compound structure. This was, however, a mere estimate. For detailed analysis, it would be necessary to investigate deeper into compound formation at the air/water interface and calculate energetic and geometric size of compounds. Nevertheless, estimation made by simply measuring the actual molecular dimension was the very first step. Moreover, every substrate provides different adhesion potential for various compounds, and thus investigation into these influences belongs to next actions regarding this topic.

Table (4.2) proposes further improvement of deposition concentration for investigated compounds, considering the same volume V as mentioned in Table (4.1) and same deposition set-up, the molar concentration c according to calculated compounds' dimensions should have been generally lower in order to prepare monolayer-thin film.

Table 4.2: Suggestion for further improvement of deposition.

Compound	Cu(dbm) ₂	Ni(salen)	DM15N	DM18N	ErPc ₂
Distance d [Å]	13.6	10.8	11.5	11.5	13.0
Compound area [Å ²]	185	117	132	132	169
Molar concentration [μ M]	24	248	114	76	249

The Raman spectra were acquired in order to confirm that dissolved compounds used during multiple modified Langmuir–Schaefer deposition were not impaired by this approach and can be unambiguously observed on the graphene-covered substrate. The graphene in the form on few-layer graphene (FLG) was observed for every spectrum, Figure (3.11). Therefore, multiple deposition is possible and water sub-phase does not damage graphene-covered substrate. In the case of Cu(dbm)₂, which formed a bigger aggregates, peaks with lower intensity than for the powder spectra contributing to the overall spectrum were observed, Figure (3.20). These peaks were in agreement with reference spectrum and literature. Ni(salen) compound, however, was not observed by Raman spectroscopy, this can be ascribed to the fact, that this compound exhibited very low coverage and poor homogeneity, Figure (3.29). On the contrary, cobalt ferrocenes represented by DM15N and DM18N had fair coverage and homogeneity and one specific peak was observed for compounds on graphene-covered substrate, Figure (3.37) and Figure (3.48), respectively. Lastly, specific peaks for ErPc₂ compound deposited on graphene-covered substrate were also observed, Figure (3.57).

Figure (4.1) illustrates images from optical microscope for compounds deposited on graphene-covered substrate obtained during acquisition of Raman spectra. (a) Cu(dbm)₂ on FLG formed bigger aggregates, Ni(salen) is not depicted as it had poor homogeneity and is evaluated as least suitable for deposition and characterisation by methods described in this thesis, (b) ErPc₂ on FLG formed particles with size 20 – 200 nm that were resolved better by SEM, Figure (3.9.5). In this image, pink background represents substrate, purple is FLG and small particulates represent deposited compound. The homogeneity is apparently lower compared to DM15N or DM18N. For this compound rather region-dependent homogeneity was observed. Moreover, it is necessary to realise, that samples underwent several rapid thermal changes during multiple HFEPR measurements resulting in certain degradation of samples. The best coverage was observed for cobalt ferrocenes (c)–(d) DM15N and (e)–(f) DM18N.

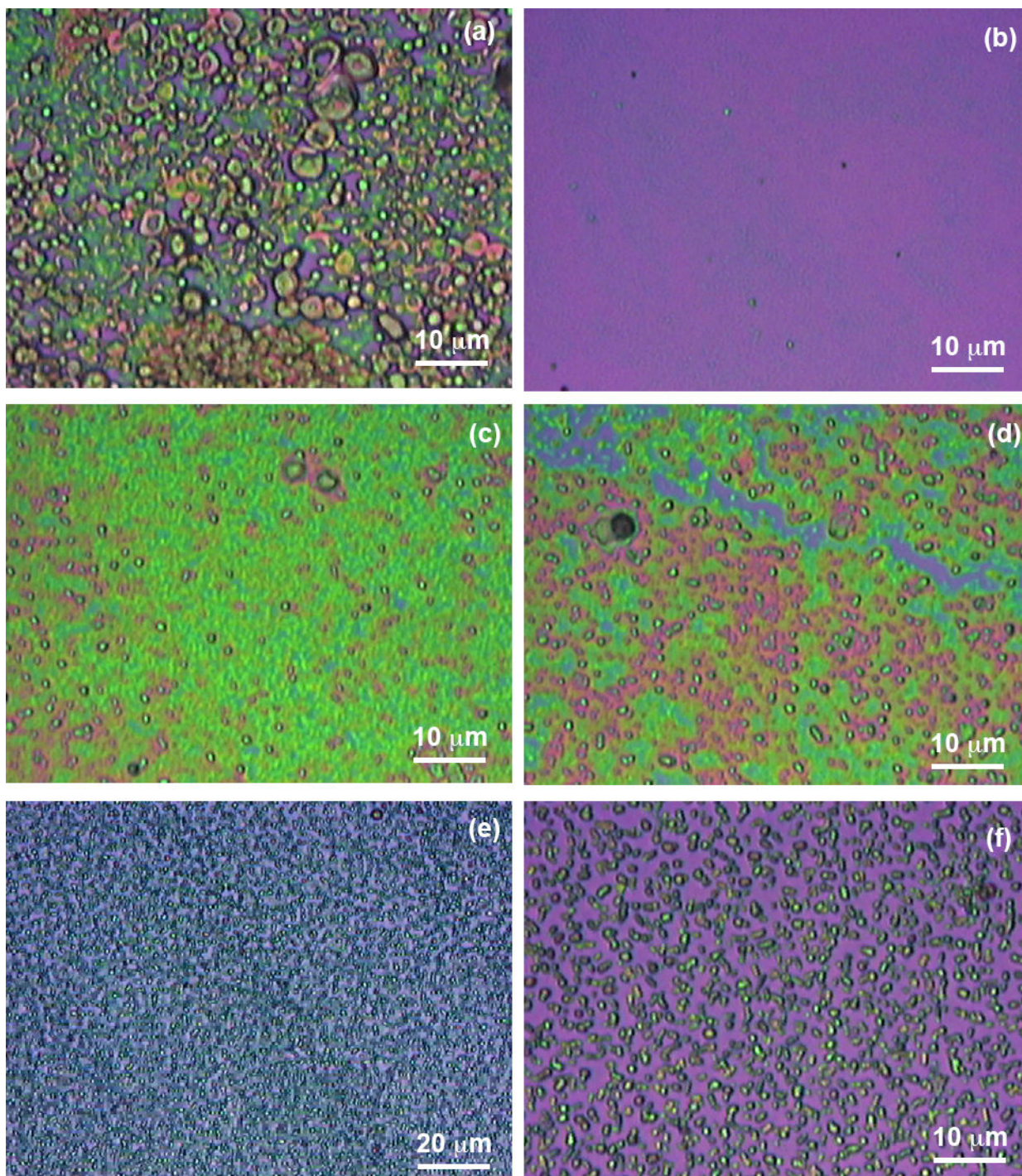


Figure 4.1: Optical images acquired during Raman spectroscopy. (a) $\text{Cu}(\text{dbm})_2$ on FLG, (b) ErPc_2 on FLG, (c)–(d) DM15N on FLG, and (e)–(f) DM18N on FLG.

4. CONCLUSIONS

The main characterisation method was high frequency electron paramagnetic resonance (HF-EPR), which observes interaction of microwave radiation with a sample. By this approach, it was possible to precisely measure magnetic properties of reference bulk compounds, where all orientations of magnetic moments are present. By these measurements, zero-field splitting parameters D and E , as well as g-value components were obtained and compared to *ab initio* simulations. These parameters are essential for further development of single-molecule magnets. At this stage, it is important to give feedback to synthetic and theoretical chemists in order to fine-tune properties of prepared compounds, as well as to close gap between simulations based on theory and experiments.

The next step was to measure interaction and change of spectra on graphene-covered substrate. At this point, it is necessary to emphasise, that thin films contain a minute amount of paramagnetic compounds confined on surface. The biggest advantage of this technique is that electrons are being investigated. Therefore, allowing for investigation of magnetic and electric properties at the same time.

Figure (3.23) shows the first compound $\text{Cu}(\text{dbm})_2$ on graphene-covered substrate. The characteristic hyperfine structure for this compound was observed for bulk material as well as on the graphene-covered substrate. Therefore, in comparison with powder spectra measured by high frequency EPR, the magnetic properties seem to be preserved after deposition. Intactness of compounds on the substrate represents another requirement for viable deposition route. The $\text{Ni}(\text{salen})$ on graphene-covered substrate did not confirm our presumption of changing from diamagnetic to paramagnetic in the presence of graphene, and is subjected for further analysis in this direction. The spectra for DM18N and ErPc_2 also did not reveal any unique behaviour on the graphene-covered substrate by these measurements and are also subjected for further analyses. Lastly, Figure (3.40) of DM15N on graphene-covered substrate revealed a direct observation of magnetic characteristic compared to powder spectra. Figure (3.42) demonstrated possibility to treat spectra from the direction of electronic transport properties and conductivity. There are recently published articles that deal with magnetoresistance, conductivities, and influence of magnetic field on conductivity of graphene and graphene-based materials [54], [51], [55].

To sum up, there are several terms that are crucial regarding graphene-based hybrid materials. Concentration of compounds, influence of substrate, intactness after deposition, and sensitivity of characterisation techniques to prepared thin films.

References

- [1] GEIM, A.K. and NOVOSELOV K.S. The rise of graphene. *Nature Materials* [online]. 2007, vol. 6, pp. 183–191. Available from: doi:[10.1038/nmat1849](https://doi.org/10.1038/nmat1849). Available from: www.nature.com/doifinder/10.1038/nmat1849.
- [2] DU, X. et al. Approaching ballistic transport in suspended graphene. *Nature Nanotechnology* [online]. 2008, vol. 3, pp. 491–495. Available from: doi:[10.1038/nnano.2008.199](https://doi.org/10.1038/nnano.2008.199). Available from: <https://www.nature.com/nnano/journal/v3/n8/full/nnano.2008.199.html>.
- [3] LEE, CH. et al. Measurement of the Elastic Properties and Intrinsic Strength of Monolayer Graphene. *Science* [online]. 2008, vol. 321, no. 5887, pp. 385–388. Available from: doi:[10.1126/science.1157996](https://doi.org/10.1126/science.1157996). Available from: <http://science.sciencemag.org/content/321/5887/385>.
- [4] SEOL, J.H. et al. Two-Dimensional Phonon Transport in Supported Graphene. *Science* [online]. 2010, vol. 328, no. 5975, pp. 213–216. Available from: doi:[10.1126/science.1184014](https://doi.org/10.1126/science.1184014). Available from: <http://www.sciencemag.org/cgi/doi/10.1126/science.1184014>.
- [5] NOVOSELOV, K.S. et al. Electric Field Effect in Atomically Thin Carbon Films. *Science* [online]. 2004, vol. 306, no. 5696, pp. 666–669. Available from: doi:[10.1126/science.1102896](https://doi.org/10.1126/science.1102896). Available from: <http://www.sciencemag.org/cgi/doi/10.1126/science.1102896>.
- [6] WAJID, A.S. et al. Polymer-stabilized graphene dispersions at high concentrations in organic solvents for composite production. *Carbon* [online]. 2012, vol. 50, no. 2, pp. 526–534. Available from: doi:[10.1016/j.carbon.2011.09.008](https://doi.org/10.1016/j.carbon.2011.09.008). Available from: <http://linkinghub.elsevier.com/retrieve/pii/S0008622311007421>.
- [7] PATON, K.R. et al. Scalable production of large quantities of defect-free few-layer graphene by shear exfoliation in liquids. *Nature Materials* [online]. 2014, vol. 13, pp. 624–630. Available from: doi:[10.1038/nmat3944](https://doi.org/10.1038/nmat3944). Available from: <http://www.nature.com/doifinder/10.1038/nmat3944>.
- [8] BOLAND, C.S. et al. Sensitive, High-Strain, High-Rate Bodily Motion Sensors Based on Graphene–Rubber Composites. *ACS Nano* [online]. 2014, vol. 8, no. 9, pp. 8819–8830. Available from: doi:[10.1021/nn503454h](https://doi.org/10.1021/nn503454h). Available from: <http://pubs.acs.org/doi/abs/10.1021/nn503454h>.
- [9] RAVULA, S. et al. Ionic liquid-assisted exfoliation and dispersion. *Nanoscale* [online]. 2015, vol. 7, pp. 4338–4353. Available from: doi:[10.1039/C4NR01524J](https://doi.org/10.1039/C4NR01524J). Available from: <http://xlink.rsc.org/?DOI=C4NR01524J>.

REFERENCES

- [10] RAO, C.N.R., MAITRA U. and MATTE H.S.S.R. Synthesis, Characterization, and Selected Properties of Graphene. In: *Graphene synthesis, properties, and phenomena*. Weinheim: Wiley-VCH, 2012, pp. 1–47. ISBN 9783527651122.
- [11] GEIM, A.K. Graphene. *Graphene: Status and Prospects* [online]. 2009, vol. 324, no. 5934, pp. 1530–1534. Available from: doi:10.1126/science.1158877. Available from: <http://www.sciencemag.org/cgi/doi/10.1126/science.1158877>.
- [12] VADUKUMPULLY, S., PAUL J. and VALIYAVEETIL S. Cationic surfactant mediated exfoliation of graphite into graphene flakes. *Carbon* [online]. 2009, vol. 47, no. 14, pp. 3288–3294. Available from: doi:10.1016/j.carbon.2009.07.049. Available from: <http://linkinghub.elsevier.com/retrieve/pii/S0008622309004849>.
- [13] LEUENBERGER, M.N. and LOSS D. Quantum computing in molecular magnets. *Nature* [online]. 2001, vol. 410, pp. 789–793. Available from: doi:10.1038/35071024. Available from: <http://www.nature.com/doifinder/10.1038/35071024>.
- [14] BADER, K. et al. Room temperature quantum coherence in a potential molecular qubit. *Nature Communications* [online]. 2014, vol. 5, no. 5304. Available from: doi:10.1038/ncomms6304. Available from: <http://www.nature.com/doifinder/10.1038/ncomms6304>.
- [15] QIU, D. et al. Spin crossover-graphene nanocomposites. *RSC Advances* [online]. 2014, vol. 4, no. 59, pp. 31323–31327. Available from: doi:10.1039/C4RA04257C. Available from: <http://xlink.rsc.org/?DOI=C4RA04257C>.
- [16] NEMEC, I. et al. Tuning of spin crossover behaviour in iron(iii) complexes involving pentadentate Schiff bases and pseudohalides. *Dalton Transactions* [online]. 2011, vol. 40, no. 39, pp. 10090–10099. Available from: doi:10.1039/c1dt10696a. Available from: <http://xlink.rsc.org/?DOI=c1dt10696a>.
- [17] EL FATIMY, A. et al. Epitaxial graphene quantum dots for high-performance terahertz bolometers. *Nature Nanotechnology* [online]. 2016, vol. 11, pp. 335–338. Available from: doi:10.1038/nnano.2015.303. Available from: <http://www.nature.com/doifinder/10.1038/nnano.2015.303>.
- [18] HONG, J. et al. Chemically Engineered Graphene-Based 2D Organic Molecular Magnet. *ACS Nano* [online]. 2013, vol. 7, no. 11, pp. 10011–10022. Available from: doi:10.1021/nn403939r. Available from: <http://pubs.acs.org/doi/abs/10.1021/nn403939r>.
- [19] LE FERRAND, H. et al. Magnetic assembly of transparent and conducting graphene-based functional composites. *Nature Communications* [online]. 2016, vol. 7, no. 12078. Available from: doi:10.1038/ncomms12078. Available from: <http://www.nature.com/doifinder/10.1038/ncomms12078>.
- [20] CIESIELSKI, A. and SAMORI P. Supramolecular Approaches to Graphene. *Advanced Materials* [online]. 2016, vol. 28, no. 29, pp. 6030–6051. Available from: doi:10.1002/adma.201505371. Available from: <http://doi.wiley.com/10.1002/adma.201505371>.
- [21] WARNER, J. et al. *Graphene* [online]. 1st ed. Oxford: Elsevier, 2012. 470 pp. ISBN 9780123948274. Available from: <https://www.elsevier.com/books/graphene/warner/978-0-12-394593-8>.
- [22] *Hybridization of Atomic Orbitals*. [online]. USA: National Science Foundation, 2016. Available from: <https://chem.libretexts.org/>.

- [23] WALLACE, P.R. The Band Theory of Graphite. *Physical Review* [online]. 1947, vol. 71, no. 9, pp. 622–634. Available from: doi:[10.1103/PhysRev.71.622](https://doi.org/10.1103/PhysRev.71.622). Available from: <https://link.aps.org/doi/10.1103/PhysRev.71.622>.
- [24] DRUDE, P. Zur Elektronentheorie der Metalle. *Annalen der Physik* [online]. 1900, vol. 306, no. 3, pp. 566–613. Available from: doi:[10.1002/andp.19003060312](https://doi.org/10.1002/andp.19003060312). Available from: <http://doi.wiley.com/10.1002/andp.19003060312>.
- [25] KITTEL, CH. *Introduction to Solid State Physics*. 8th ed. New Jersey: John Wiley & Sons, 2005. 704 pp. ISBN 978-0471415268.
- [26] GATTESCHI, D., SESSOLI R. and VILLAIN J. *Molecular Nanomagnets*. 1st ed. New York: Oxford University Press, 2006. 408 pp. ISBN 9780198567530.
- [27] VAN SLAGEREN, J. *Introduction to Molecular Magnetism*. 1. Physics Institute: University of Stuttgart, 2004. 44 pp.
- [28] NEMEC, I. et al. Magnetic Anisotropy and Field-induced Slow Relaxation of Magnetization in Tetracoordinate Co(II) Compound [Co(CH₃-im)₂Cl₂]. *Materials* [online]. 2017, vol. 10, no. 3. Available from: doi:[10.3390/ma10030249](https://doi.org/10.3390/ma10030249). Available from: <http://www.mdpi.com/1996-1944/10/3/249>.
- [29] NEESE, F. and PANTAZIS D.A. What is not required to make a single molecule magnet. *Faraday Discussions* [online]. 2011, vol. 148, pp. 229–238. Available from: doi:[10.1039/C005256F](https://doi.org/10.1039/C005256F). Available from: <http://xlink.rsc.org/?DOI=C005256F>.
- [30] PETTY, M.C. *Langmuir-Blodgett Films: An Introduction*. 1st ed. Cambridge: Cambridge University Press, 1996. 256 pp. ISBN 978-0521424509.
- [31] GENGLER, R. *A modified Langmuir Schaefer method for the creation of functional thin films* [online]. Groningen: University of Groningen, 2010. Available from: [http://www.rug.nl/research/portal/publications/pub\(8d102806-1950-4ee8-a84a-79b7f29312f2\).html](http://www.rug.nl/research/portal/publications/pub(8d102806-1950-4ee8-a84a-79b7f29312f2).html).
- [32] WEIL, J.A. and BOLTON J.R. *Electron Paramagnetic Resonance*. 2nd ed. New Jersey: John Wiley & Sons, 2006. 664 pp. ISBN 9780471754961.
- [33] RIEGER, P. *Electron Spin Resonance*. 1st ed. Cambridge: The Royal Society of Chemistry, 2007. 186 pp. ISBN 978-0-85404-355-2.
- [34] DUB, P., SPOUSTA J. and ZLÁMAL J. *Kvantová mechanika*. Institute of Physical Engineering: Brno University of Technology, 2005. 180 pp.
- [35] *Fundamental Physical Constants*. [online]. USA: National Institute of Standards and Technology, 2017. Available from: <http://physics.nist.gov/cgi-bin/cuu/Value?gem>.
- [36] UMBACH, CH. *Raman: Theory and Instrumentation*. Department of Materials Science and Engineering: Cornell University, New York, 2009.
- [37] ATKINS, P., DE PAULA J. and FRIEDMAN R. *Quanta, Matter and Change*. 1st ed. New York: W. H. Freeman, 2009. 782 pp. ISBN 0-7167-6117-3.
- [38] SPIZZIRRI, P.G. et al. *Nano-Raman spectroscopy of silicon surfaces*. Materials Forum: 2008.
- [39] KOLÍBALOVÁ, E. *Introduction to Scanning Electron Microscopy*. Brno: CEITEC BUT, 2012.

REFERENCES

- [40] HRUBÝ, J. *Preparation and application of metal and semiconductor nanostructures* [online]. Brno: Brno University of Technology, 2015. 44 pp. Available from: https://www.vutbr.cz/www_base/zav_prace_soubor_verejne.php?file_id=103652.
- [41] REIMER, L. *Scanning Electron Microscopy*. 2nd ed. Berlin: Springer, 1998. 529 pp. ISBN 978-3-642-08372-3.
- [42] LENG, X., XIONG X. and ZOU J. Rapid microwave irradiation fast preparation and characterization of few-layer graphenes. *Transactions of Nonferrous Metals Society of China* [online]. 2014, vol. 24, no. 1, pp. 177–183. Available from: doi:10.1016/S1003-6326(14)63045-4. Available from: <http://linkinghub.elsevier.com/retrieve/pii/S1003632614630454>.
- [43] KIM, J. et al. *Expanding characteristics of graphite in microwave-assisted exfoliation*. Istanbul: Scientific Cooperations International Workshops on Engineering Branches, 2014.
- [44] MALARD, L.M. et al. Raman spectroscopy in graphene. *Physics Reports* [online]. 2009, vol. 473, no. 5-6, pp. 51–87. Available from: doi:10.1016/j.physrep.2009.02.003. Available from: <http://linkinghub.elsevier.com/retrieve/pii/S0370157309000520>.
- [45] MA, B.-G. et al. Synthesis and structure of bis (dibenzoylmethane). *Journal of Chemical Crystallography*. 1999, vol. 29, no. 7, pp. 793–796.
- [46] LENZ, S. *Influences on Electron Spin Relaxation in Mononuclear Transition Metal Beta -Diketonate Complexes*. Stuttgart: University of Stuttgart, 2015. 75 pp.
- [47] NEKOEI, A.-R. et al. Theoretical study, and infrared and Raman spectra of copper(II) chelated complex with dibenzoylmethane. *Spectrochimica Acta Part A: Molecular and Biomolecular Spectroscopy* [online]. 2014, vol. 128, pp. 272–279. Available from: doi:10.1016/j.saa.2014.02.097. Available from: <http://linkinghub.elsevier.com/retrieve/pii/S1386142514002844>.
- [48] TANG, CH. 2,2 -[Cyclohexane-1,2-diylbis(nitrilomethylidyne)]diphenolatonickel(II). *Acta Crystallographica Section E* [online]. 2009, vol. 65, no. 317. Available from: doi:10.1107/S1600536809006084. Available from: <http://scripts.iucr.org/cgi-bin/paper?S1600536809006084>.
- [49] DOCHERTY, J. et al. Detection of potentially toxic metals by SERS using salen complexes. *The Analyst* [online]. 2016, vol. 141, no. 20, pp. 5857–5863. Available from: doi:10.1039/C6AN01584K. Available from: <http://xlink.rsc.org/?DOI=C6AN01584K>.
- [50] LI, J.-S. et al. Polyoxometalate-based metal–organic framework-derived hybrid electrocatalysts for highly efficient hydrogen evolution reaction. *Journal of Materials Chemistry A* [online]. 2016, vol. 4, no. 4, pp. 1202–1207. Available from: doi:10.1039/C5TA09743F. Available from: <http://xlink.rsc.org/?DOI=C5TA09743F>.
- [51] GOPINADHAN, K. et al. Extremely large magnetoresistance in few-layer graphene/boron–nitride heterostructures. *Nature Communications* [online]. 2015, no. 8337. Available from: doi:10.1038/ncomms9337. Available from: <http://www.nature.com/doifinder/10.1038/ncomms9337>.
- [52] DÖRFEL, M. *Single Crystal Studies of the Magnetic Anisotropy of Molecular Nanomagnets*. Stuttgart: University of Stuttgart, 2015. 197 pp.

- [53] BAIN, G.A. and BERRY J.F. Diamagnetic Corrections and Pascal's Constants. *Journal of Chemical Education* [online]. 2008, vol. 85, no. 4, pp. 532. Available from: doi:10.1021/ed085p532. Available from: <http://pubs.acs.org/doi/abs/10.1021/ed085p532>.
- [54] KISSLINGER, F. et al. Linear magnetoresistance in mosaic-like bilayer graphene. *Nature Physics* [online]. 2015, vol. 11, pp. 650–653. Available from: doi:10.1038/nphys3368. Available from: <http://www.nature.com/doi/10.1038/nphys3368>.
- [55] KRYUCHKOV, S.V. and KUKHAR E.I. Influence of the Magnetic Field on the Graphene Conductivity. *Journal of Modern Physics* [online]. 2012, vol. 3, no. 9, pp. 994–1001. Available from: doi:10.4236/jmp.2012.39129. Available from: <http://www.scirp.org/journal/PaperDownload.aspx?DOI=10.4236/jmp.2012.39129>.

REFERENCES

List of Abbreviations

Abbreviation	Meaning
EPR	Electron Paramagnetic Resonance
ESR	Electron Spin Resonance
HFEPR	High Frequency Electron Paramagnetic Resonance
NMR	Nuclear Magnetic Resonance
SMM	Single-Molecule Magnet
SEM	Scanning Electron Microscopy
SLG	Single-Layer Graphene
BLG	Bi-Layer Graphene
FLG	Few-Layer Graphene
DOS	Density of States
LB	Langmuir–Blodgett
LS	Langmuir–Schaefer
SH	Spin Hamiltonian
TA	Transversal Acoustic
TO	Transversal Optical
LO	Longitudinal Optical
SE	Secondary Electrons
BSE	Back-Scattered Electrons
AE	Auger Electrons
PET	Positron Emission Tomography
NMP	<i>N</i> -Methyl-2-pyrrolidone
CL	Chloroform
DCM	Dichloromethane
DMF	Dimethylformamide
VTI	Variable Temperature Insert
CCD	Charge-Coupled Device
CEITEC	Central European Institute of Technology
BUT	Brno University of Technology
SAS	Slovak Academy of Sciences
MUNI	Masaryk University
CASSCF	Complete active space self-consistent field
NEVPT2	N-Electron Valence State Perturbation Theory
SQUID	Superconducting Quantum Interference Device
CCDC	Cambridge Crystallographic Data Centre
AG	Arbeitsgruppe (Working Group)
AC	Alternating Current